DESIGN AND OPTICAL CHARACTERIZATION OF GALLIUM ARSENIDE ALUMINUM ARSENIDE MATERIAL SYSTEM REFLECTIVE MODULATORS FOR MID-INFRARED FREE SPACE OPTICAL APPLICATIONS USING SOLID-SOURCE MOLECULAR BEAM EPITAXY

A Dissertation

presented to

the Faculty of the Graduate School

at the University of Missouri-Columbia

In Partial Fulfillment

of the Requirements for the Degree

Doctor of Philosophy

---

by

STANLEY IKPE

Dr. Gregory Triplett, Dissertation Supervisor

MAY 2013

The undersigned, appointed by the dean of the Graduate School, have examined the dissertation entitled

DESIGN AND OPTICAL CHARACTERIZATION OF GALLIUM ARSENIDE ALUMINUM ARSENIDE MATERIAL SYSTEM REFLECTIVE MODULATORS FOR MID-INFRARED FREE SPACE OPTICAL APPLICATIONS USING SOLID-SOURCE MOLECULAR BEAM EPITAXY

presented by Stanley Ikpe,

a candidate for the degree of doctor of philosophy, and hereby certify that, in their opinion, it is worthy of acceptance.

Professor Gregory Triplett

Professor Robert O'Connell

Professor Carmen Chicone

Professor Jae Wan Kwon

Professor Naz Islam

DEDICATION

To my loving family for always inspiring me to achieve my greatest aspirations and to my dearest friends for encouraging me to persevere…

ACKNOWLEDGEMENTS

First and foremost, I would like to thank my creator and savior through whom all is possible. To my advisor, Dr. Gregory Triplett for allowing me to pursue my ambitions and navigating me through tough and sometimes circuitous terrain. Your persistence and encouragement has helped me throughout my graduate career. Also, to Dr. Carmen Chicone, Dr. Robert Oconnell, Dr. Jae Won Kwon, and Dr. Naz Islam for your patience, advisement, and support. It is greatly appreciated.

I would also like to thank my fellow graduate students and research companions Denzil Roberts, Hisham Abbas, Hayder Mahdi, Nicholas Rada, and Mehjabeen Khan. Your confidence in my ability, readiness to learn with me, eagerness to listen as I voice my concerns and uncertainties, and willingness to laugh at an occasional bad joke has not only helped me complete this work but has made me a confident research scientist.

Lastly, but surely not least, I thank my great family and my close friends. You all have always helped me get through all my difficulties and provided me with the love and emotional support necessary to make it through such a demanding and grueling process. You all have motivated, encouraged, and inspired me throughout my graduate career and I sincerely love and appreciate you all.

TABLE OF CONTENTS

LIST OF ILLUSTRATIONS

Figure Page

LIST OF TABLES

Figure Page

LIST OF ABBREVIATIONS

(AFM)	Atomic Force Microscopy
(APD)	Antiphase Domains
(BEP)	Beam equivalent Pressure
(CCR)	Corner-Cube Retroreflector
(DBQW)	Double Barrier Quantum Well
(DBR)	Distributed Bragg Reflector
(FSO)	Free Space Optics/Optical
(FWHM)	Full Width at Half Maximum
(LoS)	Line of Sight
(MEMS)	Micro Electromechanical System
(MIR)	Mid-infrared
(MQW)	Multiple Quantum Well
(MRR)	Modulating Retroreflector
(NIR)	Near-infrared
(NRL)	Naval Research Lab
(QWM)	Quantum Well Modulator
(RHEED)	Reflection High Energy Electron Diffraction
(RM)	Reflective Modulator
(TMM)	Transfer Matrix Method
(SAC)	Self-Activated Centers
(SEM)	Scanning Electron Microscopy
(SI)	Semi-Insulative

(UAV) Unmanned Aerial Vehicle

(UHV) Ultra-high Vacuum

ABSTRACT

With the ever-growing usage of free space optical communication implementations, new innovations are currently being made to help improve the quality of transmission of these systems. One particular method employed to help improve transmission efficiency of optical links is shifting the transmission wavelength into the mid-infrared spectrum. Studies have shown sufficient increase in atmospheric transmission at and around mid-infrared wavelengths (near 3-5 μm). In order to successfully implement such systems at these wavelengths, devices must first be designed that are capable of optical communication operation at such wavelengths. One such device common in modern free space optical systems is the reflective modulator. This device minimizes the pointing and tracking associated with establishing free space optical connections. In this dissertation, a free space optical reflective modulator is designed using Gallium Arsenide and Aluminum Arsenide (GaAs/AlAs) to operate at mid-infrared transmission wavelengths. The reflective modulator consists of multiple quantum well modulator (QWM) atop of a distributed Bragg reflector (DBR). The physical device characteristics are analyzed and the device functionality evaluated using optical characterization techniques.

CHAPTER 1

INTRODUCTION

With recent growths in mid-infrared technology, the span of its possible application is far-reaching. Particularly in the realm of optical communication, where much work is being done to improve efficiency and performance of communication links. The demand for large bandwidth, high speed data transmission is everpresent in our modern society. Therefore the implementations of optical communication systems is more widely employed now more than ever before. Due largely, in part, to their inherent light-speed transmission and large data bandwidth capabilities [1-3]. Though major milestones in optical communications have been achieved in recent years, the use of lightwaves to transfer information is by no means a new idea. Smoke signaling systems, dating back to the biblical era, helped lay some of fundamental principles for modern day optical communication. Millennia later, the development and patent of Alexander Graham Bell's photophone, in the 1880s, became the cornerstone for the modern optical communication scheme. Using a system of mirrors, Bell was able to achieve point to point vocal transmission using sunlight. Though the photophone was never widely employed, it is the progenitor to modern lightwave communication implementations. Recent technological advancements in semiconductor optoelectronics and fiber optics, has helped to further the progression of optical communication implementations.

1.1 Optical Communication

The development of the first semiconductor laser in the 1950s, inexplicitly marked the birth of the modern optical communication systems. The semiconductor laser's compact size, spectral confined radiation profile, and high-powered modulation capabilities made it the ideal device for optical communication applications. Various techniques and device implementations in the years to follow helped improve the efficiency of laser devices, thus making them even more effective for such applications. Continued optoelectronic breakthroughs including the development of the photodetector (1960s) and the development of low loss optical fibers (1970s) for effective optical transmission, eventually led to the emergence of fiber optic systems in the late 1980s.

Traditional optical communication systems consist of three major components: the optical transmitter, the optical receiver, and the associated transmission media; with each component playing a specific role in the data transmission process. The optical transmitter is responsible for converting an input electrical signal into a modulated optical signal for transmission. The transmitter contains an optical source, typically a laser or high power light emitting diode (LED). The wavelength essentially determines the efficacy of transmission through the medium of the system (dependent upon the material composition of the primary medium). Conversely, the optical receiver converts the transmitted optical signal back into an electrical signal to be interpreted by drive circuitry. The receiver is typically the limiting factor of such optical systems

because of their inability to track high frequency modulation at lower optical power densities. The final component in traditional optical systems is the medium in which the optical signal is transmitted or simply the transmission medium. It is in the transmission medium where the optical signal is the most susceptible to external interference impeding the integrity of the transmitted data. In particular, free space optical (FSO) communication systems, which uses the atmosphere as the primary transmission medium, are disturbed by additional atmospheric scattering effects [1-5]. It has been shown that transmission wavelengths in the mid-infrared spectral range can help reduce these atmospheric effects and improve transmissivity of the link [1, 4-13]. Therefore the study and development of devices capable of achieving mid-infrared characteristics is essential in the adaptation of modern FSO links for mid-infrared functionality.

1.2 Motivation

Recent work in free space optical communication has shown great promise by increasing efficiency using mid-infrared transmission wavelengths [4-12]. The difficulty in implementing mid-infrared FSO links lies in the construction of capable technology to achieve such feats. Thus, this study focuses on one specific aspect of a modern FSO system; entitled the reflective modulator. This particular device is more commonly employed in systems with at least one mobile station, such as unmanned aerial vehicle (UAV) communication and secure point-to-point communication between nautical vehicles, but can be implemented to function in other analog or digital data transmission systems. Designing a reflective modulator device for mid-infrared

operation is important to determine the efficacy and feasibility of implementing such a device in an FSO system.

1.3 Obstacles in Modern Optical Communications Links

Among the atmospheric effects inherent to FSO systems, there are other physical drawbacks that can also impede the performance of the link. Gaining and maintaining alignment of the line of sight (LoS) between transmitter and receiver (often referred to as pointing and tracking) can propose a difficult task in itself. This process takes into account factors such as fixture movement such as building sway and line of sight obstructions that may misalign or physically obstruct the transmission path [2]. Atmospheric turbulence (hot and cold patches in the atmosphere) may also induce beam wandering by altering the angle of arrival of the transmitted beam incident upon the receiver. To address these issues as they apply to FSO systems, a modulating retroreflector (MRR) is used. The use of MRR technology can help reduce the need for pointing and tracking and beam wandering in a FSO communication link [6-9].

1.4 Reflective Modulators

A modulating retroreflector is special type of reflective modulator. It is a device that works by modulating a continuous wave beam and returning the modulated signal to the source via reflective optics [6]. A MRR is essentially the composite of two separate devices: a semiconductor quantum well modulator (QWM sometimes also referred to as simply a multiple quantum well or MQW) and sufficient reflective optics typically a corner-cube retroreflector (CCR) or a semiconductor distributed Bragg

reflector (DBR). The QWM is composed of cascading quantum wells capable of absorbing light energy at a specified wavelength. This structure then works as an optical modulator to the incident interrogation beam. Dependent on the applied electrical bias, the interrogation beam is absorbed as it propagates through the quantum well region effectively modulating the beam. The now modulated beam is reflected back toward the optical source after passing through the QWM region and encountering the subsequent reflective optic. The CCR is a system of orthogonal mirrors capable of reflecting an incident beam back at the same angle of arrival. This layer can also be substituted for other reflective optics such as a DBR [6]. The following section describes the design of a mid-infrared reflective modulators for free space optical communication.

MRR technology is commonly deployed in communication systems with one or more mobile targets; since they have an innate ability to eliminate the need for pointing and tracking the interrogation beam. Such systems include unmanned aerial vehicle (UAV) communication with a stationary mobile station and remote maritime communication links established between naval ships at sea. Though MRRs eliminate pointing and tracking dilemmas, these links are still susceptible to the same atmospheric effects as other FSO communications links. This is highly due in part that FSO links are most commonly employed with near-infrared (NIR) optical sources that are highly absorptive in atmospheric moisture. Studies have shown that increasing the transmission wavelength, into the mid-infrared (MIR) regime and beyond, may significantly improve signal transmissivity [1-2, 11]. Thus, adapting an MRR device for mid-infrared operation is a natural progression. This process includes the careful

selection of compatible semiconductor materials and design of a composition of semiconductor devices that are capable of both absorbing and reflecting the desired MIR wavelength. In this dissertation, the intricate process is explained thoroughly.

1.5 Dissertation Organization

This dissertation will proceed as follows: Chapter 2 provides a detailed look at the reflective modulator types, structures, and each subcomponent. First the quantum well modulator region is discussed followed by the distributed Bragg reflector region. The device functionality (including schematics) is presented in greater detail, further discussing the design constraints and considerations. Also in this chapter, the basics of molecular beam epitaxy as well as the growth methods used are discussed and concluded with optical characterization techniques used in analysis of the structure.

Chapter 3 presents the simulation and design concepts of each subdevice. Simulations and design diagrams are shown for the mid-infrared MRR implementation. The selection criterion for transmission wavelength, structural consideration, and optimization are also presented. The process for simulating the refractive indices in the MIR spectra is presented as well as the final device design. Chapter 4 then briefly outlines the experimental methods of optical characterization used to evaluate the device quality.

Chapter 5 discusses the fabrication process of the entire MRR device showing detailed RHEED images, MBE parameters, and growth environments. The metallization process is also presented; giving insight on how electrode contacts are embedded in the

device. Chapter 5 is concluded by discussing the cleaving process and analyzing the effects of size on the device.

Chapter 6 covers the MRR device performance and evaluation. Microscopic images and schematics of the final device are shown. Structural and morphological analysis is presented using optical characterization techniques. These optical characterization methods include: transmission, absorption, and reflection spectroscopy.

Chapter 7 presents the relevance of achieved measurements to those from those expected from simulations. The explanations of any data discrepancies from theoretical data are presented here as well. Chapter 7 is then followed by the experiment conclusion, future works, and supplementary documentation.

REFERENCES

[1] S. Ikpe, “Atmospheric Effects on Near-Infrared Free Space Optical Communication Links,” 2009.

[2] S. Bloom, E. Korevaar, J. Schuster, H. Willebrand, “Understanding the performance of free-space optics,” June 2003.

[3] C. P. Colvero, M. C. R. Cordeiro, J. P. von der Weid, “Real time measurements of visibility and transmission in far-, mid- and near-IR free space optical links,” *Elec. Letters* 41 (10). 2005.

[4] P. Corrigan, R. Martini, E. A. Whittaker, and C. Bethea, “Mid-Infrared Lasers and the Kruse-Mie Theorem in Fog for Free-Space Optical Communication Applications,” *Optical Society of America*, 2008.

[5] R. Martini, et. al., “Free-Space Optical Transmission of Multimedia Satellite Data Streams Using Mid-Infrared Quantum Cascade Laser,” *Electronics Letters* vol. 38, iss. 4, pp.181-183, 2002.

[6] W. S. Rabinovich, P. G. Goetz, R. Mahon, E. Waluscka, D. S. Katzer, S. C. Binari, M. L. Biermann, and G. C. Gilbreath, “Cat’s eye quantum well modulating retro-reflectors for free-space optical communications,” 2003.

[7] Rabinovich, W.S.; Gilbreath, G.C.; Mahon, R.; Burris, R.; Goetz, P.G.; Moore, C.I.; Ferraro-Stell, M.; Witkowsky, J.L.; Swingen, L.; Oh, E.; Koplow, J.; Stievator, T.H.; , "Free-space optical communication link at 1550 nm using multiple quantum well modulating retro-reflectors over a 1-kilometer range," *Lasers and Electro-Optics, 2003.*

[8] W.S. Rabinovich; R. Mahon; P.G. Goetz; E. Waluschka; D.S. Katzer; S.C. Binari; G.C. Gilbreath; , "A cat's eye multiple quantum-well modulating retro-reflector," *Photonics Technology Letters, IEEE* , vol.15, no.3, pp.461-463, March 2003.

[9] Gilbreath, C. G. ;Bowman, S. R.; Rabinovich, W. S.; Merk, C. H.; Senasack H. E.;, 2000. “Modulating retroreflector using multiple quantum well technology,” United State. “*The United States of America as represented by the Secretary of the Navy* “ (Washington, DC) 6154299
URL: http://www.freepatentsonline.com/6154299.html

[10] T.H. Stievater; W.S. Rabinovich; P.G. Goetz; R. Mahon; S.C. Binari; , "A surface-normal coupled-quantum-well modulator at 1.55 μm," *Photonics Technology Letters, IEEE* , vol.16, no.9, pp.2036-2038, Sept. 2004.

[11] Richard, H. L., “The Atmospheric Transmission of Infrared Radiation from 2-5 microns for slant paths from 35,000 feet to the Upper Limit of the

Atmosphere, A Survey," *National Aeronautics and Space Administration*, Washington, D.C., June 1967.

[12] G. C. Gilbreath, W. S. Rabinovich, C. I. Moore, H. R. Burris, R. Mahon, K. J. Grant, P. G. Goetz, J. L. Murphy, M. R. Suite, M. F. Stell, M. L. Swingen, L. M. Wasiczko, S. R. Restaino, C. Wilcox, J. R. Andrews, and W. J. Scharpf, "Progress in Laser Propagation in Maritime Environment at the Naval Research Laboratory," *Free-Space Laser Communications V*, Proc. Of SPIE vol. 5892, 2005.

[13] G. C. Gilbreath, W. S. Rabinovich, T. J. Meehan, M. J. Vilcheck, R. Mahon, R. Burris, M. Ferraro, I. Sokolsky, J. A. Vasquez, C.. S. Bovais, K. Cochrell, K. C. Goins, R. Barbehenn, D. S. Katzer, K. Ikossi-Anatasiou, M. J. Montes, "Large-aperture multiple quantum well modulating retroreflector for free-space optical data transfer on unmanned aerial vehicles," *Society of Photo-Optical Instrumentation Engineers* 2001.

[14] E. Korevaar, I. Kim, B. McArthur, "Debunking the recurring myth of a magic wavelength for free-space optics," Proceedings: SPIE 4873, 155. 2002.

CHAPTER 2

CONCEPTION OF MID-INFRARED REFLECTIVE MODULATORS

The concept of a reflective modulator (RM) device has been around for over a decade with many various implementations and applications. The adaptation of RM technology for applications (primarily communications) is the mid-infrared is an innovative direction for these well-known concepts and is the main focus of this experiment. Most frequent implementations of the RM utilize multiple semiconductor quantum wells (MQW) to achieve optical modulation through the phenomena of electroabsorption. This has proven most useful in applications such as free space optical communications. Most notably, the modulating retroreflector device designed and patented by the Naval Research Lab (NRL), which is capable of 10 Mbit/s modulation speeds using a MQW implementation [9,13]. Figure 2.1 demonstrates the basic operation of this device.

a)

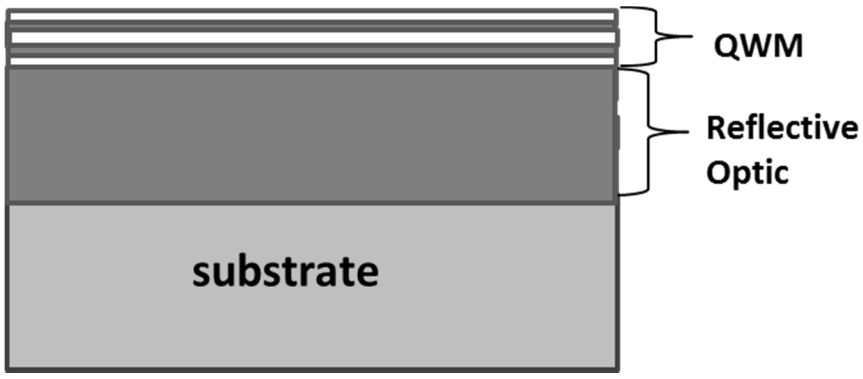

b)

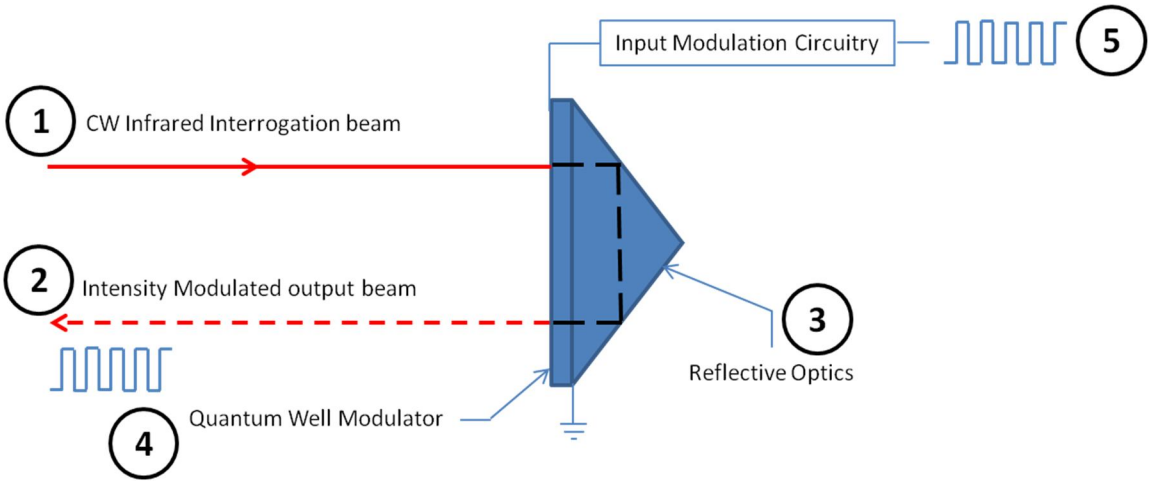

Figure 2.1 a) Schematic of a sample modulating retroreflector (MRR). **b)** Diagram of MRR operation [9]. 1) An interrogation beam is sent (via transmitter) to probe data from the MRR. 2) The reflected beam is optically modulated containing the inquired data for the receiver. 3) The reflective optic (Corner Cube Retroreflector or Distributed Bragg Reflector) returns the modulated beam to the receiver. 4) The Quantum Well Modulator (QWM) region acts as a shutter to achieve optical modulation. 5) Input signal (circuitry) containing information for the receiver.

Considering this implementation, RM devices can be broken down into two smaller semiconductor devices for simplicity: the multiple quantum well modulator and the reflective optic each of which explained in further detail in the sections below.

2.1 Quantum Well Modulator

The quantum well modulator region of a RM is essentially responsible for converting a continuous wave interrogation beam from a remote location probing for information, into an optical intensity varying beam containing the requested frequency modulated data as specified by an electrically driven external input frequency. An interrogation beam is incident upon the multiple quantum well region on one end and exits the region modulated according to the applied bias. The rate and efficacy of achievable modulation is dependent primarily upon the physical characteristics of the quantum wells. Figure 2.2 shows a sample QWM structure.

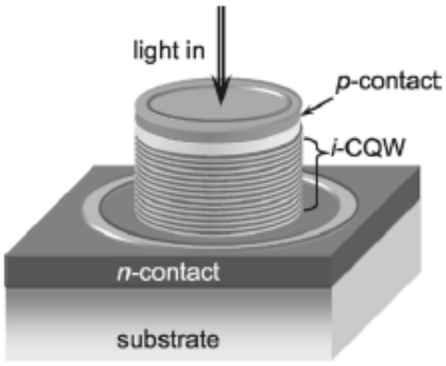

Figure 2.2 Schematic of a quantum well modulator [10].

Devices with large surface areas have improved absorptive properties than those that have a much smaller surface area simply because they cannot produce as many photoelectrons (electrons generated from single photon absorption) as their larger counterparts. Conversely, the smaller devices are generally much faster because the generated photoelectrons do not travel as great of a cross-sectional distance and less susceptible to resistive and capacitive effects that arise (at the contact regions) in large devices. Therefore a compromise is ever present between device speed and absorption efficiency. Thus, the development of the QWM requires the utmost consideration and planning to attain sufficient electroabsorption at the desired wavelength(s) specified for device operation with the desired operation specifications. The specific design considerations of each RM component are given in the following section.

2.1.1 Quantum Wells and Intersubband Electroabsorption

Physically, a quantum well is essentially a thin small bandgap semiconductor material layer confined between two thicker, larger bandgap semiconductor materials. In this particular case, we consider a GaAs quantum well(s) with $Al_xGa_{1-x}As$ barriers on

either side. Very thin (less than 100 Å) semiconductor materials have drastically different absorptive and transmissive characteristics than opposed to that of the bulk material. Bringing two semiconductor materials into close contact, forming an abrupt junction, will cause energy discontinuities in the valence and conduction bands at the junction of the materials. This discontinuity in conduction band energy creates a well-like region in which free electrons may reside. Within each well there are specific energy states in which the probability of an electron residing at that particular energy is very great. If within the well there exists multiple states, then an electron can absorb incident energy (greater than the difference of the energy states) and transfer to a higher energy state. The width and height of the well can be adjusted in order to achieve free electron absorption within the wells confined energy subbands [15,16].

Quantum well electroabsorption refers to a well's affinity to excite a free electron in the well ground state up into its first excited state [16].Depending on the well thickness, the well's subbands can lie nearly collapsed on top of one another near the bottom of the well (for sufficiently thick quantum well layers) or toward the top of the well (for very thin well layers). In some cases, the subband energy can lie slightly above the quantum well itself and collapse down into the well when an external force is applied across the well. This electroabsorption can only take place when there is an applied electric field to invoke this bound-to-extended transition [17]. It is also possible to have the excited state(s) also bound within the quantum well or reside slightly above the quantum well in the vacuum continuum. These transitions are known as bound-to-bound and bound-to-continuum transitions respectively. The bound-to-bound and

bound-to-extended transitions have proven successful and greatly simplify design and are the primary transitions sought after in the devices designed for this dissertation. Each of these processes requires an external optical energy source to promote this carrier excitation by carrier-photon interaction. The electroabsorption process is illustrated in Figure 2.3 below.

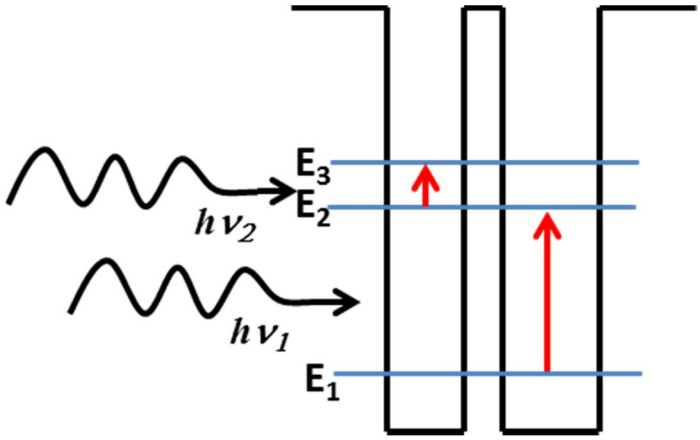

Figure 2.3 Multiple quantum well (MQW) electroabsorption schematic. Free electrons in the ground state (E1) are excited to elevated states (E_2 and E_3) by the incident photon energy $h\nu_1$and $h\nu_2$.

Sufficiently thin quantum wells result in the formation of intersubband energy levels within the well that provide discrete states in which can reside. The separation of these energy levels determines the wavelength(s) of incident energy that can be absorbed within the well. Varying the well width, in turn, adjusts the intersubband separation. The thinner the well, the greater the intersubband energy separation, as the energy levels are forced up toward the top of the well. Conversely, increasing the well width results in the collapse (downward to the bottom of the well) of the intersubband energy level spacing, hence reducing the absorption peak wavelength(s) of the quantum well. The GaAs/$Al_xGa_{1-x}As$ material system has inherent optical limitations due to a

crossover point (x= .45) where the direct band gap associated with the Γ band becomes indirect and undesirable for optical devices. For this specific reason, a double tunnel barrier quantum well is asserted to negate this restraint.

In order to achieve intersubband electroabsorption of any kind, intuitively, there must be available carriers in the well's ground state to be promoted into a higher energy level. This is done by sufficiently doping (adding additional impurities to introduce free electrons or holes carriers; this is known as an extrinsic device) the quantum well layer. The free carrier concentration of the well is solely dependent on the application of the quantum well device. Heavily doping the well so that there is a very dense population of carriers available increases the likelihood of electroabsorption. This is quite simply because the more available carriers there are, the more likely one of those carriers will absorb the incident photon energy (provided that that very energy is enough to promote the carrier into an excited state). In this experiment the doping level is held constant (approximately 10^{18} cm^{-3}). An in depth explanation of the design process and considerations, as they pertain to GaAs wells, is given in the next chapter.

2.1.2 Double Barrier Quantum Wells

The confinement of carriers and the wavefunction separation can also be enhanced by adding an additional barrier region on either side of the quantum well (as shown in Figure 2.4). The resultant structure is known as double barrier quantum well (DBQW). These wells were first proposed in 1991 by Schneider [18,19]. By applying ultrathin (~ 2 nm) AlAs barriers on either side of the GaAs quantum well between the

$Al_xGa_{1-x}As$ thick barriers, the first excited state is shifted toward higher energies. This well structure creates an asymmetry that modifies the relationship between photoconductivity and applied electric field allowing such devices to achieve substantial electroabsorption without an applied bias [18,19].

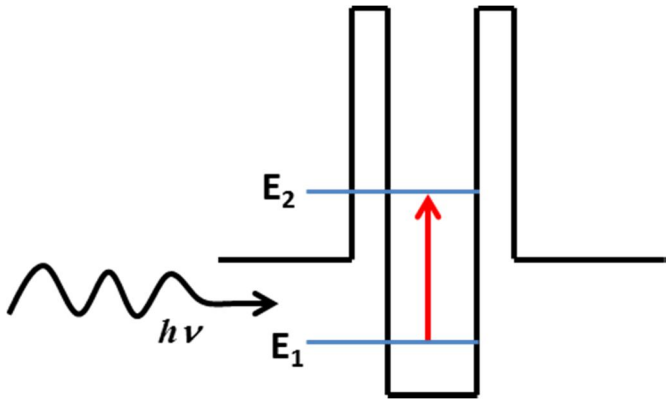

Figure 2.4 Double barrier quantum well structure composed of $Al_xGa_{1-x}As$ (lower barrier), AlAs (tall ultrathin barrier), and GaAs (quantum well).

The structures considered in Schneider (*et. al*) are composed of 25 nm $Al_{.30}Ga_{.70}As$ outer barriers, approximately 2 nm AlAs tunnel barriers, and 4.5 to 5 nm GaAs well. Though the effect of increasing the GaAs well layer from 4.5 nm to 5 nm on electroabsorption is mildly explored in this work, no extensive study relating the physical parameters of the structure currently exists. In order to enhance the optical capabilities of this structure, the relationship(s) between the physical parameters and wavefunctions must be further understood. Therefore, this work explores the effects of manipulating the physical characteristics of the double barrier structure and optimizes each physical parameter (i.e. well width, tunnel barrier width, large barrier height) to yield a quantum well structure capable of higher well confinement and

electroabsorption in the 3-5 μm range. This design and optimization process is further described in the subsequent chapter.

Similar to the traditional rectangular quantum well structures, applying a bias across the DBQWs induces a quantum-mechanical band bending which effectively increases the intersubband energy separation within each quantum well (due to a phenomenon called the Franz-Keldysh effect). This increase in the band separation, allows for the absorption of higher energy photons. When the bias is removed, the bands return to their equilibrium position, with the energy bands lying closer to one another. When the intersubbands lie respectively close to one another, lower energy photon absorption occurs. The shifting that occurs is also a function of the applied bias [20]. The greater the applied bias, the greater the shift. Unlike the single barrier structures, DBQWs are susceptible and in fact encourage carrier tunneling through the ultrathin barrier into the well created by the AlAs thin barriers and the $Al_xGa_{1-x}As$ barriers [18]. This effect helps to reduce the background noise associated with quantum well detectors devices.

2.1.3 Quantum Confined Stark Effect

The intersubband energy level is most essential in the adaptation of a RM device for mid-infrared applications. Since the separation of the intersubband energies is far smaller than that of the interband (conduction band to valence band) energy, lower energy emission (such as those attributed to mid-infrared emissions) can be more easily detected. This is but one of two vital function of the multiple quantum well region in RM

devices. The other is the phenomena known as the Quantum Confined Stark Effect (QCSE). QCSE refers to the shifting of optical absorption peaks in quantum confined well regions as an electric field is applied perpendicularly across the semiconductor layers. This external force causes exciton resonance to shift as a result of one-dimensional carrier confinement within the quantum well [21-23]. This shifting of absorption peaks is characteristic of thin layer semiconductor materials. Whereas, in very thick layers, a broadening of the absorption peak is observed due to the bulk phenomena such as the Franz-Keldysh effect [21]. Therefore, thin multiple quantum well structures are very attractive for optical modulation applications such as free space optics.

The exciton resonance can be notably observed at room temperature quite easily in thin layer quantum wells due to carrier confinement. Applying a perpendicular electric field across the wells, will affect the bound states with in the well, as one side of the quantum well drops in energy slightly increasing (or decreasing) the wells width [20]. This implies that the intersubband's spacing can be modified with the well width (assuming that there exist discrete subbands within the well for bound-to-bound transitions). The energy levels can be brought closer together or drawn further apart by decreasing or increasing the well width respectively (polarity dependent) [24]. When the applied electric field varies in polarity, intensity, or frequency (as in AC signals), the quantum wells behave as an optical shutter of sort; absorbing or transmitting the incident wavelength(s) energy dependent on the applied field. This is the primary concept in optical modulation explained by QCSE in multiple quantum wells. Figure 2.5 depicts the optical shutter process utilizing the QCSE phenomena.

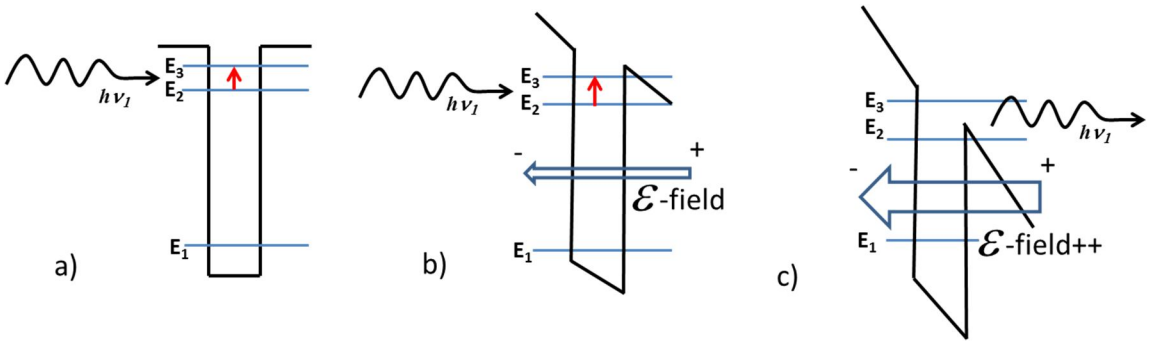

Figure 2.5 a) A single quantum well structure with subband energy levels E_1, E_2, and E_3 under no external electric field. The incident energy $h\nu_1$ is sufficient to invoke absorption from the E_2 level to the E_3 level. **b)** The single quantum well with a slight electric field applied across (perpendicular to the semiconductor layers) the well. The applied electric field reduces well width slightly separating the subband energies E_2 and E_3. The incident energy $h\nu_1$ is still sufficient to invoke E_2-E_3 electroabsorption. **c)** Increasing the applied electric field across the well, further decreases the well width and therefore increase the intersubband energy separation. The incident energy $h\nu_1$ is no longer sufficient to cause E_2-E_3 electroabsorption as the E_3 energy level has moved out of the well in to the continuum.

The absorptive/transmissive characteristics of any particular quantum well structure can be altered in real-time to achieve desirable functionality. The form of optical modulation described above acts as an optical shutter opening (transmitting) and closing (absorbing) the available transmission window to the incident energy. To accomplish this effectively, a few device considerations and compromises must be evaluated. The ability for the QWM region to effectively act as a shutter device depends on the number of cascading quantum wells, though increasing the number of wells will directly increases the overall thickness of the QWM region. Increasing the thickness of this region has an adverse effect on the reflected power of the modulated beam. Similarly, QWMs intended for high reflected power operation need to be highly transmissive to the interrogating beam. This in turn implies that the QWM thickness must be small, hence reducing the total number of quantum well structures and the quantum efficiency of absorption in the region.

The design considerations for each RM QWM region are application specific. Therefore, in this particular FSO implementation, an intersubband QWM is design is chosen to achieve mid-infrared wavelength absorption within the atmospheric transmission window (3-5 μm). The peak absorbance, response wavelength, and optical bandwidth of the device are all dependent on width, height, and doping of the barrier regions of the quantum well [25]. With a plentitude of possible well configurations, the QWM is very flexible and can be tailored to meet the demands of this FSO application. The use of doped multiple thin wells allow for the intersubband absorption of mid-infrared wavelengths. Since this study is not particularly concerned with high power return to the receiver, the size of QWM is designed to achieve substantially intersubband absorption and moderate transparency. The shutter operation is achieved by applying an input signal (in this case an alternating square bias) across the QWM region. The speed at which the quantum wells can switch from absorbing to non-absorbing (shutter) is dependent on the physical size of the device [26]. Increasing the device's physical size increases the associated device capacitance which reduces the maximum switching speed. Inasmuch, the aperture size of device also increases with the physical size of the device presenting yet another compromise that must be considered in QWM design.

Mid-infrared absorption is achievable in QWM through intersubband transitions (ISBT). The aperture size and switching speed of this device is moderate since the physical size of the devices is centimeters squared in area. The well structures are designed to be substantially thin and are cascaded to improve absorption efficiency. The

overall thickness of the region is designed for ease of transmission. With these parameters in mind, a QWM can be designed for a mid-infrared RM device in FSO communication.

Other quantum well characteristics, such as material composition and lattice strain, play a significant role in the innate absorptive ability of the structure. Materials with very similar atomic spacing (lattice constant) are said to be “lattice matched” materials. Lattice matched materials can be epitaxially deposited in thin layers upon another lattice matched material with negligible to no atomic strain. Atomic strain may lead to the introduction of undesired states (defects) within a quantum well device proposing numerous growth and fabrication complexities. Inasmuch, atomic strain may also be manipulated to produce devices able to achieve energy states (and therefore electroabsorption) that may otherwise be unattainable given certain semiconductor material systems. These devise are known as strained-layer devices. The quantum well design in this work utilizes Aluminum Arsenide (AlAs) and Gallium Arsenide (GaAs). Two very well-known and frequently utilized latticed matched materials. Therefore, the MQW region of the device presented in the is dissertation considers a AlAs/GaAs device with negligible atomic strain. Similarly, the same principles are in affect when designing the reflective optic region of the MRR device using AlAs and GaAs materials.

2.2 Reflective Optics

In a MRR device, the purpose of the reflective optic is to control the propagation direction of the optically modulated return beam to the receiver in a FSO

communication link. This portion of the device is a very smooth mirror-like surface that reflects the interrogation beam after optical modulation. There are two very different reflection mechanisms that may be employed by the reflective optic device of an MRR. They are retroreflection and specular reflection. Each mechanism is discussed in further detail in the sections below.

2.2.1 Reflection Mechanisms

The first reflection mechanism is retroreflection. In retroreflection, the interrogation beam is incident upon a retroreflective device and is reflected at 180° from its incident angle. Retroreflection is achieved through the use of a micro electromechanical system (MEMS) device called a corner-cube retroreflector (CCR) which will be further described in the subsequent section [6-8]. This method of reflection is most commonly employed in applications where the interrogation beam must return the optically modulated information back to the original source. In particular, FSO communication between a stationary unit and at least one mobile unit, such as unmanned aerial vehicle (UAV) communication systems employed by the Naval Research Labs (NRL) [6-10]. This device eliminates the need for any pointing and tracking system needed to maintain a consistent link between the transmitter and receiver while the receiver is in motion; since the interrogation beam will always reflected directly back to the source. Furthermore, this method of reflection is very versatile and capable of being implemented from short to very long optical path lengths.

The second reflection mechanism is known as specular reflection. In this method, the interrogation beam is reflected off a smooth surface and is reflected at an equal but opposite angle as the incident beam. This method of reflection is characteristic of mirrors and mirror-like devices. In devices designed for quantum well modulation, it is of the utmost importance that the reflective device be capable of sufficient reflection at the wavelength(s) applicable to achieve the task at hand. Henceforth, the type of reflective device chosen is based primarily on preference and applicability. The most common reflective optics employed in RM devices are discussed in the following section.

2.2.2 Types of Reflective Devices

This section reviews the reflective devices used in modulating reflectors. Though there are a plethora of implementations for each type of device, the fundamental concepts of each remains to achieve reflection with minimal signal loss. The manner in which each device achieves reflection is quite different and is thoroughly discussed below.

I. Retroreflectors

Retroreflective devices can typically be divided into two subclasses: corner-cube (CCR) and cat's eye retroreflectors. The former represents the class of devices that achieve retroreflection through the use of three perpendicular reflective (mirror-like) surfaces strategically placed in order to form a cubic corner in which the mirror corners come into contact with one another. In doing so, retroreflection can be achieved as

incoming photons from any angle (assuming the mirrors are fabricated to reflect the incident wavelength) through a series of mirror refractions. The consequential reflected beam returns parallel to the incident beam offset by the size of the reflective surfaces. This type of retroreflector is not typically employed for long range systems. With this implementation, fades inversely with range ($1/R^4$) [6]. This is attributed to beam divergence both from the incident and return beams.

The second type of retroreflector is more commonly associated with longer range applications through the use of coupling optics and spherical mirrors to increase numerical aperture [6,7]. This effect is achieved using a transparent aspheric lens with a focal length equidistant to the curvature of the reflective surface. The use of cat's eye retroreflectors also allows for the development of much smaller MRR devices. Such is not the case for CCR devices since the retroreflection mechanism can only be optimized when the device size is approximately equal to the aperture size [7].

II. Distributed Bragg Reflectors

Distributed Bragg reflectors (also referred to as Bragg mirrors or dielectric mirrors) are mirror devices capable of high-reflectivity at a specific design (or center) wavelength. They consist primarily of periodically alternating layers of high and low refractive index materials of approximately a quarter-wavelength (design wavelength) in thickness and a single period thickness approximately half the wavelength [25]. Each layer is symmetrically grown as shown in Figure 2.6.

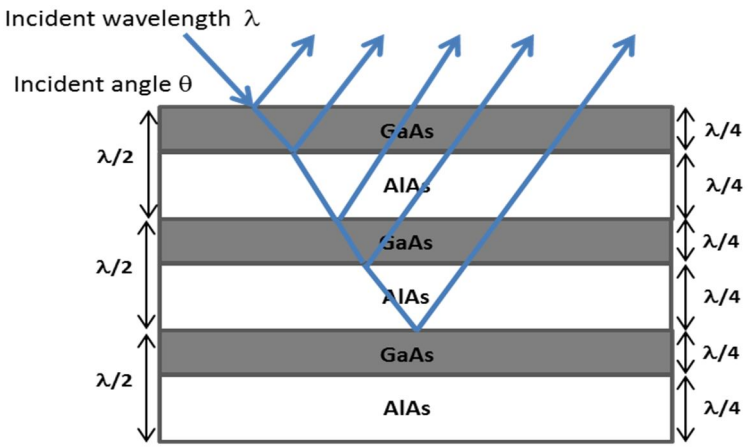

Figure 2.6 A schematic of a quarter-wave Bragg mirror similar to that seen in [26].

The reflectivity of these mirrors is determined by the ratio of the high refractive to the low refractive index. This ratio is known as the refractive index contrast ratio. The larger this ratio is the greater the associated reflectivity is for a specific number of layers. This dispersion phenomenon can be described by the Bragg condition for quarter-wavelength reflectors. An electromagnetic wave travelling in an optically dense medium n_1 (refractive index > 1) is subject to partial reflection back into the primary medium when incident upon an abrupt interface between the medium and a denser medium (n_2). The reflected wave is π radians out of phase with the incident wave at the n_{12} interface. Similarly, a portion of the electromagnetic wave is also transmitted into the subsequent medium reflects at the n_{21} interface. At this interface, $n_2 > n_1$ and reflects out of phase from the n_{12} interface. When the reflected wave travels a distance d_2 back across the medium, it interferes constructively at the n_{12} interface and is once again in phase with the incident wave. The resultant reflectivity spectrum is a compilation of constructive and destructive interference fringes additive at each interface. Figure 2.7 further illustrates this concept.

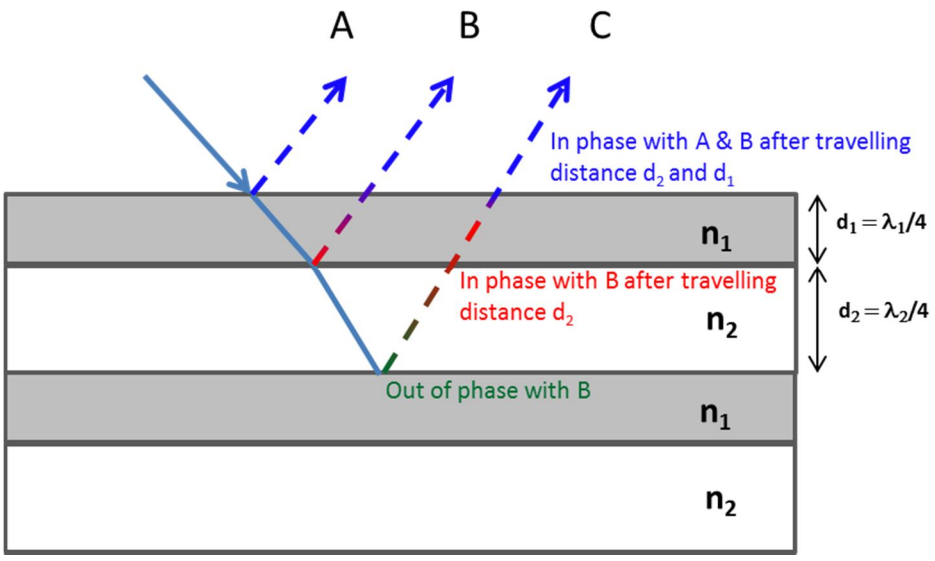

Figure 2.7 Schematic of the Bragg Reflection mechanism.

The selection of materials for DBR devices plays a large role in the physical thickness of the mirror device. Since the thickness of each layer in the DBR is directly proportional to $\lambda/4$ (or a quarter of the design wavelength) and the layer thickness is also inversely proportional to the materials refractive index, then mirrors designed for long wavelengths will initially imply thicker layers be deposited for any given material. In order to design a thinner mirror and the same long wavelengths, materials with substantially large refractive indices must be used. Moreover, increasing the number of periods (alternated pairs) will increase the mirror's reflectivity at the specified design wavelength [16]. Thus, applications that require high-reflectivity are typically much thicker than those that do not. The application for which the mirror is designed can also limit the mirrors reflective capabilities. The polarization of the incident light and its angle of incidence are application specific and are not flexible to the device design [16]. The total number of periods used and the material composition of each layer must be chosen carefully in order to produce the desired mirror device.

The reflectivity spectrum for DBR devices can be simulated as a function of incident wavelengths. In order to determine the percentage of the incident light that is reflected by the mirror, the refractive index of the materials must be determined. The refractive index is a measure of how well a particular wavelength propagates through a material as opposed to the free space, thus it can be described as a function of wavelength. Using Sellmeier's empirical relationship between refractive index and wavelength, the refractive index can be determined for each material at every wavelength within the spectrum in consideration. The spectral range in which the Sellmeier's relation is valid varies with each material, therefore when designing DBR devices it is imperative that materials are chosen with an overlapping spectral range so that a design wavelength can be selected that can be effectively modeled in each material layer. In this experiment gallium arsenide (GaAs) and aluminum arsenide (AlAs) are the materials selected for DBR design. A significant problem occurs when attempting to design a mid-infrared DBR considering these two materials. The parameters, known as Sellmeier's coefficients, for AlAs are undefined for mid-infrared wavelengths, thus the refractive indices for AlAs cannot accurately be determined for wavelengths above 2.2 μm [13]. Therefore, determining the reflectivity spectrum for a DBR device with a mid-infrared design wavelength will be undefined. In order to accurately model the reflectivity spectrum for GaAs/AlAs DBR devices, these parameters must be determined. Using the single effective oscillator (SEO) model, the Sellmeier equation can be simplified and described in terms of the incident energy (eqn. 2.1)

$$n^2(E) - 1 = \frac{E_0 E_d}{E_0^2 - E^2} \tag{2.1}$$

where E is the incident photon energy, E_0 is the single oscillator energy, and E_d is the dispersion energy (strength of interband optical transitions) [21,23]. Using this approximation, the refractive indices for energies (wavelengths) far beyond that of the bandgap of the material can be determined. The invalidity of this approximation worsens as the incident energy E approaches that of the material bandgap energy, but conversely grows more accurate for energies far below that of the bandgap energy [23]. Using previously known values for the dispersion parameters in the near-infrared spectrum, a fitting algorithm is designed to produce newly optimized mid-infrared dispersion parameters that are capable of determining the refractive indices for GaAs and AlAs in the mid-infrared range (λ ~ 2-6 μm) within 2% error [23]. With this information, the DBR reflectivity for a GaAs/AlAs device can be determined as well.

Once the refractive indices for the selected materials are determined, the approximate thickness of each material layer can be found by

$$n_h t_h = n_l t_l = \frac{\lambda_0}{4} \tag{2.2}$$

Where λ_0 is the design wavelength of the DBR device, n_h and n_l are the a the high and low refractive index respectively, and t_h and t_l are the respective thicknesses of each layer [24]. Once these parameters are determined, the reflectivity spectrum of the associated Bragg mirror device can be calculated. Employing a transfer matrix method (TMM) algorithm, the reflectivity spectrum can be effectively estimated. Using this

method, MATLAB software is developed to determine the associated layer thicknesses of each material as well as the reflectivity spectrum for the resultant DBR structure.

The physical structure of DBR devices can be very simplistic in nature, but there are major factors that must first be considered when designing such a device. In order to successfully deposit alternating thick layers, it is important that the materials selected have very similar lattice constants (lattice matched), thus thick defect-free layers can be deposited pseudomorphically. Materials with significantly different lattice constants will result in formation of strained layers. Though strained layer asymmetric mirrors have been fabricated, mid-infrared applications are not tested in this particular design [17]. For this reason, the materials selected for DBR growth are GaAs and AlAs due to their pseudomorphic growth compatibility and availability in the growth facility. Furthermore, the difference in refractive index between the two materials is substantial resulting in the largest contrast ratio available in the GaAs/AlAs material system (therefore maximal reflective capability is achieved per number of periods). In order to increase the percent reflectivity for a specific wavelength and alternating materials, the number of repeated periods must be increased. Essentially, implying that a thicker device must be fabricated. The reflectivity of the DBR device is typically application specific and must be considered during device design. For free space application, it is imperative that reflected signal is capable of reaching its receiver target while maintaining its signal integrity [1]. Therefore, high-reflectivity (> 99%) mirrors are typically considered for such applications. Conversely, moderately reflective devices are typically much thinner

than their high-reflectivity counterparts and not typically implemented for FSO applications.

2.3 Device Growth via Molecular Beam Epitaxy

Molecular Beam Epitaxy (MBE) is one of several techniques used to deposit single crystal thin films. It is the premier deposition technique for the growth of semiconductor heterostructures due to its atomic resolution thickness capabilities [10]. Recent growth epitaxial growth techniques allow for the fabrication of very abrupt (sharp) interfaces between different materials and thus the construction of more complex device structures are possible [8]. Since the fabrication of MRR devices requires great control and precision of layer thickness, MBE is the ideal deposition technique for the development of this particular device structure. Great growth precision is achieved through the use of an ultrahigh vacuum (approximately 10^{-10} torr) allowing deposition of monolayer precision of single crystals [27]. The substrate is first heated and cleaned (removed of protective oxide layer) in situ and then the appropriate materials are then deposited thermally dependent. The layer deposition is monitored and analyzed with an electron diffraction technique known as RHEED (Reflection High Energy Electron Diffraction). RHEED can be used to observe the surface morphology of both the substrate and device.

All devices mentioned in this dissertation are grown in either an EPI model 930 or Varian Gen II MBE as shown in Figure 2.8. The model 930 and Gen II MBE

are the primary methods of epitaxial growth in the Compound Semiconductor Research Lab (CSRL) on the University of Missouri campus.

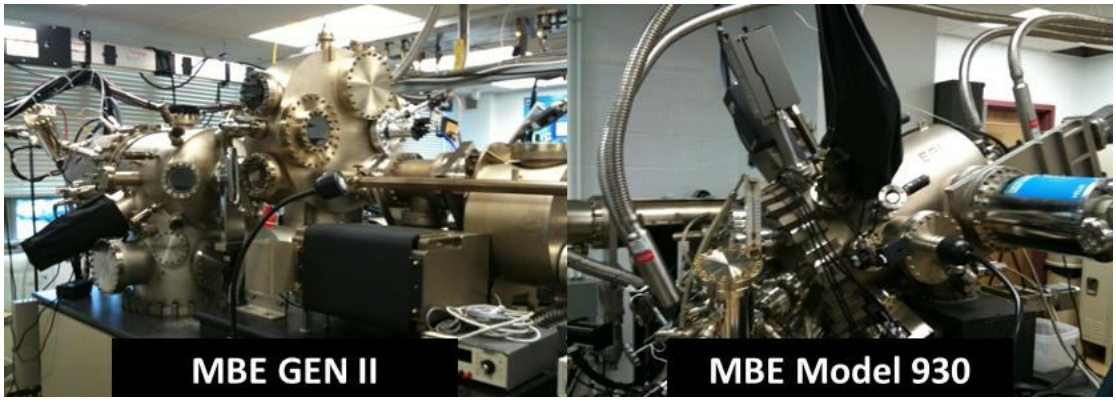

Figure 2.8 Gen II and Model 930 MBE machines in the CSRL in EBW 235 University of Missouri-Columbia.

2.3.1 High Quality Growth with Model 930 MBE

Ultrathin and ultra-smooth epitaxial layers are capable of being grown with the MBE process as new growth methods and techniques have been refined over recent decades. Perhaps the MBE's most valuable feature is its ability to achieve extremely slow growth rates and ultra-refined structures through the use of an ultra-high vacuum (UHV) system and mechanical shutters between substrate holder and the deposition cells. This allows for exact precise deposition with a precision better than 0.1 monolayers in some cases [28-30]. Furthermore, GaAs and AlGaAs were among the first III-V material compositions studied using the MBE techniques, therefore are proven materials for high quality (high purity) device growths. High purity is an essential characteristic when design any optical device as it implies low operating voltages (and

currents), longer device life times, and increased quantum efficiency [28]. The specific growth procedure, as it pertains to this device, is described chronologically in Chapter 4.

The EPI model 930 MBE machine used for the growth of the device considered in this dissertation, is of the solid-source variety MBE. In this MBE methodology, bulk epitaxial materials of the utmost purity are heated up within the Knudsen effusion-cell until sublimation takes place. The temperature at which the effusion-cell is heated is deterministic of the desired flux necessary to achieve proper compound compositions. This flux is measured by a beam flux monitor that can accurately determine the beam equivalent pressure (BEP) within the growth chamber as the gaseous elements enter the chamber. The elemental gases are strategically released from their appropriate shutters through the use of mechanical shutters and then adsorb on the heated substrate surface where they interact to form solid compounds [10]. Due to the ultrahigh vacuum within the growth chamber, the evaporated atoms have exceptionally large mean free paths (distance travelled before encounter another atom) and do not react until the reach the substrate surface, hence forming a “beam” of atoms directed toward the substrate from each individual cell. Figure 2.9 shows a schematic of the interior of an MBE growth chamber.

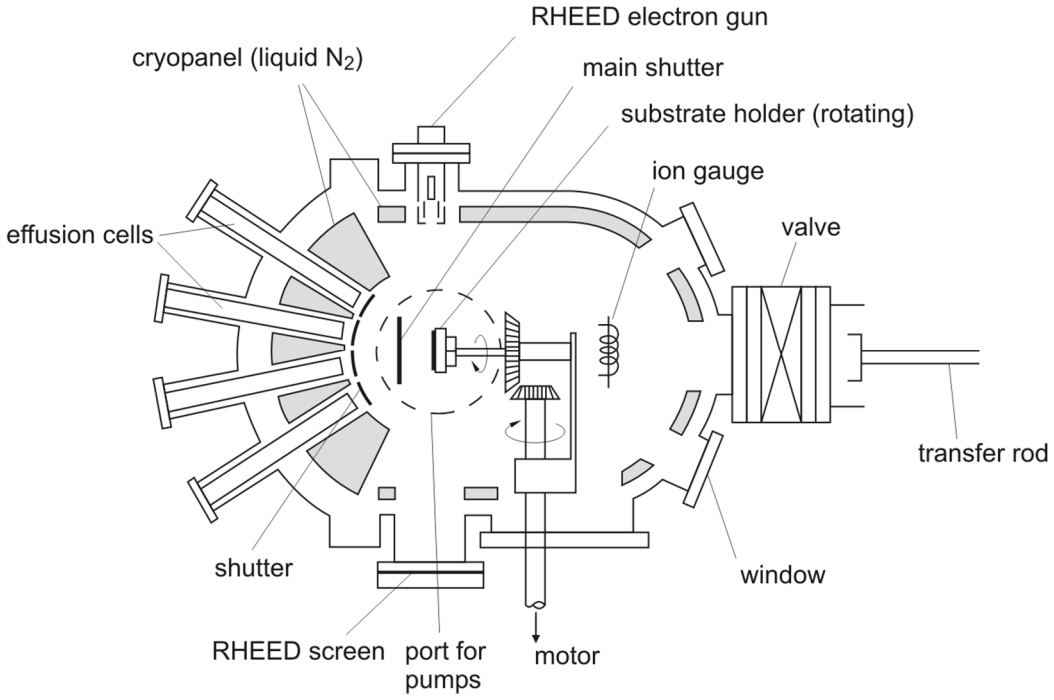

Figure 2.9 MBE Growth Chamber [31].

2.3.2 Reflection High Energy Electron Diffraction

The ability to grow ultrathin layers with great precision using MBE is greatly complemented by the ability to monitor the uniformity of each epitaxial layer in real-time (in-situ) through Reflection High Energy Electron Diffraction. With this technique, valuable information on the device's smoothness and cleanliness can be immediately extracted. Due to the level of surface reconstruction (chemisorption) that takes place during epitaxial growth, it is also possible to monitor the deposition rate of material on the surface of the substrate (Figure 2.10 and 2.11).

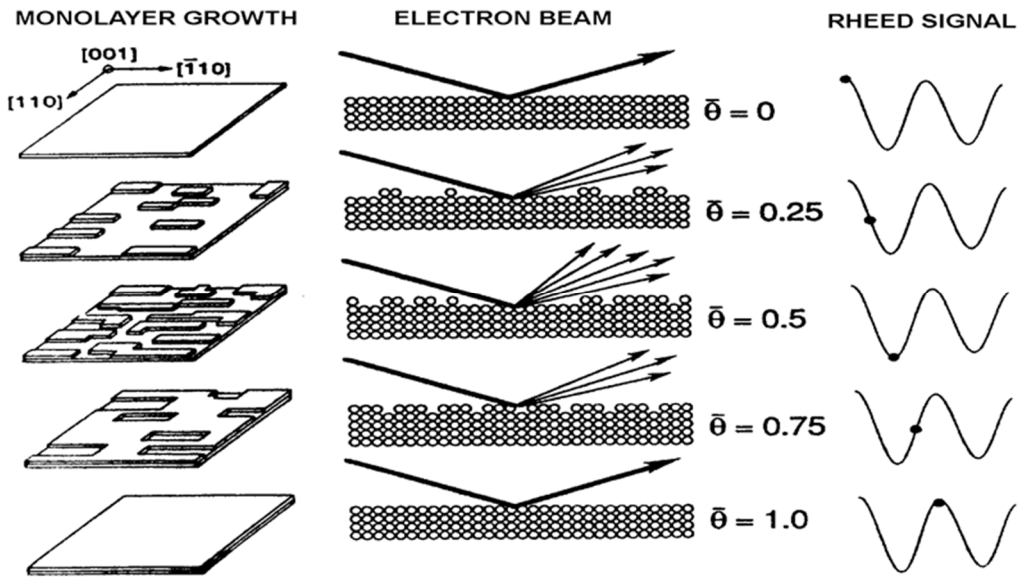

Figure 2.10 Schematic of RHEED oscillation during material deposition [33].

This is accomplished by high voltage monoenergitic electron gun that accelerates electrons at a glancing angle (~1-3 °) to limit the depth at which the electron penetrates) toward the substrate surface. The high energy electron is then incident on a fluorescent screen conveying a diffraction pattern dependent on the surface's morphology as the electrons reflect off the lattice atoms of the substrate [28, 32, 33].

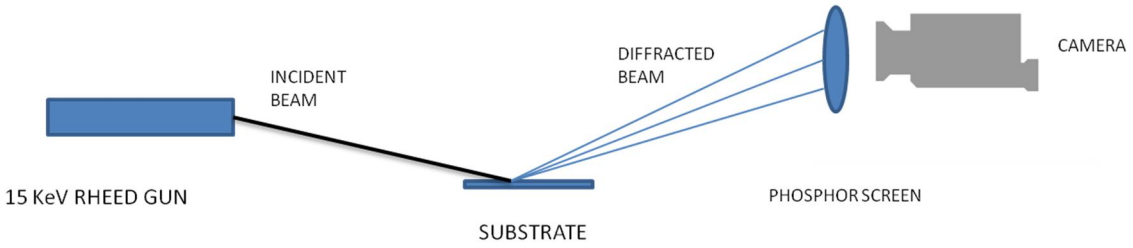

Figure 2.11 Schematic of RHEED *in situ* diffraction monitoring during sample growth.

2.4 Post-growth Characterization Techniques

In-situ techniques, such as RHEED, are beneficial for directly monitoring the quality of the device material as it is being grown within the MBE machinery. It is also very important to analyze the growth quality of the material post-growth to greater understand the device capability and in turn its optimal functionality. There is a plethora of optical characterization methods to fully investigate both the physical and quantum mechanical attributes of any given semiconductor device. Optical characterization is also necessary to evaluate the device performance and the negative effects (due to impurities) that cannot otherwise be assessed during growth. The following section list optical characterization techniques used in the analysis of the RM device of this dissertation.

2.4.1 Photoluminescence

Photoluminescence (PL) is simply the emission of photon energy at certain wavelengths by a semiconductor after being optically excited (pumped) by photon energy at or greater than the band edge. This phenomenon occurs through the spontaneous emission process. As a photon is absorbed by a random electron in the ground state, the electron is promoted into an excited state where it spontaneously releases the quantized energy in the form of a single electron after a spent lifetime (as determined by the material). Due to the conservation of energy principle, the emitted photon cannot have any more energy than the original photon absorbed. Multiple photons can also contribute to this process. When more than one photon is absorbed,

the resultant emission photon can have the same or different energy as the original photon. In some cases the photon may have an energy greater than the photon energy absorbed; provided there are multiple excited states in which an excited electron can reside. Therefore, nonradiative downward transitions may provide additive fluorescent energy [34,35].

The PL procedure is very advantageous technique for deciphering both the physical and quantum-mechanical properties of epitaxial thin layers. It is one of the most widely used optical characterization technique in the semiconductor technology industry due to its non-invasive versatility. Material bandgap and offsets can be determined directly from luminescent peak intensity and spectral location, as well as surface/interface and defect behaviors, amongst other properties, of a particular structure [36]. In this dissertation, the PL method is employed to determine the precise $Al_xGa_{1-x}As$ alloy composition of the double barrier regions, epitaxial surface/interface behavior, doping level, and presence of undesired structural anomalies. The experimental setup is presented as well as the supplemental results are discussed in Chapter 6.

2.4.2 Absorption/Transmission Spectroscopy

Absorption Spectroscopy is associated with a particular material's ability to take in photonic radiation through the transfer of energy. Conversely, transmission spectroscopy can be classified as a material's lack of absorption or its inability to transfer photonic energy. These characterization methods are correlated and are very

useful in determining the wavelength energies that are permissible through a material. In traditional semiconductor materials, the bandgap (E_g) separation between the conduction and valence bands represents the minimum energy required to invoke an electron transition from the valence to conduction band (absorption). Any energy less than the bandgap energy can transmit through the material more easily, therefore, causing little to no absorption between the bands. However, within the conduction band, there may lie several quantized states (or energy levels) in which an excited electron may reside. If there exists more than one available energy subband in the conduction band, an energy E ($< E_g$) may be sufficient enough to excite an electron transition between these subbands. The separation(s) between these intersubbands are much smaller than that of the material bandgap, less transitional energy is required.

Since the energy associated with mid-infrared wavelengths are very low in energy, the intersubband transitions are of the utmost interest for absorption/transmission characterization of mid-infrared devices, since these energies are not nearly sufficient enough to promote interband energy transfer. To ensure that intersubband absorption can take place, there must first be an abundance of electron carriers available in the ground intersubband state to adsorb the incident infrared energy. Doping the quantum well layer excessively with electrons (*n-doped*) implies that the ground state in the conduction band will have free electrons in thermal equilibrium, therefore intersubband absorption is possible. The absorption coefficient is determined by Beer-Lambert's Law of absorption that states the absorption coefficient of a medium

can be expressed as the natural log of the ratio of the reference intensity to the transmitted intensity, thus absorption *A* can be written in form of equation 2.3 below.

$$A = \ln\left(\frac{I_0}{I_t}\right) \tag{2.3}$$

Where I_0 is the intensity of the reference source and I_t is the intensity of the wave after being transmitted through the absorptive medium. The absorption/transmission test setup is further described in Chapter 6.

2.4.3 Specular Reflection Spectroscopy

Reflection spectroscopy is a special case of transmission spectroscopy wherefore incident energy is not transmitted through the bulk of the material, but rather a significant portion of the energy is reflected and scattered at the abrupt surface of the material. This characterization method is very useful in determining surface smoothness/roughness of the epitaxial layer. An ideal uniform layer is very smooth and will exhibit high reflectivity behavior at atmosphere/epitaxial layer interface. Specular reflectance measurements are taken at a 45 degree incident angle and at normal incidence.

2.4.4 Optical Microscopy

Optical microscopy is used to evaluate physical traits at the surface of each sample. Visible light is incident orthogonally to the surface of each sample and is reflected back through a system of lenses. This reflection is then captured by a high-

definition microscope digital camera. From the resultant image, surface aberrations and deep level defects can be assessed using image analysis software. Less rough surfaces and areas of minimal defect appear smooth in the image (implying high reflectance at the surface). Whereas more rough surfaces and areas of defect are marked with darker areas and darkened cavities with varying reflectance intensities due to diffraction at the surfaces and interfaces. This characterization method gauges the layer quality of each epitaxial device, which serves as an immediate indication of optical performance.

2.4.5 Atomic Force Microscopy

Atomic Force Microscopy (AFM) is a scanning force microscopy technique used to develop high definition topography images. Such images are useful in asserting physical surfaces features and material characteristics on a nanoscale. AFM is often used in the surface evaluation of epitaxial layers and is beneficial in determining ideal growth conditions that yield high quality thin film growth. Operated in non-contact mode, this microscopy technique can produce three dimensional high-precision topographic images of a device surface based on the atomic resonance at the sample surface. Profilimetric measurements and feature sizes can be extracted using image analysis software.

REFERENCES

[15] C. M. Herzinger, P. D. Swanson, T. K. Tang, T. M. Cockerill, L. M. Miller, M. E. Givens, T.A. DeTemple, J. J. Coleman, and J. P. Leburton, "Electroabsorption properties of a single GaAs quantum well" *Phys. Rev*. B 44 (24). 15, December 1991.

[16] S. L. Chuang, S. Schmitt-Rink, D. A. B. Miller and D. S. Chemla, "Exciton Green's-function approach to optical absorption in a quantum well with an applied electric field," *Phys. Rev.* B 43 *(2).* 15, January 1991.

[17] M. O. Manasreh, *Semiconductor Quantum Wells and Superlattices for Long-Wavelength Infrared Detectors*, Artech House, Inc. 1993.

[18] H. Schneider, P. Koldi, F. Fuchs, B. Dischler, K. Schwarz, and J. D. Ralston, "Photovoltaic intersubband detectors for 3-5 μm using GaAs quantum wells sandwiched between AlAs tunnel barriers," *Semicond. Sci. Technol.* 6. C120-C123. 1991.

[19] H. Schneider, F. Fuchs, B. Dischler, J. D. Ralston, and P. Koidl, "Intersubband absorption and infrared photodetection at 3.5 and 4.2 μm in GaAs quantum wells," *Appl. Phys. Lett*. 58 (20). 20, May 1991.

[20] D. S. Chemla, T. C. Damen, and D. A. B. Miller, "Electroabsorption by Stark effect on room-temperature excitons in GaAs/GaAlAs multiple quantum well structures," *Appl. Phys. Lett.* 42 (10), 15 May 1983.

[21] D. A. B. Miller and D. S. Chemla, "Relation between electroabsorption in bulk semiconductors and in quantum wells: The quantum confined Franz-Keldysh effect," *Phys. Rev*. B 33, pp.6976-6982, 1986.

[22] A. Harwit and J. S. Harris, "Observation of Stark shifts in quantum well intersubband transitions," *Appl. Phys. Lett.* 50, 685. 1987.

[23] D. A. B. Miller, D. S. Chemla, T. C. Damen, A. C. Gossard, W. Wiegmann, T. H. Wood and C. A. Burrus, "Band-Edge Electroabsorption in Quantum Well Structures: The Quantum-Confined Stark Effect," *Phys. Rev. Lett.* Vol. 53, *22.* 26, November 1984.

[24] A. Krier, "Mid-infrared Semiconductor Optoelectronics," Springer-Verlag London Limited, 2006.

[25] M. H. MacDougal, H. Zhao, P. D. Dapkus, M. Ziari, W. H. Steier, "Wide-bandwidth distributed Bragg reflectors using oxide/GaAS multilayers," *Electronics Letters,* vol. 30, no. 14, July 1994.

[26] Murtaza, S.S.; Anselm, K.A.; Srinivasan, A.; Streetman, B.G.; Campbell, J.C.; Bean, J.C.; Peticolas, L.; , "High-reflectivity Bragg mirrors for optoelectronic

applications," *Quantum Electronics, IEEE Journal of* , vol.31, no.10, pp.1819-1825, Oct 1995.

[27] Cho, A. Y. (ed) 1994 Molecular Beam Epitaxy (Woodbury, NY:AIP)

[28] Robin f. C. Farrow, "Molecular Beam Epitaxy: Applications of Key Materials,: Noyes Publications. Park Ridge, NJ. 1995. *ISBN 0-8155-1371-2.*

[29] Sadao Adachi, "GaAs, AlAs, and $Al_{[x]}Ga_{[1 - x]}As$: Material parameters for use in research and device applications," *J. Appl. Phys.* 58, R1 (1985), DOI:10.1063/1.336070

[30] D. A. B. Miller, "Optical Physics of Quantum Wells," *AT&T Bell Laboratories.* Holmdel, NJ.

[31] *Image: http://web.tiscali.it/decartes/phd_html/III-Vms-mbe.png*

[32] M. A. Herman and H. Sitter, "Molecular Beam Epitaxy: Fundamentals and Current Status," Springer-Verlag Berlin Heidelberg, NY. 1996. *ISBN*: 3-540-60594-0.

[33] M. Ohring, "The Material Science of Thin Films," Academic Press, 1992.

[34] B. E. A. Saleah and M. C. Teich, "Fundamentals of Photonics," 2nd Ed. John Wiley & Sons Inc. 2007. *ISBN*: 9780-471-35832-9.

[35] T. H. Gfoerer, "Photoluminescence in Analysis of Surfaces and Interfaces," *Encyclopedia of Analytical Chemistry*. R. A. Meyers (Ed.) pp. 9209-9231. John Wiley & Sons Ltd. 2000.

[36] S. Perkowitz, "Optical Characterization of Semiconductors," Academic Press. 1993.

CHAPTER 3

SIMULATION AND DEVICE DESIGN

In the previous two chapters, we developed the concept of the reflective modulator device; describing in detail the essential components and their functions as well as the general premise behind such an innovative design. In this chapter, an ideal operational device is simulated and considered for manufacturing design. Each subdevice is considered and designed separately of the other and optimized to exude best functioning performance characteristics. Actual device fabrication restraints will be discussed in the subsequent chapters: Chapter 4: Experimental Implementation and Chapter 5: Device Fabrication Process. The infrared quantum modulator is first considered followed by the distributed Bragg reflector.

3.1 Infrared Quantum Well Modulator Design & Simulation

When designing any quantum well device structure, it is imperative to consider confinement characteristics of the well material. Free carrier confinement refers to a well's ability (or inability) to restrict its free carriers within a given space, in this case, free electrons constrained in two dimensions by the quantum well barriers within the conduction band. The confinement due to the well's potential barriers causes the discretization of allowed energies. The available energies can then be fine-tuned by varying the well thickness and depth. Inside of the well, the electron exhibits standing wave behavior (wave-particle duality) due its mass when confined in two-dimensions.

The probability that the electron will reside at a particular position within the well can be described by the time-independent Schrodinger's wave equation below:

$$\frac{\delta^2\psi(x)}{\delta x^2} + \frac{2mE}{\hbar^2}\psi(x) = 0 \tag{3.1}$$

Where *E* is the total energy of the free electron and *m* is the free electron mass. The solution of this wave equation is of the form:

$$\psi(x) = A_1 \cos Kx + A_2 \sin Kx \text{ where } K = \sqrt{\frac{2mE}{\hbar^2}} \tag{3.2}$$

Considering the boundary conditions of the quantum well, the wave function must be continuous, therefore implying that the wave function goes to zero at each boundary edge.

$$\psi(x=0) = 0 \tag{3.3a}$$

$$\psi(x=a) = 0 = A_2 \sin Ka \tag{3.3b}$$

For a well with left boundary at position x=0 and right boundary at x=*a* for a well width of *a*.

Equation (3.3b) is valid when *Ka* is multiple of π or *Ka*=$n\pi$. The solution to the time-independent wave equation can be written in the form of equation (3.4) after finding the coefficient A_2 by taking the convolution integral of the wave equation. The resulting solution is of the form

$$\psi(x) = \sqrt{\frac{2}{a}} \sin\left(\frac{n\pi x}{a}\right) \text{ where } n = 1, 2, 3,... \quad (3.4)$$

Equating the parameter *K* from equation (3.2) and $n\pi/a$ and solving for the energy *E* yields the approximate total energy levels of the quantum well in thermal equilibrium given by

$$E_n = \frac{\hbar^2 n^2 \pi^2}{2ma^2} \text{ where } n = 1, 2, 3,... \quad (3.5)$$

In order to more accurately determine the intersubband energies associated with each quantum well structure, a Schrodinger-Poisson solver package is used. This software package allows for the configuration and construction of group IV, III-V, or II-V compound semiconductor devices as well as the calculation of its device parameters. Thus, the exact wave functions and eigenvalues can be extracted from any specified well structure. Other important well parameters such as the dipole moment, oscillator strength, and intersubband energy separation can also be extracted and are essential in configuring device functionality.

The primary objective of the MQW design phase of this particular device, is to determine which well structure is best suited for electroabsorption operation at the specified wavelength. This is done through a series of steps using two very different statistical software packages. The first is JMP 9, a statistical analysis software with the ability to effectively model variances between a particular dependent variable and any number of independent variables. The second entitled *nextnano*[3], is a Schrodinger-

Poisson solver capable of modeling quantum statistics. The procedure for determining the selection criteria for a particular mid-infrared quantum well structure is discussed in the following sections. Furthermore, the criteria selected are specific to the device in this dissertation and will vary for other structures and applications.

3.1.1 Design of Experiments using JMP 9

With a particular optical wavelength in mind (application specific), the succeeding step in the design process is to determine the intersubband energy separation corresponding to the desired spectrum and the appropriate combination of materials that will produce the required separation. This is where JMP statistical software is very useful, as it allows the user to weigh the significance of a number of independent variables (or factors) versus a single dependent variable (or response) using linear regression techniques. This essentially allows precise examination and selection, of explanatory parameters. In case of MBE growth, this includes quantum well growth factors such as layer thickness and material composition and responses such as transition dipole moment and oscillator strength. In doing so, a distinct model can be developed correlating the quantum well physical characteristics to the varying quantum-mechanical characteristics associated with the particular well structure. The model can then be used to extrapolate the physical description (layer thickness, composition, etc.) to produce the desired optical properties for electroabsorption.

The first step in developing a design of experiment simulation is to identify which parameters are, in fact, controllable (*factors*) and those that vary in reaction to those

parameters (*responses*). The JMP software package allows the data type of each factor and response to be explicitly defined as continuous, therefore define the relationship between given data points and extrapolated data with a continuous function with a normally distributed error term. The principal factors in this particular design of experiments are the quantum well width, the tunnel barrier width, and the Aluminum composition of the well barrier. Each of these factors is altered to directly tune four specific parameters that help determine quantum well electroabsorption: the intersubband energy level separation, the absorption wavelength (inversely related to the energy separation), the transition dipole moment and oscillator strength. Figure 3.1 depicts the responses and factors as defined by the scope of the device.

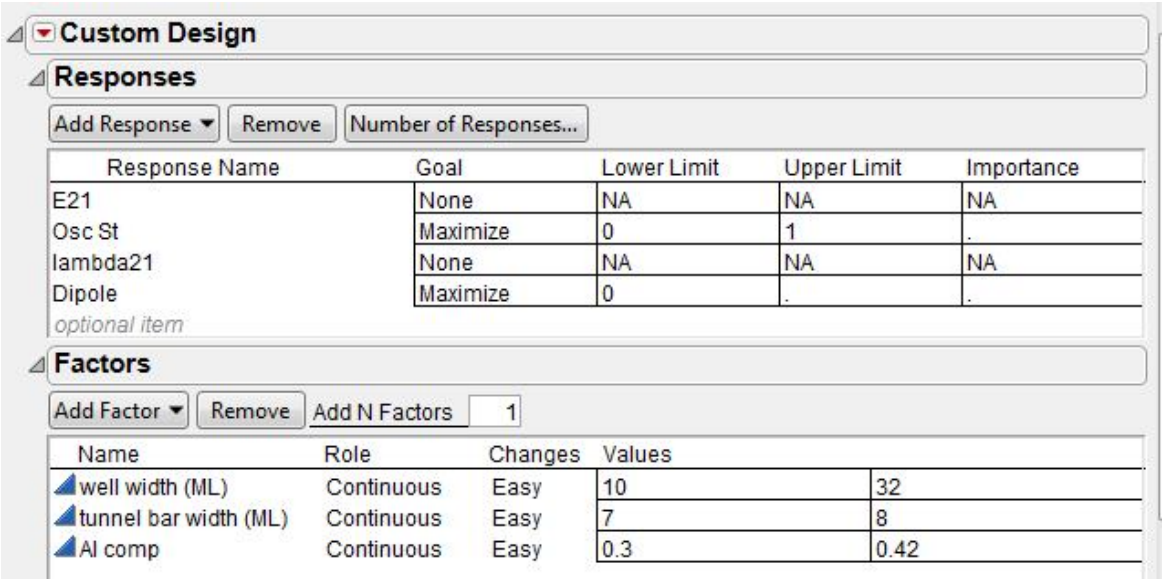

Figure 3.1 JMP 9 design of experiment custom design response and factor definition interface.

Once each factor and subsequent response is defined, precise model parameters can be chosen that describe the variance behavior between the independent and dependent parameters. These parameters are known as the interaction terms. The interaction

terms used to devise this model consist of linear, polynomial, and quadratic terms in order to more precisely weigh the effects of variance between the factors and their responses to produce a fit model describing this variance. Figure 3.2 shows a list of each interaction term explored in the linear regression fit model.

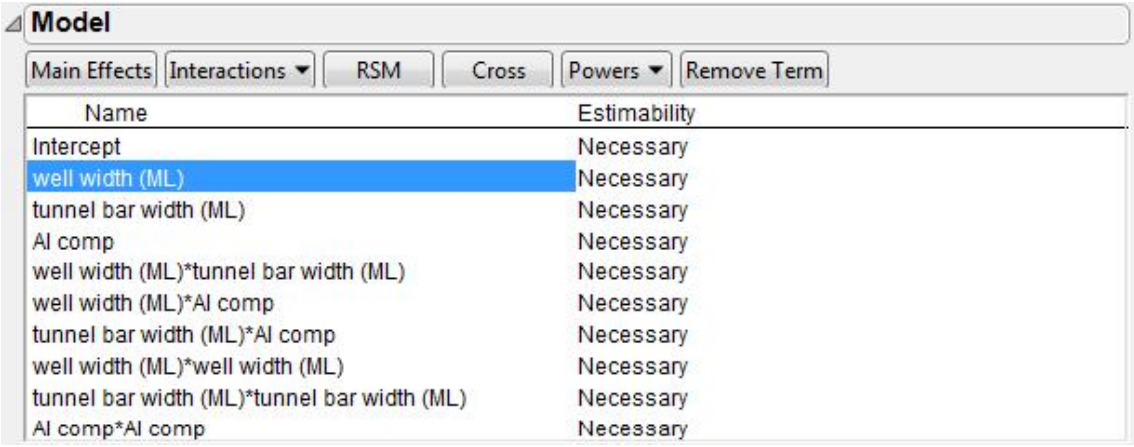

Figure 3.2 Interaction terms used linear regression fit modeling.

Linear regression is a modeling technique used to characterize the relationship between a single scalar dependent variable and a number of independent variables (multiple regression). In this method, a known dataset is descriptively modeled by predictor functions with any unknown data parameters being estimated by the original dataset. This can be more simply stated as

$$y \approx f(X, \beta) + \varepsilon \tag{3.6}$$

where the explanatory parameter, *y*, can be described by a function, *f()* of the independent variable(s) and some unknown parameter β and an additive error term, ε. The aforementioned interaction terms' significance is measured by the variance to the unknown parameter. This is done with the *least squares* method. The least squares

method is a maximum likelihood estimator (assuming a normal distribution) that estimates the unknown parameters to minimize the sum of squared errors associated with the dataset. Thus, the resultant model yields the minimal possible residual values, or variance between the observed and predicted (fitted) data. Using JMP, this variance can be easily visualized with model fit plot and subsequent residual plots. The appropriate fit plots and residuals for each response considered are shown below (Figure 3.3-3.6).

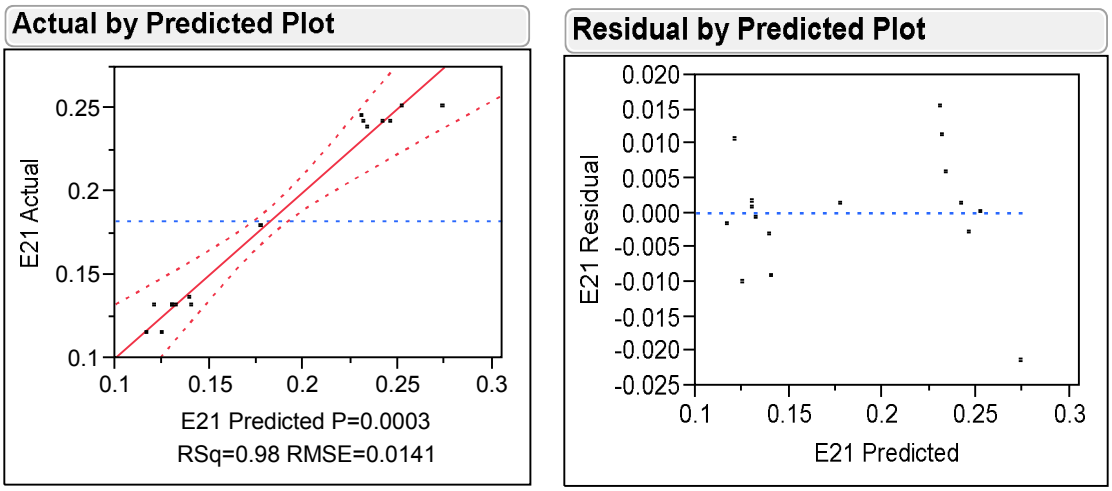

Figure 3.3 Actual vs. Predicted leverage plot and corresponding residual plot of E_{21} separation.

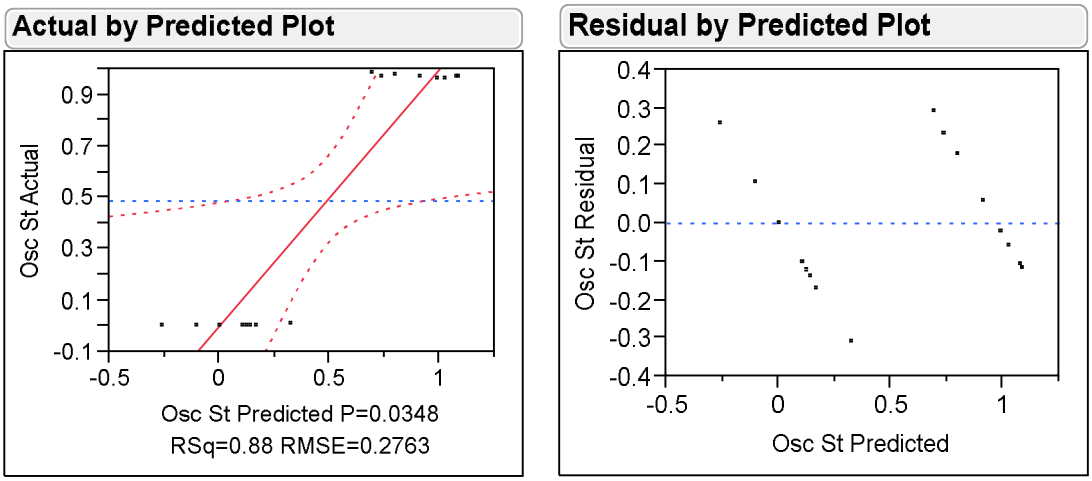

Figure 3.4 Actual vs. Predicted leverage plot and corresponding residual plot of transition oscillator strength.

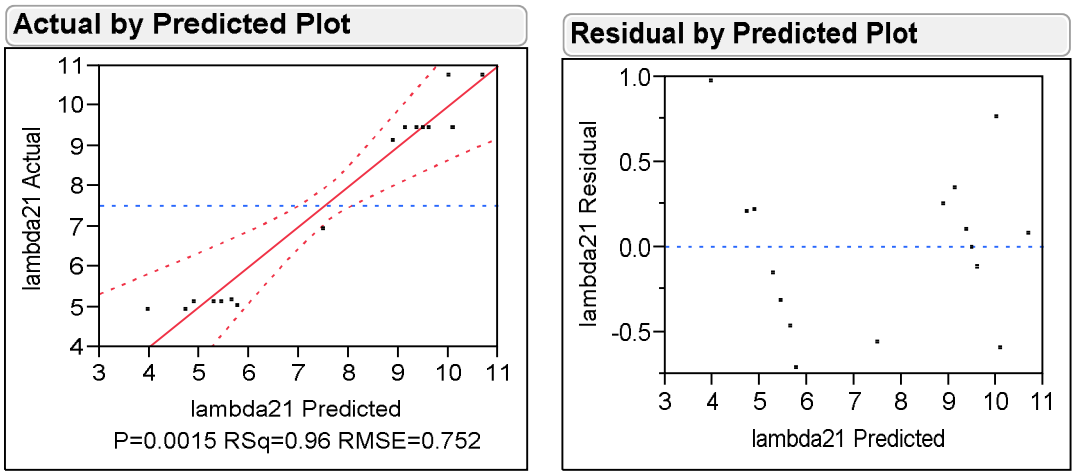

Figure 3.5 Actual vs. Predicted leverage plot and subsequent residual plot of absorption wavelength.

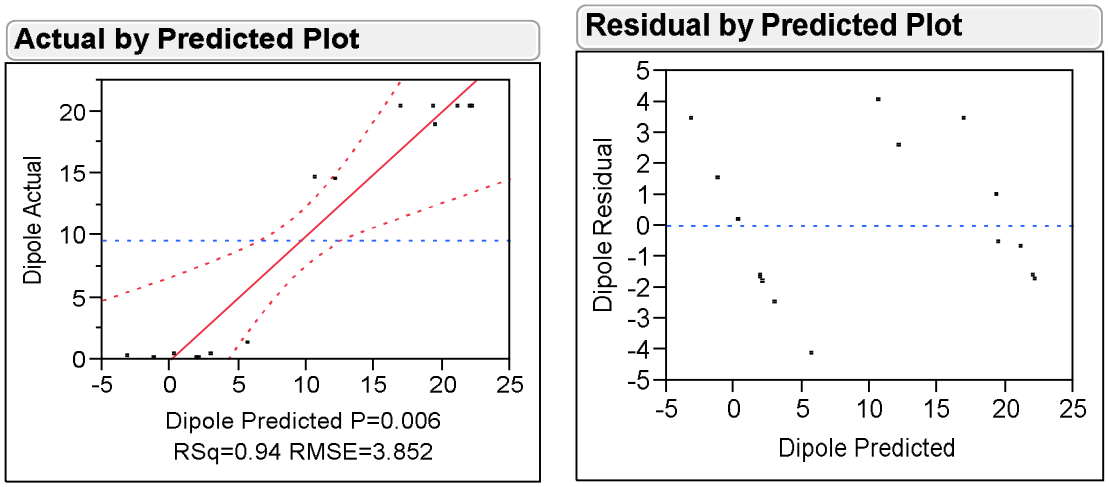

Figure 3.6 Actual vs. Predicted leverage plot and corresponding residual plot of transition dipole moment.

The residual plot is a measure of how much each individual data point (or observations) differs from the forecast value as predicted by the fit model. Essentially, this helps to determine in which regions the generated model is the most effective. Based on the plots of Figure 3.3-3.6, it is advocated that the fit model is a very reasonable predictor of E_{21} separation and the associated absorption wavelength (Figure 3.3 and 3.5). This is suggested by the steepness of the fit line and the corresponding confidence levels. Furthermore, all observations lie within the model space. The residual plots are marked by clustering of data points around the zero line, indicating a low difference between

the actual and predicted values. Conversely, the plots of Figure 3.4 and 3.6 show slight asymptotic behavior toward the mean line and outlier points that reside outside of the prediction space. This indicates that the fit model derived cannot accurately represent the data space. Thus, the explanatory variables, transition dipole moment and oscillator strength, are not easily modeled and cannot be accurately described by the choice of independent factors (These factors are not accurate figures of merit for a design of this particular structure using the JMP package and thus are disregarded, but they are still in fact very important parameters in determining electroabsorptive capability as discussed in the next section). The corresponding residuals show that only a few transition dipole moments and oscillator strengths can be accurately modeled using this fit. This is due to the discrete like behavior of the transition dipole and oscillator strength.

The significance of each interaction terms can then be weighed and screened to form a model expression describing the variance of each response from the mean. These factors are described with leverage plots that show the equivalent pull (or leverage) of the factor on the fit line. Data points that lay farther away from the fit line have a tendency to tilt the line towards itself, whereas data points that lie on or near the fit line have a less significant effect. Inasmuch, the overall strength of the interaction term on the fit model can be measured with each leverage plot. The interaction terms of heavy weight (or high significance) have a fit line and corresponding confidence levels that intersect the horizontal mean line, whereas the terms of low significance show an asymptotic behavior towards the mean line or do not intersect at all; therefore indicating no significant overlap between the fit and the mean of the dependent

variable. Using these figures of merit, the interaction terms can be vetted and disregarded dependent on their ineffectiveness to describe the explanatory term. The most significant leverage plots for each response are shown below (Figure 3.7-3.8).

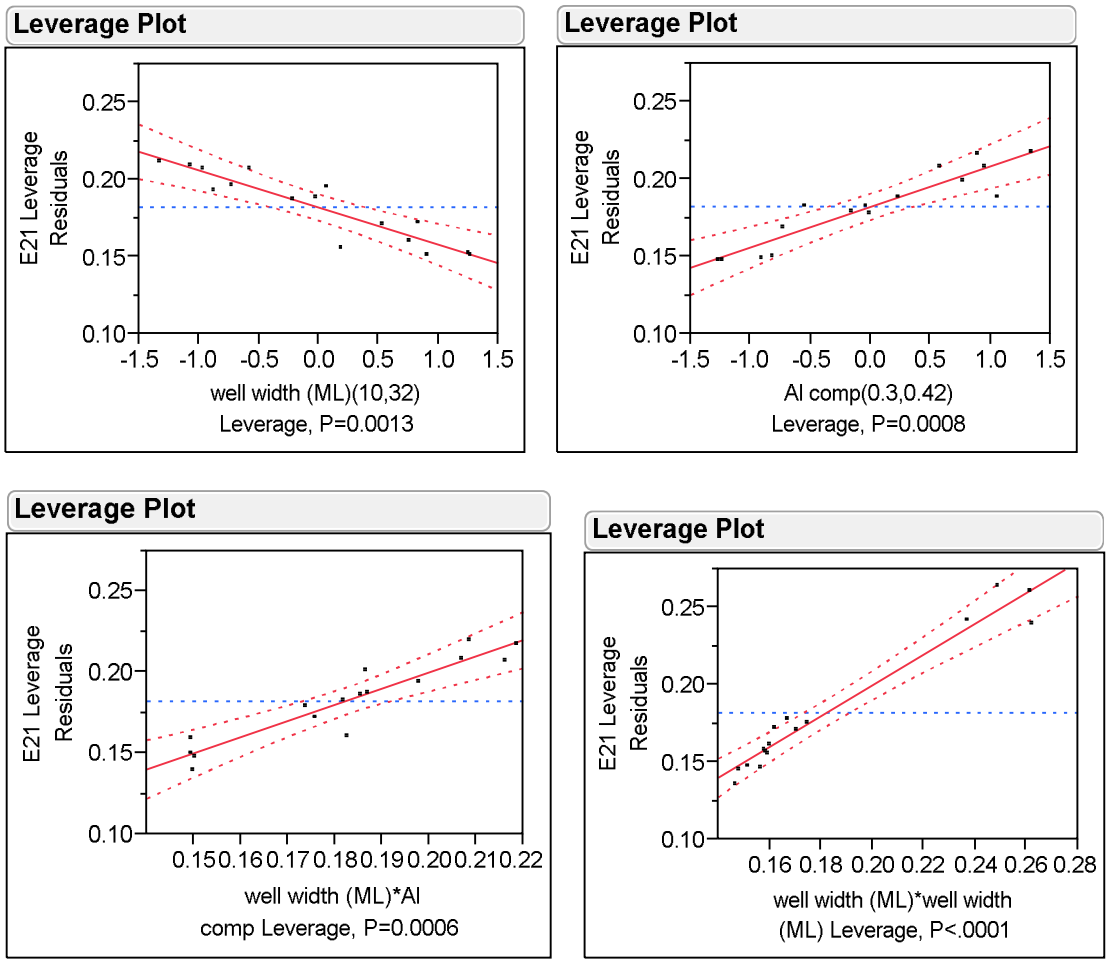

Figure 3.7 Leverage plots corresponding to the most significant interaction terms for E_{21}separtaion fit model. Effect of well width variation between 10-32 monolayers (ML) on E_{21} separation (Top Left). Effect of Al composition variation between 30-42% (Top Right). The effect of the E_{21} separation as it varies with the well width and Al composition compositely and the square of the well width (Bottom Left & Right respectively).

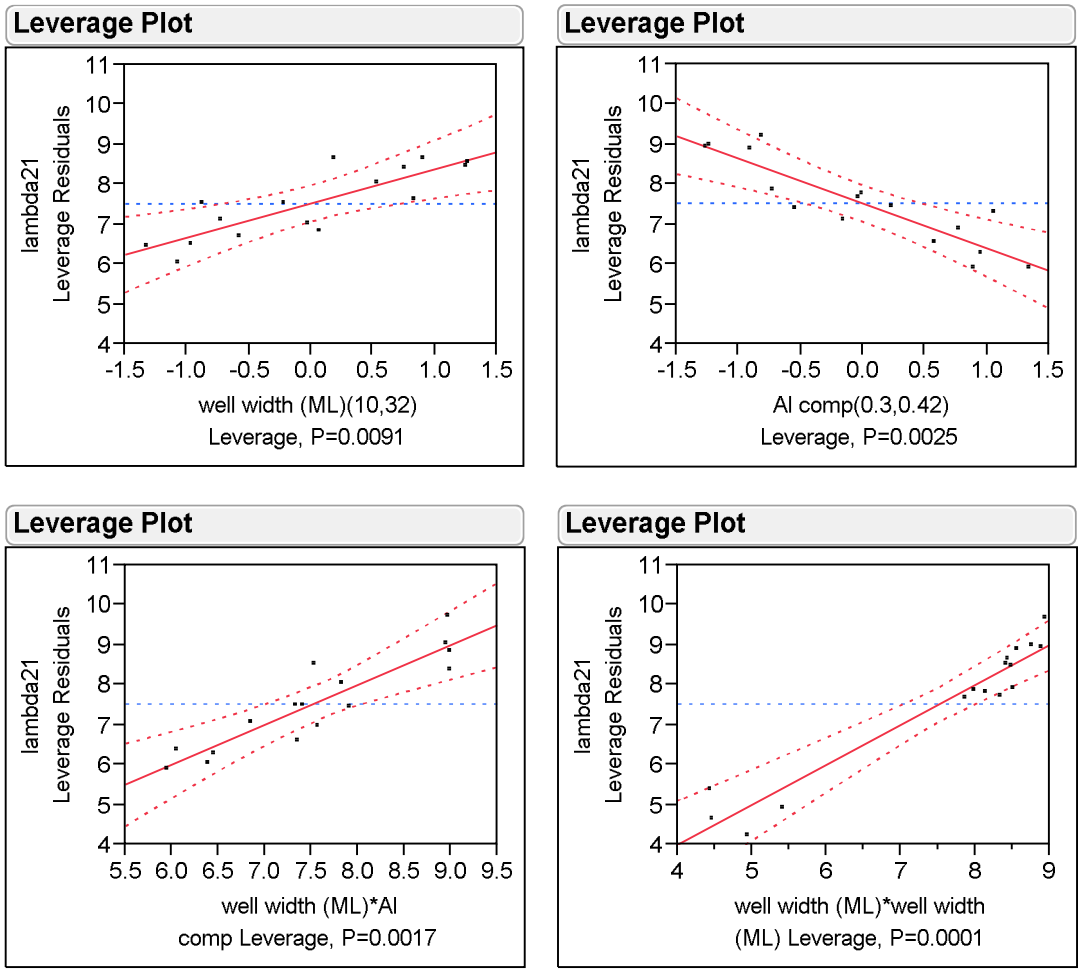

Figure 3.8 Leverage plots corresponding to the most significant interaction terms for optical absorption wavelength fit model. Effect of well width variation between 10-32 monolayers (ML) on absorption wavelength (Top Left). Effect of Al composition variation between 30-42% (Top Right). The effect of the absorption wavelength as it varies with the well width and Al composition compositely and the square of the well width (Bottom Left & Right respectively).

As seen from Figure 3.7 and 3.8, the well width and Al composition are the most significant design factors influencing the E_{21} separation and absorption wavelength. The leverage plots are marked by steep fit line slopes and confidence levels that contain at least 95% of the dataset. Furthermore, these regressors are both highly sensitive to the square of quantum well width. Implying that the rate of which both responses change with respect to variation in the well thickness is significantly great. Thus, for such a

structure, the well width is the most important parameter to ascertain a specific energy separation and absorption wavelength.

3.1.2 *nextnano*^{3} Quantum Well Design & Simulation

With these factors in mind, the first design consideration for this particular device is determining the materials that are applicable for use in device construction. The application in which the device will be employed has a significant role on the choice of materials that must be selected (direct versus indirect bandgap materials); where direct bandgap materials are more characteristic of optical devices as they allow more energy efficient radiative interband transitions. The choice of materials used is also more directly limited to the materials available in the growth facility. In despite, the *nextnano*^{3} package allows any group IV, III-V, or II-VI compositions to be considered and defined layer-by-layer. The proposed design for this dissertation considers a quantum well structure using GaAs, AlAs, and $Al_xG_{1-x}As$ compositions. These combinations of materials have been studied thoroughly and have proven effective for unstrained heterostructures based on the Kronig-Penney model of solids [37-39]. Once the growth materials have been selected, the device design can then be implemented.

The multiple quantum well structure proposed in this work is designed to achieve intersubband electroabsorption between 3-5 μm, a wavelength range not accessible in the case of traditional rectangular GaAs/$Al_xGa_{1-x}As$ quantum well devices [35]. Thus, a new double-barrier design is implemented to introduce greater carrier confinement and achieve the necessary energy level separation to attain intersubband

absorption in the 3-5 μm range [24,30]. Using this implementation, a multiple double-barrier quantum well structure is designed. Since a multiple quantum well structure is essentially a superposition of the single quantum well (provided that the barriers are thick enough to prevent tunneling into the subsequent wells; as is the case in this structure), the single well structure is simulated and analyzed with the *nextnano*[3] software package. Figure 3.9 below depicts the double-barrier quantum well structure simulated.

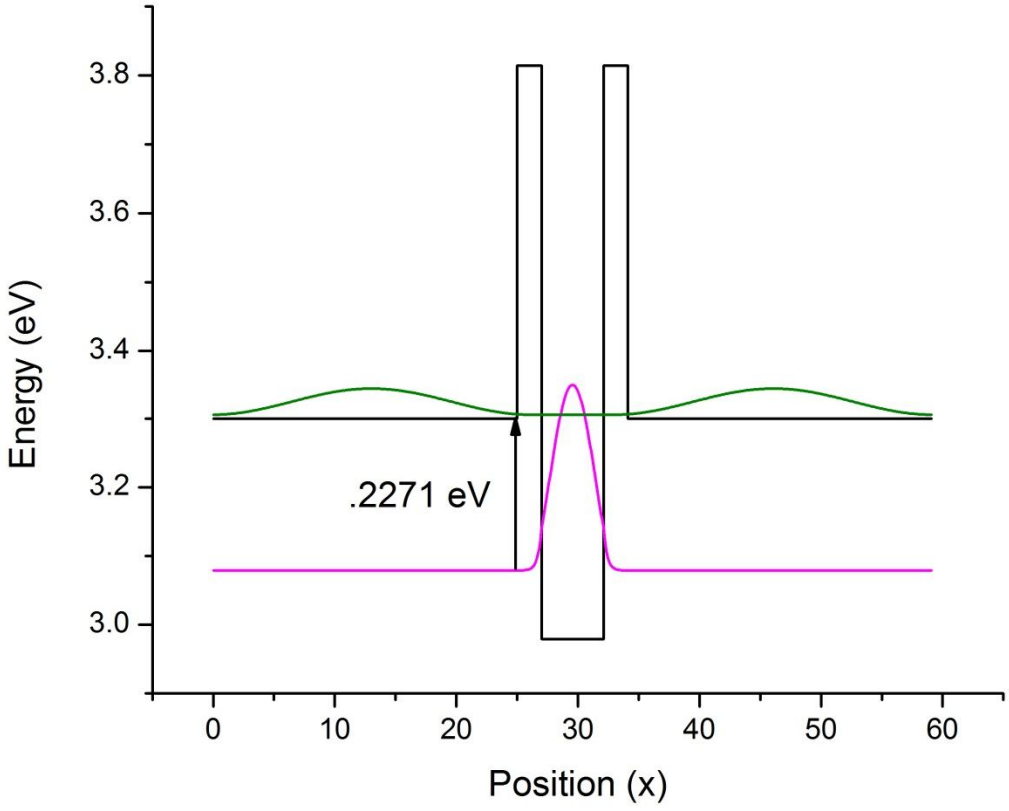

Figure 3.9 Conduction band profile of double barrier quantum well structure consisting of approximately 5 μm (18 ML) GaAs well, 2 μm (7 ML) AlAs tunnel barrier, and 25 μm $Al_{.30}Ga_{.70}As$ barrier.

From Figure 3.9 we can see the wavefunctions available in the quantum well structure and its associated eigenvalue. The eigenvalue represents the approximate discrete energy level in which the free electrons can reside while confined in the well. The separation between these two discrete levels can be adjusted by increasing/decreasing the GaAs well width. The accuracy for which these energy levels (and separation) can be determined is directly correlated with grid spacing or the step width parsing for each calculation in the layered structure. For sufficiently large well widths, the separation becomes negligibly small and nearly overlaps one another; conversely, the narrower the well, the larger the separation between intersubband energies [10]. It is also apparent from Figure 3.4 that the entire second wavefunction is not confined within the well as intended. This implies that there is a high possibility that the electrons may reside at the conduction band edge in the outer barrier (tunneling), therefore inhibiting absorptive behavior within the well. This issue can be addressed by further increasing the Aluminum composition in the outer barrier, raising the conduction band edge and confining the wavefunction within the quantum well (Figure 3.10). In doing so, results in a trade-off in intersubband energy separation. Therefore, further optimization is in order to ensure maximal absorption at the designed optical wavelength (discussed in Chapter 8).

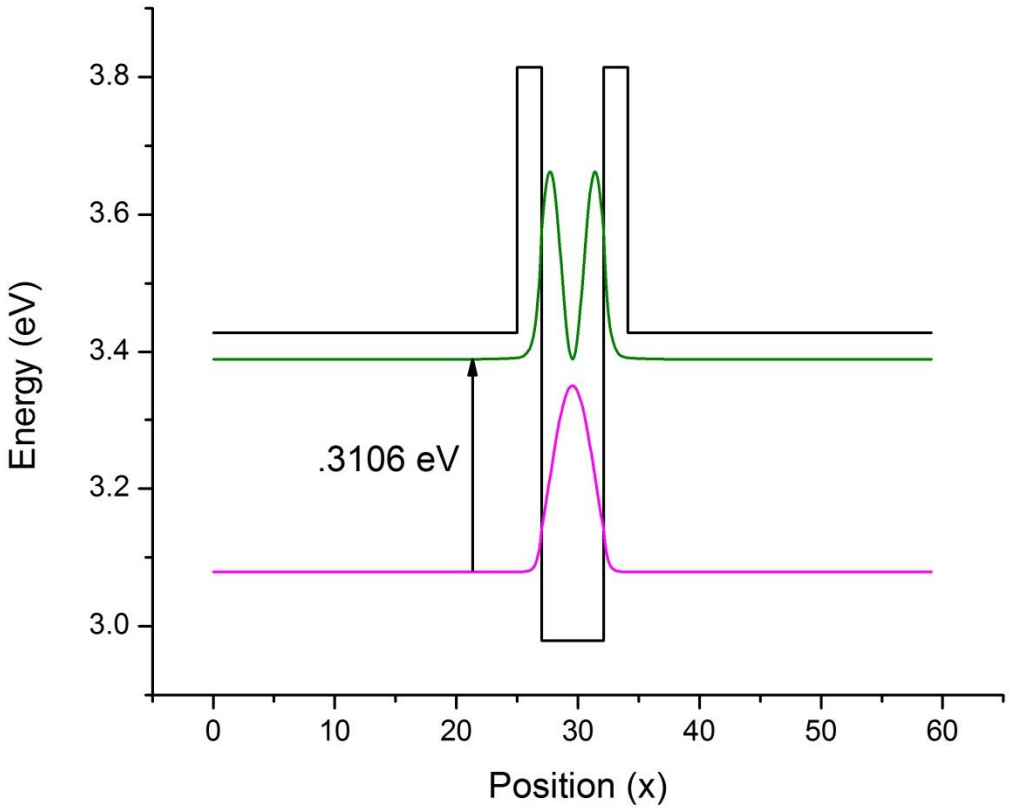

Figure 3.10 Conduction band profile of double barrier quantum well structure consisting of approximately 5 μm (18 ML) GaAs well, 2 μm (7 ML) AlAs tunnel barrier, and 25 μm $Al_{.42}Ga_{.58}As$ barrier.

The primary goal when designing a quantum well for intersubband electroabsorption is to determine the combination of tunable dimensions (i.e. well width, barrier width, barrier height, tunnel barrier width, etc.) that will yield a suitable energy level separation that discretely promote electron transitions at the specified wavelength. Once this is achieved, multiple identical wells can be added in conjunction to supplement the effect of the single well structure, therefore increasing the absorptive ability.

The *nextnano*[3] software is also provides the exact energy level available within the quantum well structure as well as provides a figure of merit corresponding to the likelihood that electron transitions will take place between the available states (considering a ground state populated with free carriers). The effective parameters that determine this likelihood of transitioning occurrence are the transition dipole moment and the oscillator strength. The transition dipole moment, or simply the transition moment, refers to the dipole moment observed between a final energy state containing a negatively charged excited electron and initial ground energy level containing a positively charge hole for which the electron will reside into. This phenomenon is induced by an electromagnetic wave (in this case, the incident wavelength radiation) with a frequency (ν) that corresponds to the separation of energy of final and initial state (or $\Delta E_{21} = h\nu$) [37,41]. The transition moment varies greatly with the carrier distribution and incident wave polarization and intensity. The transition dipole moment for a transition from *m* to *n* is given by

$$d_{nm} = \int \Psi_n^* \hat{d} \Psi_m d^3 r = \left\langle \Psi_n \mid \hat{d} \mid \Psi_m \right\rangle \text{ and } \hat{d} = e\left(\sum_i x_i, \sum_i y_i, \sum_i z_i \right) \qquad (3.7)$$

where the wavefunction at each state is dependent upon the position of every available electron. The result is a complex vector quantity whose squared magnitude gives a positive nonzero value equivalent of the strength of the interaction, which varies with carrier distribution [40].

The second figure of merit is the transition oscillator strength. This is an effective measure of strength or likelihood of an electron transition between a final and initial state. The oscillator strength can be described as

$$f_{mn} = \frac{2}{3}\frac{m_e}{\hbar^2}(E_2 - E_1)\sum_{m_2}\sum_{\alpha=x,y,z}\left|\langle 1m_1 \mid R_\alpha \mid 2m_2\rangle\right|^2 \tag{3.8}$$

Using *nextnano*[3], the well parameters are refined in order to maximize both the transition dipole moment and the oscillator strength, while ensuring that the target energy level separation remains relatively unchanged. In doing so implies the quantum well structure will exhibit absorptive capability at the specified wavelength and the transition will likely occur between to specific energy states. For the well structure considered, there exists only two intersubband states, thus and likely transitions must occur between the two available states. Therefore, the challenge lies in maximizing both the dipole moment and oscillator strength within the specified quantum well physical constraints. It has been determined that the quantum well width is the most influential factor effecting the intersubband wavefunctions. Increasing or decreasing the well width increases or decreases the wave function overlap (respectively), causing a slight spread of the wavefunction outside of the well with the decrease of the well width. This implies that there exist an optimum well size for every material system. The optimal well width for GaAs quantum wells is approximately 50 Å (5nm ~17-18 ML). From the previous statistical study, it is determined that a quantum well of approximately 5 nm (17-18 ML) in width yields an optical absorption wavelength at or near the specified wavelength. Therefore only quantum well modulators of 5 nm well width are

considered. After simulation the resultant transition moment and oscillator strength were achieved for each corresponding quantum well structure (Table 3.1).

Table 1 Quantum well design parameters.

E21 Separation (eV)	Oscillator Strength	λ21 (mm)	Transition Dipole Moment	Well Width (ML)	Tunnel Barrier Width (ML)	Aluminum Composition (%)
0.2271	0.000155	5.4601	0.19239	18	8	0.3
0.2271	0.000358	5.4601	0.29257	18	7	0.3
0.21846	0.000116	5.6761	0.1693	17	8	0.3
0.21847	0.000267	5.6758	0.25686	17	7	0.3
0.28032	0.000808	4.4235	0.39585	18	8	0.35
0.2271	0.000358	5.4601	0.59776	18	7	0.35
0.27169	0.000264	4.564	0.22915	17	8	0.35
0.27169	0.00059	4.564	0.34256	17	7	0.35
0.31084	0.98781	3.9892	13.1429	18	8	0.4
0.31039	0.97807	3.995	13.0871	18	7	0.4
0.3249	0.005108	3.8166	0.92182	17	8	0.4
0.32484	0.011856	3.8173	1.4045	17	7	0.4
0.31092	0.99008	3.9882	13.1561	18	8	0.42
0.31058	0.9826	3.9925	13.1134	18	7	0.42
0.33803	0.97508	3.6683	12.4864	17	8	0.42
0.3373	0.95305	3.6763	12.3576	17	7	0.42

Each structure in Table 3.1 represents the designs that correspond to satisfactory quantum characteristics. Table 3.2 highlights the parameters corresponding to an energy separation of .31-.38 eV, oscillator strength >90%, optical wavelength 3.8 μm ±5%, and positive integer >1 transition dipole moment. These structures most closely satisfies the design parameters. Inasmuch, it is apparent that for the specific structure an exact optical wavelength of 3.9 μm (most atmospherically transmissive wavelength in 3-5 μm window) is unattainable.

Table 3.2 Ideal quantum well parameters.

E21 Separation (eV)	Oscillator Strength	λ21 (mm)	Transition Dipole Moment	Well Width (ML)	Tunnel Barrier Width (ML)	Aluminum Composition (%)
0.31084	0.98781	3.9892	13.1429	18	8	0.4
0.31039	0.97807	3.995	13.0871	18	7	0.4
0.31092	0.99008	3.9882	13.1561	18	8	0.42
0.31058	0.9826	3.9925	13.1134	18	7	0.42
0.33803	0.97508	3.6683	12.4864	17	8	0.42
0.3373	0.95305	3.6763	12.3576	17	7	0.42

To achieve the shutter like operation characteristic to this type of device, it is important to achieve a sufficient absorption contrast at the design optical wavelength. This is achieved by applying an external bias across the entire length of the MQW cross-section. In doing so, induces a phenomenological bending at the band edge due to the Franz-Keldysh effect. The band bending results in both a lateral and vertical shift in the quantum well wavefunctions; thus decreasing the energy separation between the intersubband levels and shifting the second wavefunction into the barrier region. The shift of the wavefunction into the large barrier region is due to carrier drift associated with an applied external bias. The oscillator strength and transition dipole moment are reduced implying that the MQW region has become transparent to the optical wavelength.

This effect is a function of the applied external bias. As the bias is increased, the bending at the band edge becomes steeper exaggerating the effects of the wavefunction shifting. For a symmetric well, as is the case for the MQW of this device, reversing the polarity of the applied bias results in similar wavefunction shifts with the

slope of the bending reversed. The effects of external bias can also be simulated using the *nextnano*[3] software. Figures 3.11 and 3.12 show the results of 40 KV/cm bias and -40KV/cm bias on the double barrier quantum well structure respectively.

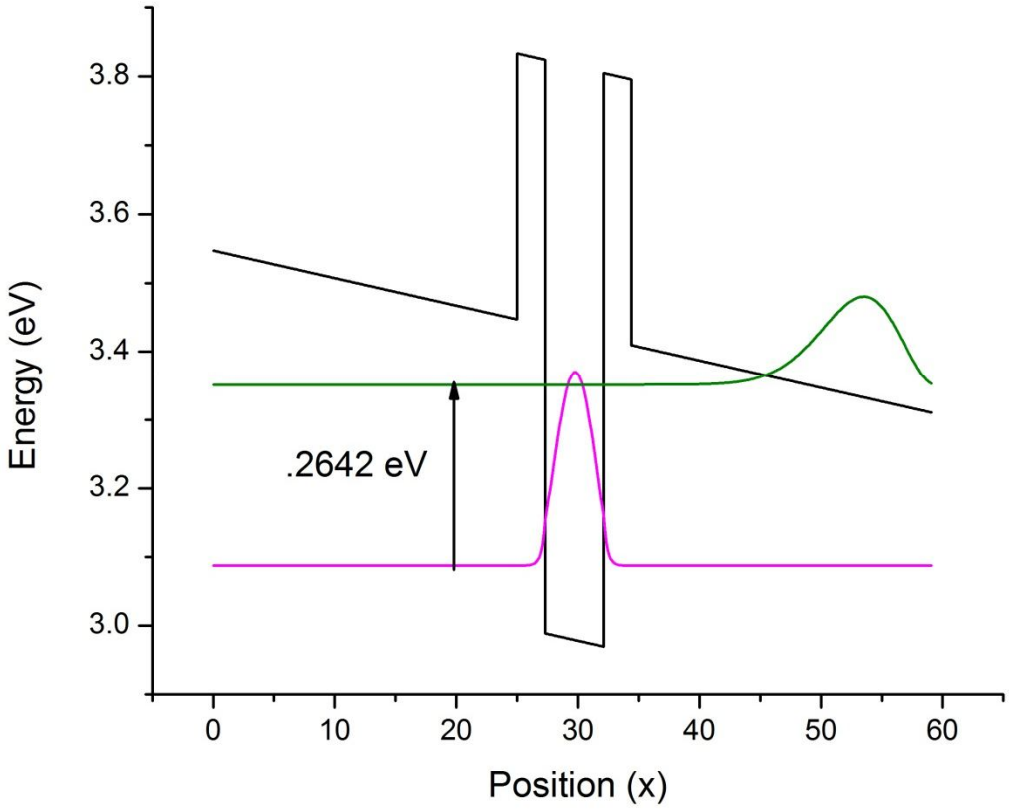

Figure 3.11 Double barrier quantum well structure with 40 kV/cm external bias (applied from right to left) exhibits decreasing band edge energy characteristic with position. The second wavefunction has shift right toward lower energy.

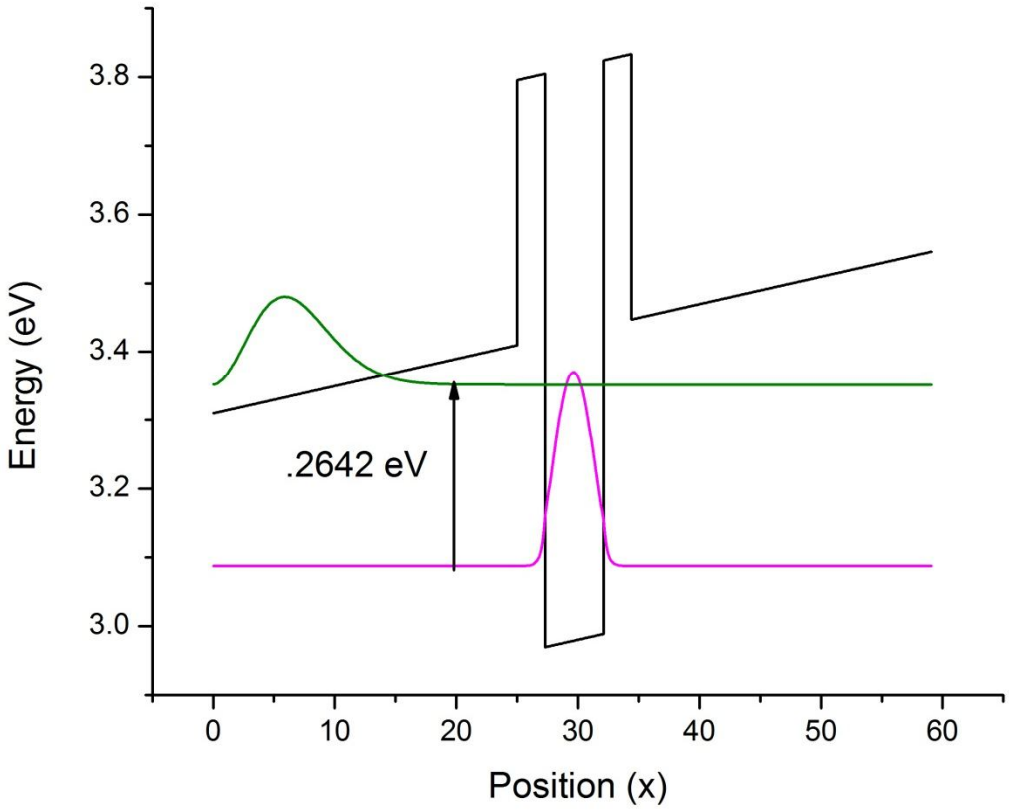

Figure 3.12 Double barrier quantum well structure with -40 kV/cm external bias (applied from left to right) exhibits increasing band edge energy characteristic with position. The second wavefunction has shift left toward lower energy.

Inasmuch, the band edge energy characteristic are plotted below in Figure 3.13; from which we can visualize how the intersubband spacing decreases with increasing applied bias. As the applied external bias is increased, both the oscillator strength and the transition dipole moment decrease exponentially implying that the desired optical transition becomes less likely with large external biases.

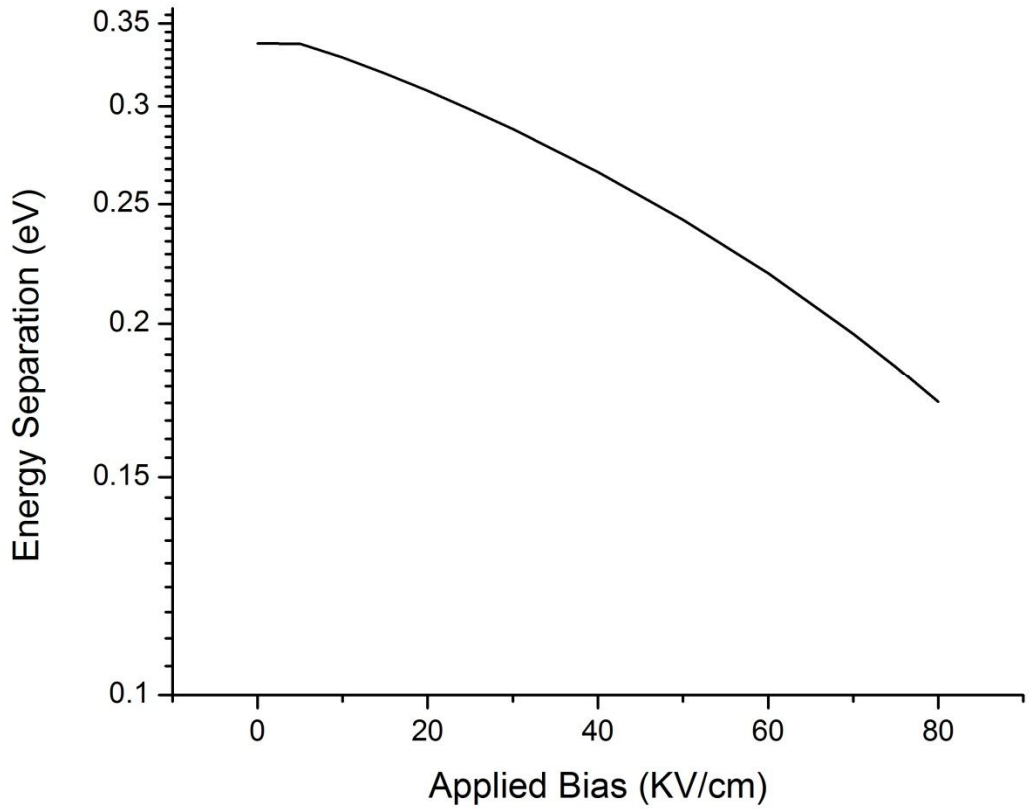

Figure 3.13 Effect of applying a perpendicular bias across a double-barrier quantum well structure. The E_{21} separation is compressed as the bias is increased (QCSE).

The associated transition dipole moment and oscillator strengths are also affected due to the application of a perpendicular external bias. As the applied electric field increases in magnitude, a greater electromagnetic force is induced upon the intersubband free carrier electrons opposing the polarity direction of the applied field. It is this force that is responsible for driving the E_2 wavefunction outside of the quantum well. This, in turn, causes a stepwise behavior in the transition dipole and oscillator strength. At zero bias, the E_2 wave function is confined within the quantum well and has substantial overlap with the E_1 wavefunction and thus implying a larger transition dipole moment oscillator strength value. Applying a small bias (<10 kV/cm), the E_2 wavefunction begins to

partially shift into the tunnel barrier with the majority of the wavefunction remaining within the confines of the quantum well with a partial E_1 overlap. Further increasing the applied bias beyond 10 kV/cm, instantaneously reduces both the oscillator strength and dipole moment, as the E_2 wavefunction is now completely outside of the quantum well. Excited E_1 electrons are less likely to reside within the confines of the quantum well and similarly, excited electrons are less likely to relax into E_1 states as implied by the plots of Figure 3.14 and 3.15.

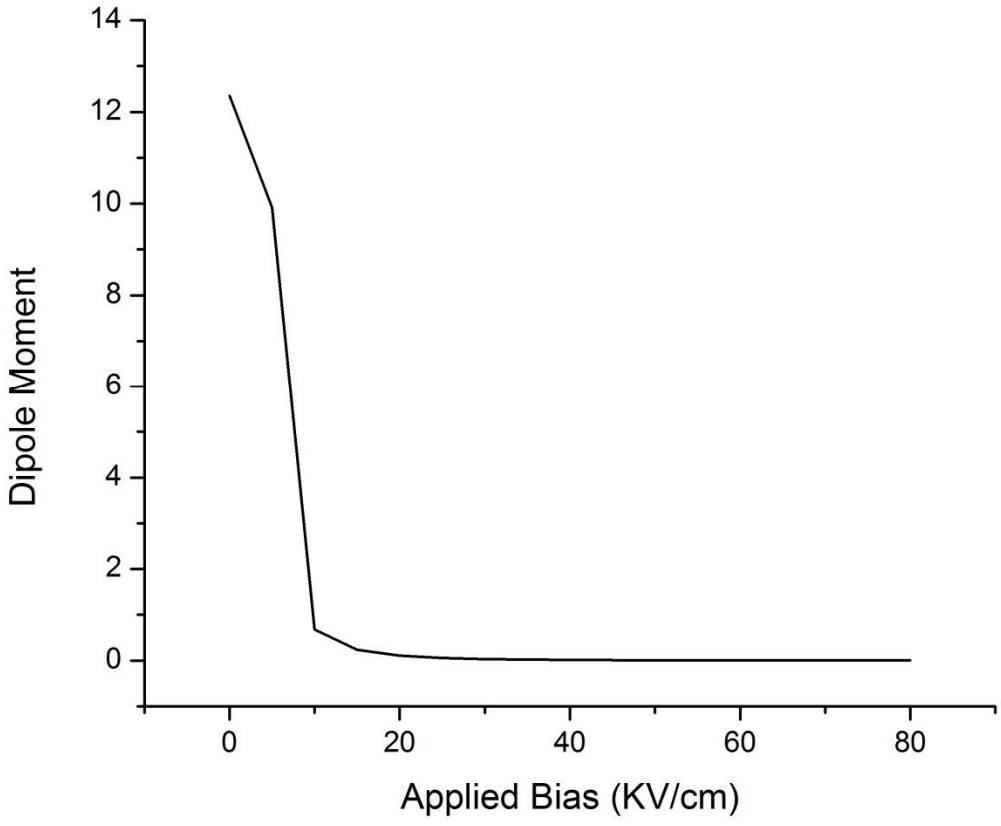

Figure 3.14 Stepwise behavior of transition dipole after applying a perpendicular bias across a double-barrier quantum well structure.

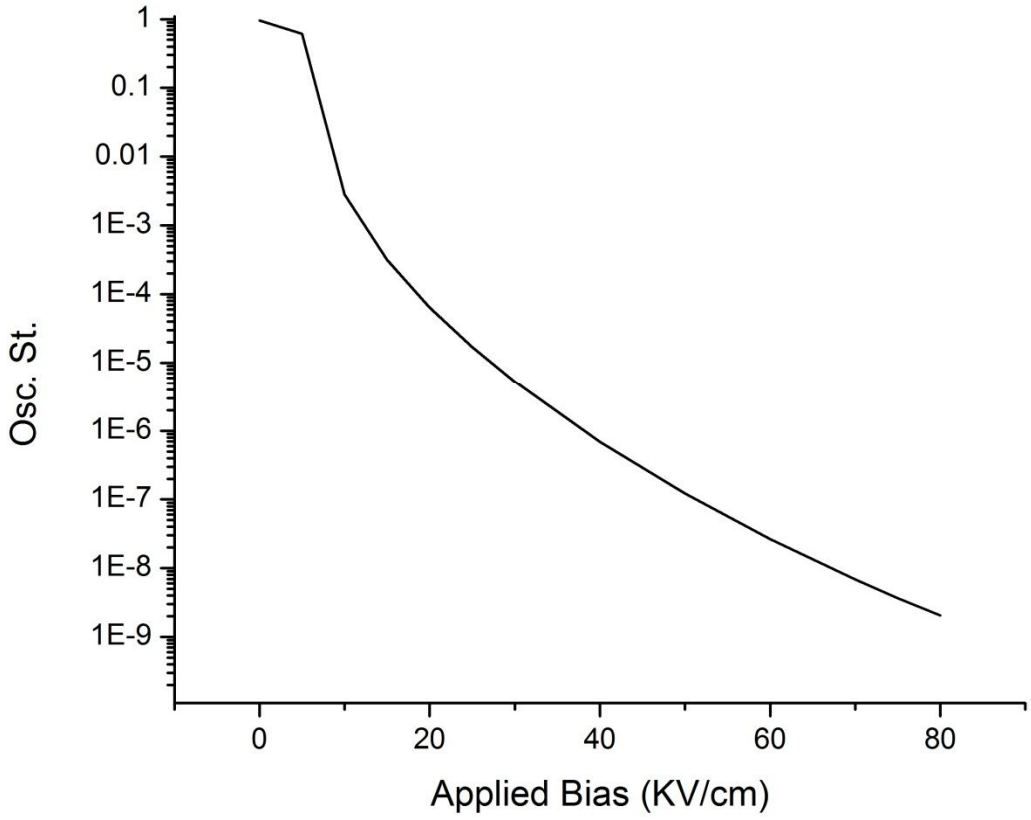

Figure 3.15 Stepwise behavior of oscillator strength after applying a perpendicular bias across a double-barrier quantum well structure.

From the plots above, an appropriate external biasing condition can be determined to invoke substantial shifts in the E_2 wavefunction and in turn absorbability of the specified wavelength. Determining a sufficient absorption contrast is entirely application specific and beyond the scope of this work.

3.2 Distributed Bragg Reflector Design & Simulation

The design process for a mid-infrared distributed Bragg reflector centered near 3.9 μm utilizing GaAs/AlAs materials is a very intricate endeavor, though the use of these material compositions are widely utilized and studied. The dispersion parameters for these materials (primarily that of AlAs) are not well defined in the mid-infrared spectrum and are often interpreted through simulation and experimental values. Dispersion for a given material can be written as a function of the incident energy upon the material and is essentially a measure of how will the electromagnetic radiation travels within a medium as opposed to in a pure vacuum. This relationship can be described by the Sellmeier dispersion equation given by

$$n^2(E) - 1 = \frac{E_0 E_d}{E_0^2 - E^2} \tag{3.9}$$

where n is the refractive index of the material, E_0 is the single dipole transition energy, E_d is the dispersion energy, and E is the incident energy. Using this dispersion relationship, the mid-infrared parameters can be approximated from known dispersion behaviors in the near-infrared spectrum. By determining the appropriate material layer thicknesses from NIR parameters, the MIR dispersion parameters can be approximated [42,43]. In doing so, the following MIR dispersion parameters are resolved (Table 3.2)

Table 3.3 Mid-infrared extracted parameters from DBR reflectivity [42].

Material	E_0 **(eV)**	E_d **(eV)**
GaAs	3.10 ± 0.05	29.05 ± 0.5
AlAs	4.90 ± 0.05	34.15 ± 0.5

With the aforementioned parameters, the refractive index of each material is experimentally determined in the mid-infrared spectrum as a function of the incident wavelength. Equation 3.10 relates the incident wavelength and energy.

$$E(\lambda) = \frac{1.2398}{\lambda_{inc}} \tag{3.10}$$

Combining equations 3.9 and 3.10 along with the parameters of Table 3.3, the experimental refractive indices for GaAs and AlAs can be described as a function of the incident wavelength. Figure 3.14 shows the variance in refractive index for binary GaAs and AlAs compounds when irradiated with an incident wavelength between 2-6 μm. The experimental refractive index values resemble a very linear behavior; based on this approximation of the desired spectral range, the refractive indices can be taken as approximately constant. Thus, yielding a refractive index value of approximately 3.2 for GaAs and 2.8 for AlAs (Figure 3.16).

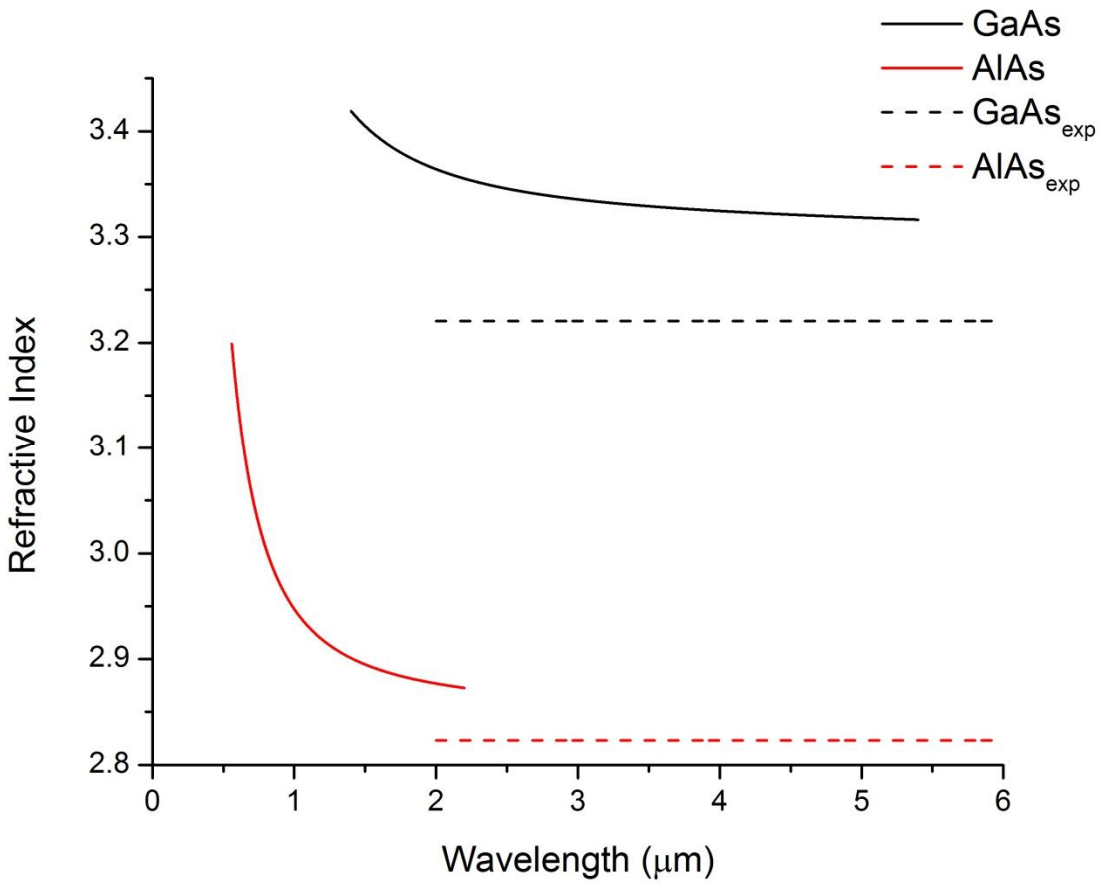

Figure 3.16 Plot of refractive index vs wavelength for binary compounds GaAs and AlAs.

An important factor when designing a distributed Bragg reflector is the refractive index contrast ratio between the chosen material defined as n_H/n_L where n_H and n_L is the high and low refractive index values respectively. Maximizing this ratio ensures maximal reflectivity for a given number of repeated Bragg layer pairs (this diffraction phenomenon is described in Chapter 2). The following plot (Figure 3.17) shows the relationship between the reflection coefficient at the interface between low and high refractive index material changes with contrast ratio.

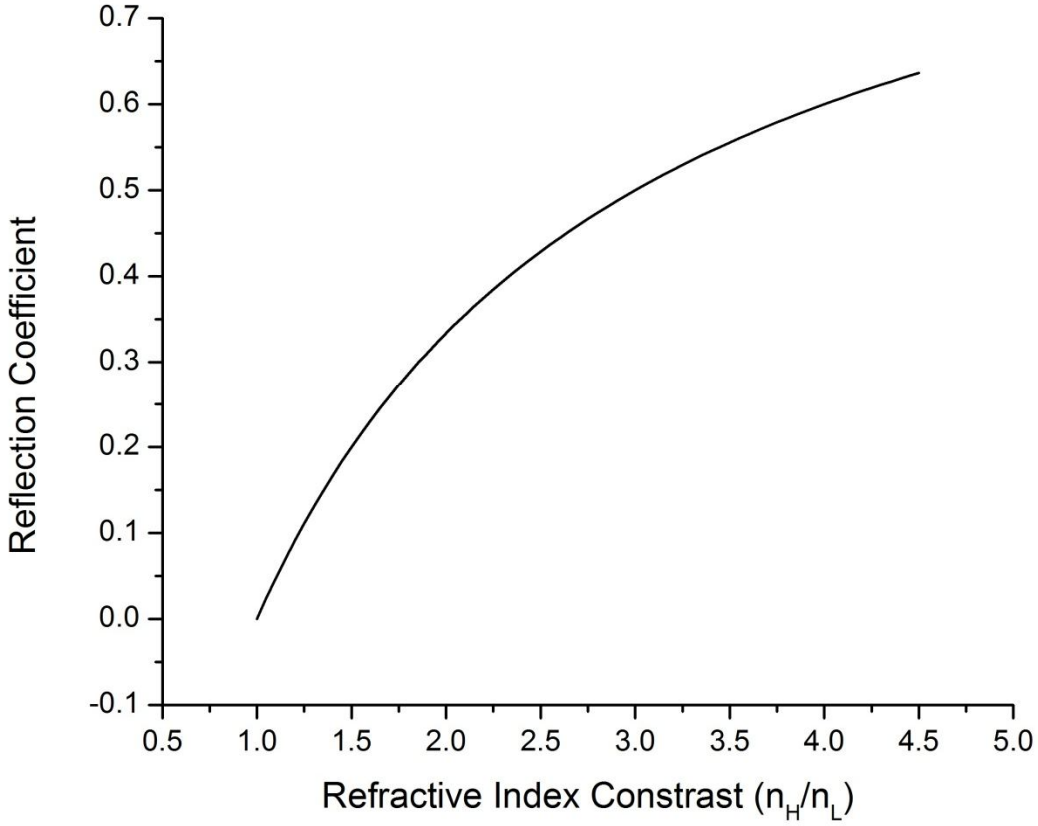

Figure 3.17 Reflection coefficient vs refractive index contrast ratio for a single period of high and low refractive index material.

The refractive index contrast ratio between GaAs (n_H) and AlAs (n_L) is not very high (ranging approximately from 1.3 – 1.36), thus implying very low reflection coefficients at each interface. For this very reason, despite successful implementations [39,40,44-46], GaAs/AlAs Bragg reflectors are not typically attractive in many MIR applications because of the necessity to successfully deposit many layers to achieve a high reflectivity spectrum. However, GaAs/AlAs structures offer a very significant advantage over many other compound materials, which is the ability to grow very large high quality layers due to the near identical lattice constants (~5.65 Å for GaAs and ~5.64 Å); thus granting

great flexibility of application. With all aforementioned parameters considered, the high reflectivity spectrum for the specified DBR can be evaluated.

3.2.1 Transfer Matrix Method approach to Reflectivity

Reflection in a distributed Bragg reflector occurs as an additive of multiple reflections at the high and low refractive index interfaces. In order to accurately represent the reflective behavior of a stratified medium a method that can recursively account for the effects of reflection at each interface is necessary. The transfer matrix method (TMM) is a common approach in optics to analyze the propagation of a particular electromagnetic wave as it travels through a multilayered structure such as Bragg reflectors. This method is very effective since transmission and reflection within each layer can be described with coupled mode theory (CMT) and simple matrix operations [47,48]. A custom implementation was constructed in MATLAB over the course of several months in order to achieve this simulation.

The TMM method is a method of analyzing the propagation of an electromagnetic wave through a layered medium most commonly used for simulating DBR reflectivity. This method is implemented with the extrapolated refractive index constants of binary GaAs and AlAs from the single oscillator model (Palmer et. al). Equation 3.11 describes the matrix method implemented in this dissertation.

$$T_p = \left(\frac{1}{T_a T_b}\right)\begin{vmatrix} \left(e_a^{-1}e_b^{-1}\right)-\left(r^2 e_z^{-1}e_b\right) & r*\left(e_z^{-1}e_b\right)-\left(e_a^{-1}e_b^{-1}\right) \\ r*\left(e_a e_b^{-1}\right)-\left(e_a e_b\right) & \left(e_a e_b\right)-\left(r^2 e_a e_b^{-1}\right) \end{vmatrix} \tag{3.11}$$

Where T_p is the transmission at the specified wavelength, T_a and T_b is the transmission coefficient at the specified wavelength in the high and low refractive index materials respectively, and r is the reflection coefficient of the high refractive material (GaAs). The values of e_a, and e_b are listed below respectively.

$$e_a = e^{i\beta_h t_h}$$
$$e_b = e^{i\beta_l t_l}$$

With $\beta_{h,l}$ and $t_{h,l}$ are the propagation constant and the quarter-wave layer thickness of the high and low refractive index medium respectively. Applying equation 3.11 for N iterations (number of paired layers) yields the transmission matrix through the stratified medium. The product of the transmission matrix (T_p) and the identity matrix yields the respective reflectivity matrix (R_s) and the square of the reflectivity matrix produces the reflectance. The reflectance is used to estimate the expected spectral response of 3-5 μm radiation on the DBR region of the device.

REFERENCES

[37] Donald A. McQuarrie, “The Kronig-Penney Model: A Single Lecture Illustrating the Band Structure of Solids,” vol. 1 no. 1. The Chemical Educator. ISSN 1430-4171 (1996).

[38] IUPAC Compendium of Chemical Terminology, 2nd Edition (1997).

[39] B. G. Kim, E. Garmire, S. Hummel, and P. D. Dapkus, “Nonlinear Bragg reflector based on saturable absorption,” *Appl. Phys. Lett.* 54 (12), 20 March 1989.

[40] S. Hastings, M. J. A. de Dood, H. Kim, W. Marshall, H. Eisenberg, and D. Bouwmeester, “Ultrafast optical response of a high reflectivity GaAs/AlAs Bragg mirror,” *Appl. Phys. Lett.* 86 (3) 031109. (2005).

[41] Neamen, D. A. *Semiconductor Physics and Devices: Basic Principle*, 3rd ed.2003.

[42] Handbook of Optics, sponsored by the Optical Society of America. 2nd ed. vol. 2, 1994

[43] Palmer, C.; Stravrinou, P. N.; Whitehead, M.; Phillips, C. C.;, “Mid-infrared (λ ~ 2-6 μm) measurements of the refractive indices of GaAs and AlAs,” *Semiconductor Science and Technology, 2002*, no.,pp.1189-1192, 16 Oct. 2002.

[44] S. H. Wemple and M. DiDomenico Jr., “Behavior of the Electronic Dielectric Constant and Ionic Materials,” *Phys. Rev. B 3,* pp.1338-1351, 1971.

[45] J. Trull, C. Cojocaru, J. Massaneda, R. Vilaseca, and J. Martorell, "Determination of Refractive Indices of Quarter-Wavelength Bragg Reflectors by Reflectance Measurements in Wavelength and Angular Domains," *Appl. Opt.* 41, 5172-5178 (2002).

[46] J. C. Bean, L. J. Peticolas, R. Hull, D. L. Windt, R. Kuchibhotla, and J. C. Campbell, “Design and fabrication of asymmetric strained layer mirrors for optoelectronic applications,” *Appl. Phys. Lett.* 63, 444 (1993).

[47] T. Makino, “Transfer Matrix Method With Applications To Distributed Feedback Optical Devices,” *PIER* 10, 271-319, 1995.

[48] Z. Y. Li, B. Y. Gu, and G. Z. Yang, “Slowly varying amplitude approximation appraised by transfer-matrix approach,” *Phys. Rev.* B vol. 60. (15). 15 October 1999.

CHAPTER 4

EXPERIMENTAL IMPLEMENTATION

4.1 Previous Works

Chapter 3 resolved the modulating reflector device into two semiconductor subdevices; the multiple quantum well modulator and the distributed Bragg reflector. The overall performance and versatility of the composite device is essentially dependent on the specific characteristics of each subdevice. The efficacy of modulation is attributed to the quantum well's ability to absorb photon energy and generate mobile electrons to contribute to the photocurrent when driven by an external bias. Conversely, when there is no external force acting, the wells must be fully transmissive to the incident energy. The speed at which these interactions can occurs directly contributes to modulation speeds. These factors are related to the physical attributes of the quantum well (i.e. well width, height, materials etc.) and can be tailored to fit the specifications of each individual application. The ability to relay the modulated information back to the correct destination for interpretation with accurate signal integrity is the sole purpose of the reflective optic. Therefore, the reflective ability and operating range of the DBR its primary governing figures of merit. For RM devices designed specifically for FSO applications in the mid-infrared spectrum, like devices in near-infrared (NIR) regime, high-speed modulation and sufficient reflectivity at atmosphere transmissive wavelengths are imperative to establish communication.

Considering the RM devices as proposed by Gilbreath (et. al) composed of InGaAs quantum wells and AlGaAs barriers, operation parameters (as specified by the NRL) require functionality at optical communication wavelengths (850nm and 980nm). Thus, the selection of applicable growth materials is narrowed by the application itself (therefore, the growth of such novel semiconductor devices is restricted to certain well-studied compounds). Seventy-five InGaAs/AlGaAs (well/barrier) periods were grown on an n-doped GaAs wafer substrate with the MBE method. The resulting structure is capable of modulation speeds of 4-10 Mbps [9-14]. These particular RM device implementations require an unusually large aperture and mesa size to implement in the UAV communication system for which it is designed [14]. Keeping in mind that the device performance scales down with the physical size. The larger the device, the slower the achievable modulation speed will be as sheet resistivity and stray capacitances plays a larger role in the device's operation. Therefore a compromise between device size and speed must be made strictly dependent upon the application of the device. Since this device is design for FSO communication, more specifically, communication with a UAV unit, the size of the RM is slightly more important than the speed at which it operates as to establish and maintain a stable communication link with a dynamic unit moving at variable speeds. Furthermore, larger devices tend to emphasize the physical flaws and deformities of the growth procedure whether in the QWM region or the reflective optic, which makes uniformity in the growth procedure of the utmost vitality.

As specified in the previous sections, the design of near-infrared RM directly dependent on the application(s) in which the device is required. The requirements and

additional specifications determine which materials are appropriate for growth and what is an adequate device size. Arsenide group quantum well modulators have been implemented in various fashions and heavily studied for optical modulators and electroabsorbers [20,21,49]. The versatility of these materials for optical applications makes them desirable and sufficient for the majority of applications.

4.2 Mid-Infrared RM Implementation

Like the design of a reflective modulator device for near-infrared communication, the design of reflective modulators for mid-infrared communication is also application specific. In this case, the FSO methodology of optical communication is the primary influence on the construction of this device. Therefore, the device is strategically designed to operate within mid-infrared wavelengths that are the most readily permissible without major atmospheric absorption (3.5-4.1 μm) [1]. Once the operation wavelength is selected, each subdevice within the RM can be customized for mid-infrared operation separately; with the primary objective in mind.

4.2.1 Quantum Well Modulator Implementation

This particular reflective modulator implementation is intended to achieve optical shutter and reflection operation at approximately 3.9 μm using primarily the GaAs/AlAs group compositions. The principal reason in this approach is due to the high sustainability of GaAs device structures. GaAs/AlAs devices are heavily regarded in optoelectronic applications for their high lattice constant matching and optical properties. Inasmuch, developing a structure with very high lattice constant matching

helps circumvent the effects of strain in the device and greatly simplifies the relations of quantum well parameters. Naturally, such optical wavelengths are not achievable with strictly GaAs/AlAs binary material systems, thus the double-barrier quantum well structure is adopted to enhance free carrier confinement with in the quantum well [35,36]. With increased confinement, energy separations on the order of the design optical wavelength are achievable. The adjustable well parameters are: the quantum well width, tunnel barrier width, and the external barrier height. Adjusting each has an effect on the quantum well (as shown by the simulations in Chapter 3). The most optimal structure is chosen to closely emulate design specifications.

4.2.2 Distributed Bragg Reflector Implementation

The subsequent reflective optic of in this implementation is a quarter-wave distributed Bragg reflector composed of alternating pairs of GaAs and AlAs binary compounds. Though these compounds are not typically known for their high refractive index contrast, as is appealing for such a device, they compensate with their high lattice matching and ability to grow very thick adjacent layers with minimal strain. Reflection at 3.9 μm is achieved by growing pairs of binary GaAs and AlAs approximately 299.4 nm and 342.61 nm thick respectively. The number of repeated pairs determines the peak reflectivity achievable with the specified materials. Peak reflectivity is often a parameter determined by the application in mind. Though a high-reflectivity mirror is very attractive for FSO applications, it is not necessary to demonstrate device functionality. Therefore, the number of repeated pairs is arbitrarily chosen to be 12 periods

corresponding to roughly 87% relative reflectivity. Reducing the number of repeated layers sacrifices only the maximum achievable reflectivity.

4.2.3 Design Difficulties and Improvements

The implementation of such a device presents many small obstacles primarily in the fabrication process that must be overcome to achieve ideal operation and functionality of the device. In particular, it is essential to achieve layer uniformity in each subsequent quarter-wave layer stack in the distributed Bragg reflector. Fluctuations in layer thicknesses will results in slightly higher reflectivity peaks at the constructive interference fringes. This is described by the relationship between quarter-wave layer thickness and the incident radiation. Inasmuch, when constructing DBR, it is imperative that deposition technique is used that provides high precision and repeatability of uniform epitaxial layers. For this very reason, MBE is a very attractive method of device construction.

A minor obstacle arises when considering growths with the EPI Model 930. Due to fluctuations in beam equivalent pressure (BEP) that arise as the material volume depletes during the growth process. This is due to the cone-shaped crucible of the effusion cells.

4.3 Optical Characterization Setups

The following section describes the characterization methods used to evaluate the device optical properties. Photoluminescence (PL) is the primary method of characterization used to analyze the quantum well modular region of the device. PL gives information on surface/interface quality of the quantum well as well as the doping level of each well. MID-IR absorption spectroscopy is another technique used to evaluate the quantum well region's ability to absorb optical energy and provides a spectrum of peaks at the absorption wavelengths. The final characterization method is specular reflectance. This characterization technique is used to measure the amount of reflected irradiance of the DBR region providing a spectrum revealing the high reflectivity zones of the device.

4.3.1 Photoluminescence

The experimental photoluminescence setup used to optically characterize this device consists of: a 680 nm laser for photoexcitation and an array of spectrophotometers ranging from 600 – 16000 nm. The 680 nm laser is used primarily for exciting transitions beyond the band edge of semiconductor materials (corresponding to energies of 1.8 eV and below). This proves useful in examining interband interactions of semiconductor materials of applicable energies. The incident energy from the 680 nm DFB laser promotes valence electrons into the conduction band leaving behind a hole (an absence of an electron). As these electron-hole pairs recombine, they emit a photon of energy equivalent to that of the separation between

the excited and the ground energy state. Electrons-hole pairs recombining at the band edge (conduction band minimum and valence band maximum) luminesce at the material bandgap energy. The majority of electrons recombine at this energy resulting in an absolute maximum at the corresponding energy. Other likely transitions result in local maxima in the PL spectra.

In specific, GaAs has three observable maxima in its PL spectra. The absolute maximum occurs at approximately 870 nm which corresponds to the bandgap energy for GaAs at 300 K (1.425 eV). The two local maxima are that are prevalent on the high energy side of the PL spectra correspond to n=1 heavy hole and light hole transitions with each increasing in energy respectively.

4.3.2 MID-IR Absorption Spectroscopy

The mid-infrared absorption spectroscopy setup of this dissertation consists of a mid-infrared globar heatgun source (with subsequent optics) and grated monochromator. The globar source emits radiation ranging from approximately 1 to 10 μm and irradiates orthogonally to the sample surface. The incident photons permeate through the sample and are absorbed in each adjacent quantum well. The absorption spectrum is then determined in reference to a blank substrate sample. This technique proves useful in observing both high absorption and transmission moments in a sample optical spectrum.

A blank substrate serves as the reference spectra in this absorption setup. The substrate is mounted onto a sample stage perpendicular to the incident radiation of the

IR-18 globar source. The source irradiates the sample with the transmitted radiation externally filtered by an optical lens permitting only 3-5 radiation. An optical chopper is set at approximately 1500 Hz in conjunction with a lock-in amplifier which hones in on and amplifies the optical signal of corresponding frequency detected by the monochromator detector. Once the reference signal is recorded, the procedure is repeated for the test sample and the absorption/transmission spectra is extrapolated using a custom software package.

4.3.3 Specular Reflectance

Specular reflectance spectroscopy is the primary method used to obtain reflectance spectra from the distributed Bragg reflector samples considered in this dissertation. This experimental setup consists of a mid-infrared globar heatgun mounted at a 45 degree incident angle from the sample surface, resulting in a reflect wave of the equal and opposite angle into a spectrophotometer via a graded index fiber. The relative reflectivity is measured with respect to a gold mirror.

REFERENCES

[49] G. D. Boyd, D. A. B. Miller, D. S. Chemla, S. L. McCall, A. C. Gossard, and J. H. English, “Multiple quantum well reflection modulator,” *AT&T Bell Laboratories*. 1987.

[50] D. S. Katzer, W. S. Rabinovich, K. Ikossi-Anastasiou, and G. C. Gilbreath, “Optimization of buffer layers for InGaAs/AlGaAs PIN optical modulators grown on GaAs substrates by molecular beam epitaxy,” *J. Vac. Sci. Technol.* B 18(3), May/Jun 2000.

CHAPTER 5

DEVICE FABRICATION

This chapter describes the complex procedure and trade-offs taken into account in the production of each composite device in the mid-infrared reflective modulator using molecular beam epitaxy. This epitaxial technique is ideal for constructing abrupt junction heterostructures and is the primary approach considered in this work. The procedure in the following section is specific for the device considered in this dissertation as grown by EPI Model 930 Molecular Beam Epitaxy available at the University of Missouri-Columbia.

5.1 Solid Source MBE Growth Procedure

Solid source molecular beam epitaxy is a premier epitaxial growth method for high precision, high purity semiconductor devices (capable of impurity levels below ten parts per billion and atomic layer precision). The following growth procedure is as it pertains to the EPI Model 930 Molecular Beam Epitaxy machine available in the Compound Semiconductor Research Laboratory at the University of Missouri-Columbia.

Before the commencement of the growth process, there are a few system imperatives that must be considered. In order to maintain an ultra-high vacuum environment within the primary chamber during growth procedures, a substantial amount of external system cooling is required. A constant flow of liquid Nitrogen (LN_2) is supplied to the growth chamber along the cryoshroud and substrate heater. LN_2 flow is

initiated prior to the commencement of each growth process. Chilled water is used to cool the surrounding of each Knudsen effusion cell (continuously cooled even when system sits idle) as the cells are heated to the appropriate temperatures. Cooling each cell minimizes the contribution of released gas from each adjacent cell (outgassing) as well as maintains the durability of the cell itself.

In order to determine the possible theoretical growth rates for epitaxial growth the beam equivalent pressure is recorded at a series of different temperatures using an ion gauge reading from positioned at the substrate location. These readings are in turned used to determine the activation energy associated with each material. The theoretical flux is then determined by the following equation (5.1) relating the cell temperature and the activation energy.

$$f(T, E_a) = Ce^{\frac{E_a T}{k_B}} \tag{5.1}$$

where E_a is the activation energy, T is the cell temperature in Kelvin, k_B is the Boltzmann constant, and C is a proportionality constant. From this equation theoretical flux ratio is determined at each cell temperature. The growth rate is then determined from RHEED oscillations at each associated cell temperature associated with the frequency of the chemisorption process on the substrate surface (with varying diffraction patterns as described in Chapter 2). The average value is taken from a series of three to five repeated measurement and taken as the experimental growth rate. The growth rate is essential in determining each epitaxial layer thickness, cumulative growth time, and

material deposition rate. Using this information, a structural recipe is constructed to automate the MBE system to yield the specified device through a series of timed shutter manipulations, cell temperature adjustments, and substrate heating.

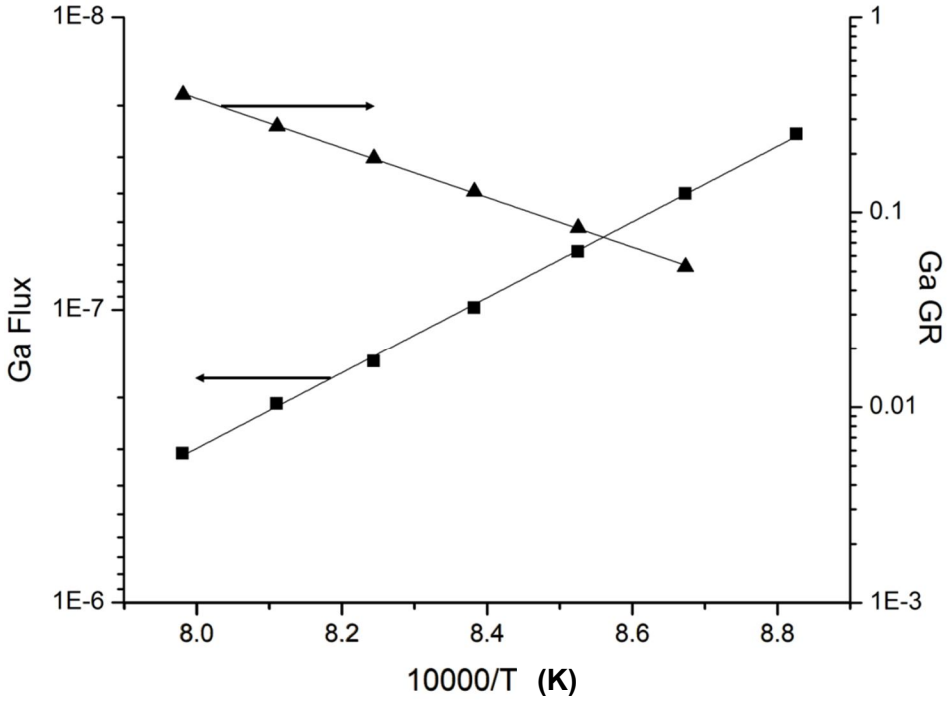

Figure 5.1 Theoretical flux (Torr) and experimental growth rate (μm/hr) approximated from BEP and RHEED oscillation of the 30 cc. Gallium (1) cell.

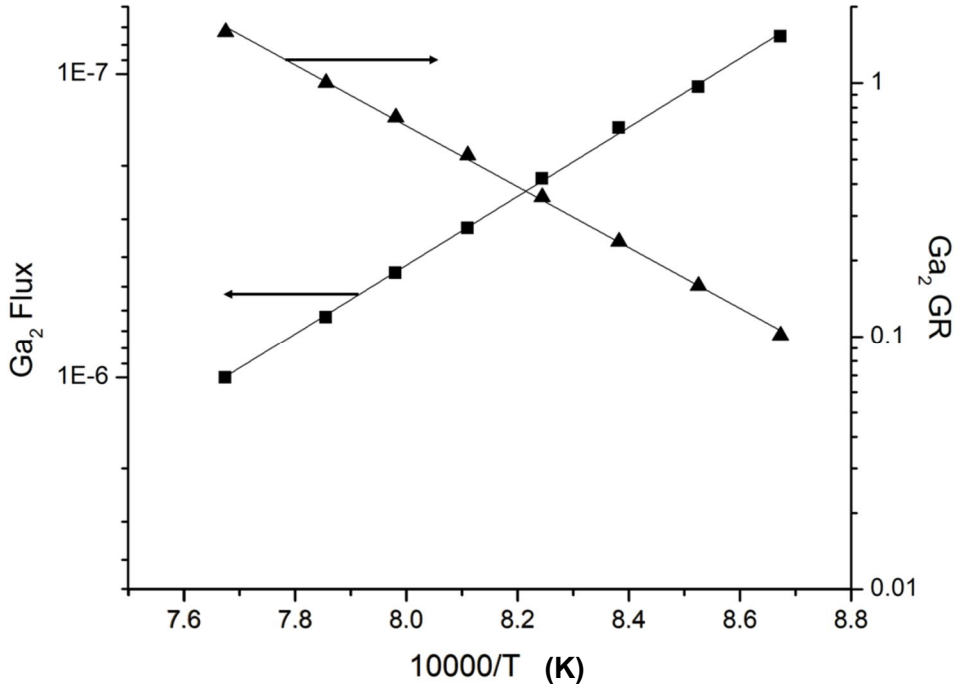

Figure 5.2 Theoretical flux (Torr) and experimental growth rate (μm/hr) approximated from BEP and RHEED oscillation of the 85 cc. Gallium (2) cell.

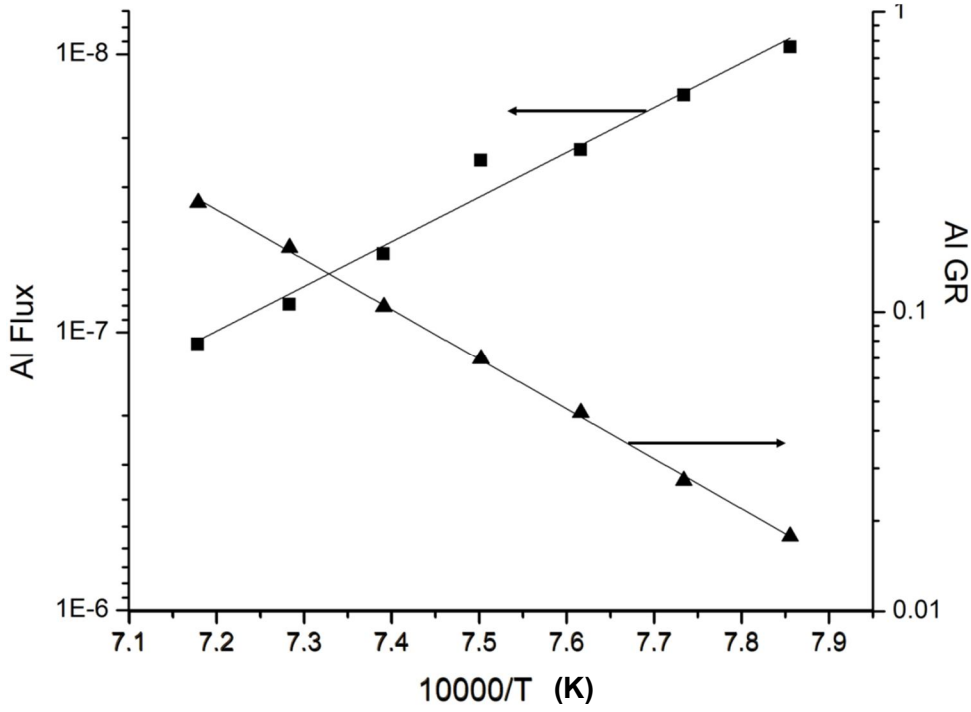

Figure 5.3 Theoretical flux (Torr) and experimental growth rate (μm/hr) approximated from BEP and RHEED oscillation of the 30 cc. Aluminum cell.

The growth process used to construct the devices considered in this dissertation begins with a two inch undoped GaAs semi-insulative (SI) wafer with (100) orientation transparent to the operation wavelength. This wafer orientation has been thoroughly studied for GaAs structures and suffices for device construction. The wafer is then cleaved into a single quarter fragment and mounted on to a Molybdenum mounting block by the use of Indium that adheres the sample to the block through surface tension. Once mounted onto the sample block, it is ready to be placed on the sample rack within the introduction chamber. In order to open the introduction chamber, the chamber pressure must be increased from approximately 10^{-6} – 10^{-7} Torr to equivalent atmosphere pressure (1 ATM). The blank wafer samples are pressure cleaned with Nitrogen blow gun and placed in the introduction chamber of MBE. Once the introduction chamber is pumped down to an appropriate pressure, via the use of both mechanical and ion pumps, (~10^{-6} – 10^{-7} Torr), the sample block is transferred into the growth chamber (Figure 5.4). It is of the utmost importance that the introduction chamber remain in a high vacuum state to ensure that substrate and successive chambers are purged of unwanted material. The pressure in the introduction chamber affects integrity of device construction and must be under high vacuum (low-pressure) before any successive barriers between the chambers are opened to position the sample. The next chamber serves as a buffer or intermediate later for storing and transitioning samples. The pressure in the transition chamber must also remain under high vacuum to avoid jeopardizing the ultra-high vacuum of the growth chamber during sample transfer since it is the chamber directly connected to the main growth chamber

in ultra-high vacuum. The pressure in the growth chamber will affect the mean-free path of traveling molecules toward the substrate during the growth process and thus is maintained with cooperative ion and cryo pumps.

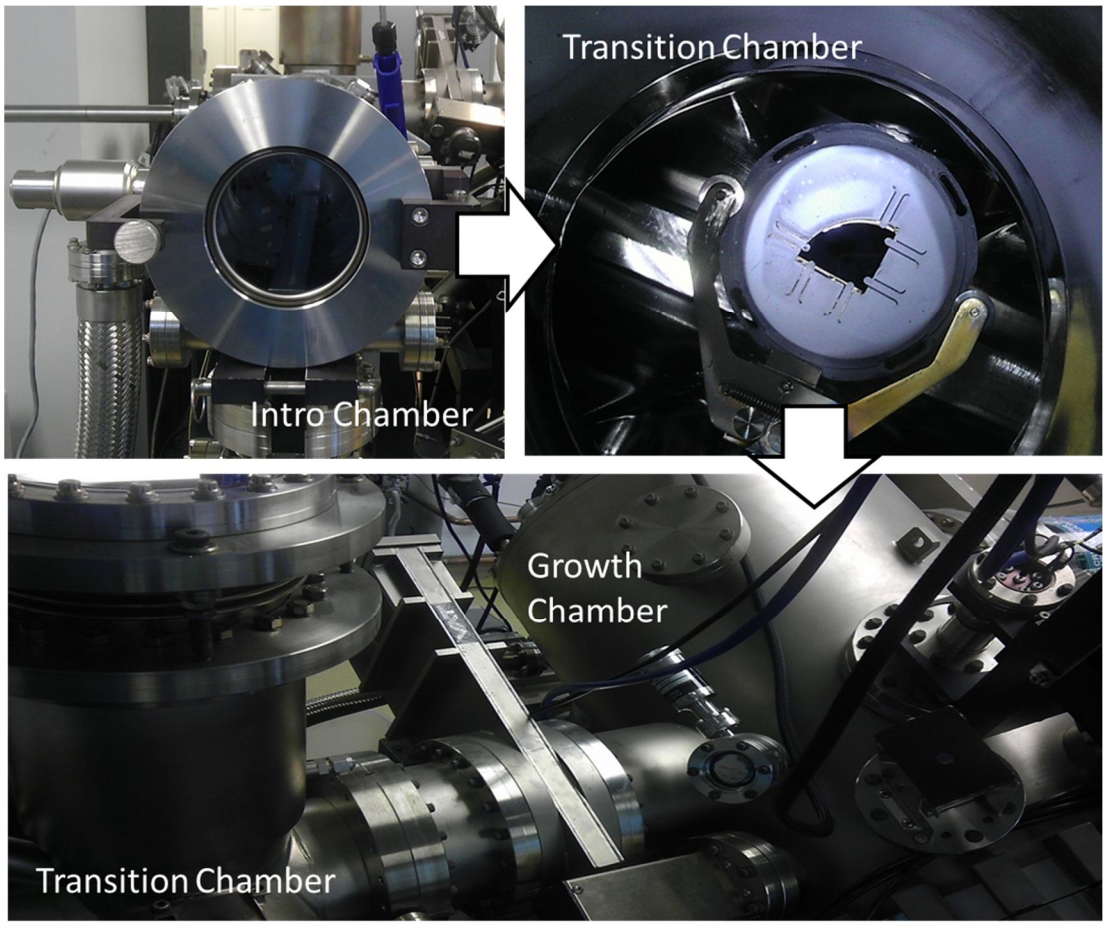

Figure 5.4 Sample manipulation in Model 930 MBE available in Compound Semiconductor Research Lab.

Once the sample mounted in the growth chamber, it is thermally cleaned by gradually raising the substrate temperature (5-10 degrees (C)/minute) under Arsenic overpressure until the substrate desorption temperature is reached; for a undoped semi-insulative GaAs substrate oxide desorption occurs at approximately 580 degrees Celsius. This process is monitored in situ by RHEED and the crossover point is indicated by a diffused radiance to a distinct, sharp diffraction streaks. Once the oxide desorption point is reached, the substrate is removed of the

protective oxide layer and is ready for epitaxial deposition. The design of the device in question, governs the projected growth time, as each epitaxial layer is a function of the compound deposition rate (Å/s) and the associated thickness of each layer. Figure 5.5 depicts the schematic of the reflective modulator device considered in this dissertation.

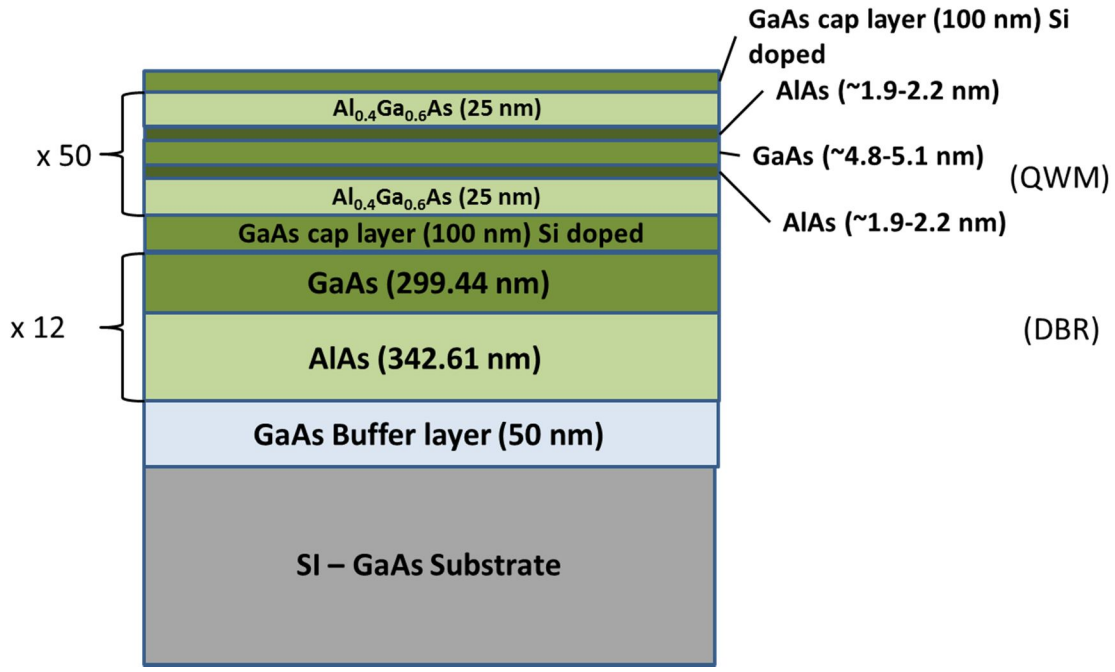

Figure 5.5 Schematic of MIR reflective modulator.

The beam equivalent pressure of each material is evaluated and recorded by an ion gauge fixed at the substrate growth position. This gives an indication of particle flux of material present at the surface of the substrate and allows for compensation if discrepancies occur from theoretical values. The flux of each material is deterministic of temperature and is used in the device design is measured; for this particular device the Al and Ga flux is measured from the respective Knudsen effusion cell. With the appropriate flux measurements and growth rates determined, the recipe entailing the physical attributes of the structure is composed using MBE computer software. The

resultant recipe is executed and grows the associated semiconductor epitaxial layers through the use of sequentially timed mechanical shutters controlling the molecular flow of each element during the growth process.

For this specific device, two separate recipes are invoked (for the quantum well modulator region and the reflective region). The growth process starts with the distributed Bragg reflector structure monitored by RHEED. Once this region is completed, the cell temperatures are adjusted to account for flux drifting and the substrate temperature is slightly lowered to before the quantum well region begins growth.

5.2 *In Situ* Growth Monitoring using RHEED

Each stage of the reflective modulator of this dissertation is periodically monitored by RHEED. The surface morphology is evaluated during the growth of each individual stage. The DBR layer begins with a quarter-wave layer of GaAs upon the undoped GaAs substrate followed by the quarter-wave AlAs layer. These layers are repeated 12 times (ending with an AlAs layer) for a total of 24 Bragg layers. The mirror is then capped with a 100 nm Si n-doped (~10^{18} cm^{-1}) layer to serve as an electrode for fabrication. The surface morphology of the layers is monitored periodically throughout the growth process with RHEED.

Once the DBR region is completed, the quantum well modulator stage begins growth (after the appropriate system adjustments). This stage is comprised of 50 double barrier GaAs quantum well structures followed by 100 nm Si n-doped (~10^{18} cm^{-1}) cap

layer to serve as the top electrode. The composite structure's surface morphology is then analyzed using RHEED. Resultant 2x and 4x diffraction fringe patterns during substrate rotation (as provided by the RHEED camera Figure 5.6), indicate 2 times by 4 times lattices spacing. This lattice spacing is characteristic to surface reconstruction of GaAs growth on (100).

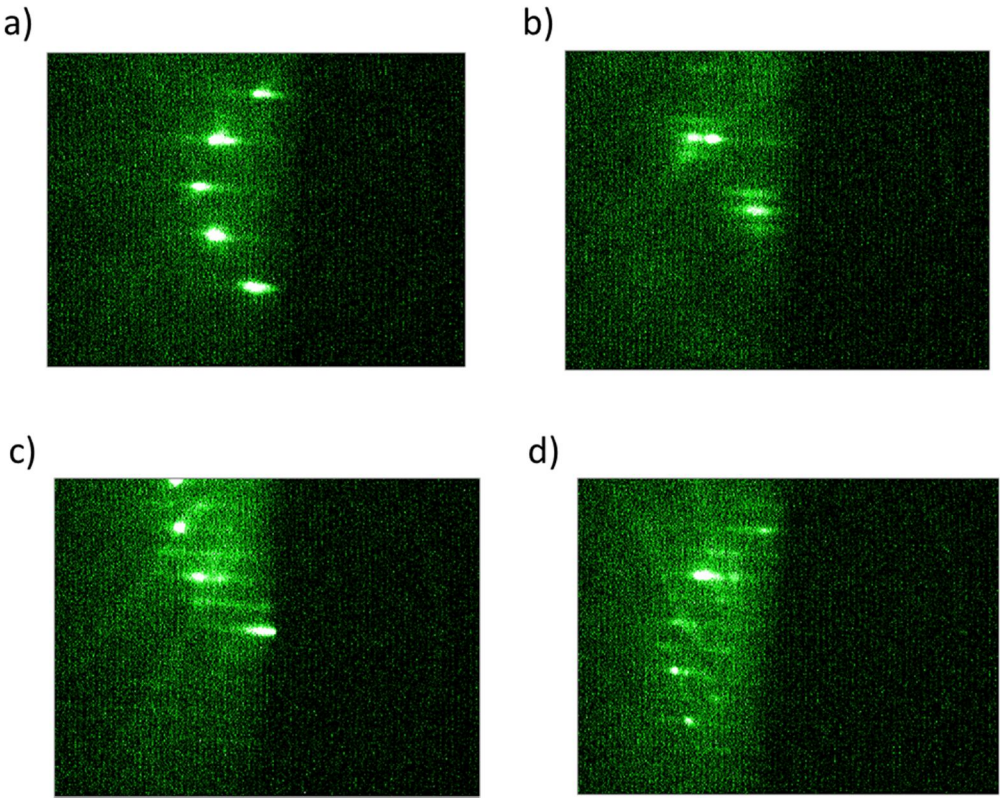

Figure 5.6 RHEED diffraction fringes on (100) substrate.

5.3 Device Fabrication and Metallization Process

Once the growth process is completed, the structure is patterned and is deposited with ohmic metal contacts for electrical characterization. This is done through a series of fabrication steps that pattern, deposit, and etches the structure in order to construct an operational device. Photolithography is used to pattern the structure into

tall pillar-like structures using UV exposures and UV resistant masks. This process is described in greater detail in the schematic of Figure 5.7.

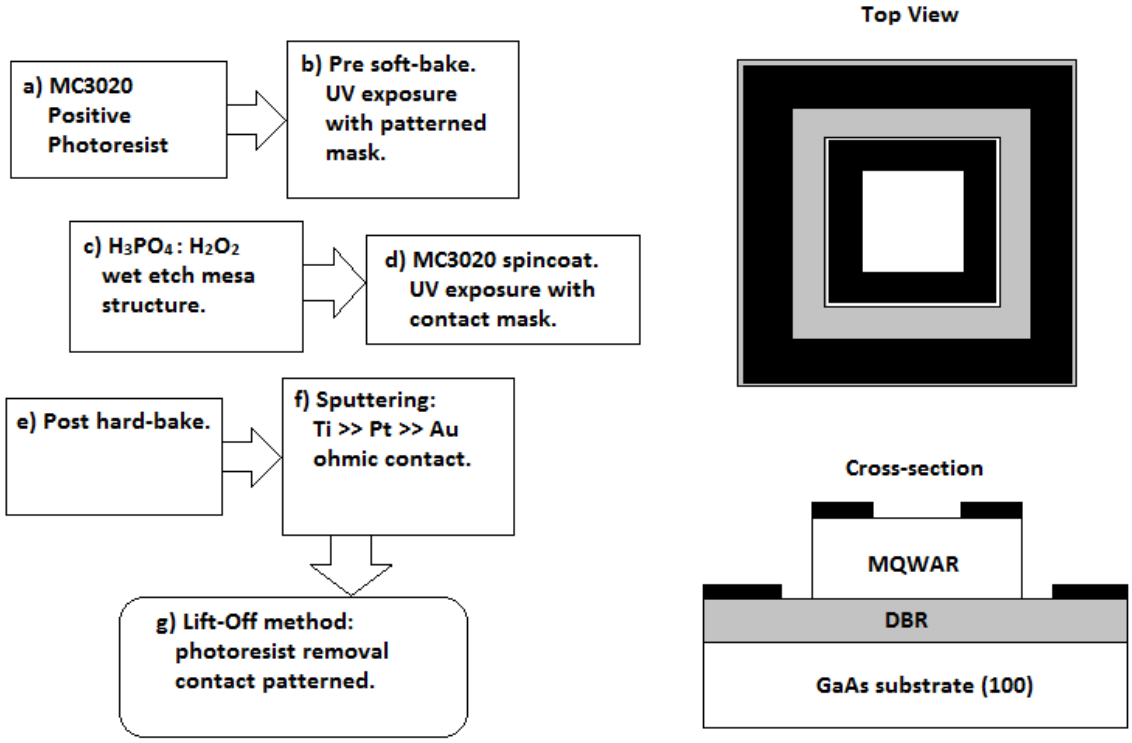

Figure 5.7 Schematic of photolithography and metallization process. a) Sample is spin-coated with MC3020 positive photoresist (3000 RPM for 30 secs to achieve approximately 3 μm thickness) b) The photoresist coated sample is then soft baked (110°C for 30 secs) and exposed to incident UV radiation under a patterned UV mask, hard baked at 120°C for 1-2 mins, and soaked in developer. c) The patterned photoresist is then chemically etched with H_3PO_4 : H_2O_2 (1:4: 45) to pattern square mesas on the device. d) The photoresist is removed in Acetone and re-coated with MC3020 and repatterned using the contact mask under UV exposure. e) The sample is then developed and hard baked for 1-2 mins at 120°C. f) The mesa structures (now spin-coated with photoresist and patterned using the contact mask) is sputtered with Ti>>Pt>>Au metals using a Sputtering machine. G) the lift-off method is used to remove the unwanted metal resulting in the patterned ohmic contacts upon the structure**.**

After the metallization process is complete, the sample is equipped with ohmic metal contacts and ready for electrical characterization. This process is completed in the sputtering facilities available in the University of Missouri-Columbia.

Scanning electron microscopy (SEM) is employed to evaluate the quality of the wet etch during the fabrication process (Figure 5.8 and 5.9). From the SEM images very distinct structures (mesas) are apparent with nano-scaled aberrations caused by

selective etching of the chemical solution. The rigidity of the mesas can be further refined using plasma etching techniques to produce sharper edges and reduce the effects of undercut. The selectively etch artifacts are likely attributed to discrepancies during heteroepitaxial growth effecting material compositions and/or quality. Such physical traits on the device may present adverse operational effects and impede desired performance specifications. The quality of material growth has a substantial impact on the ability to successfully pattern and etch structures, therefore great emphasis is placed on the growth of high quality, mirror-like surfaces during MBE growth. Figure 5.10 shows microscopic images of Ohmic contacts. Rigid edges occur during the Lift-off process and may adversely affect electrical performance.

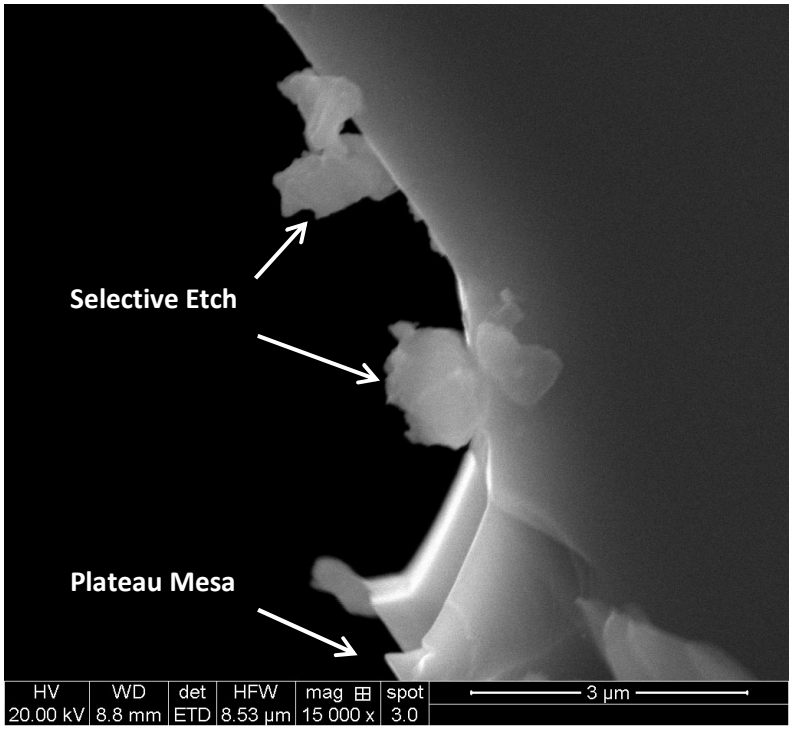

Figure 5.8 SEM image of sample mesa etched with a Phosphoric acid solution (H_3PO_4:H_2O_2:H_2O). Selectively etched artifacts are apparent.

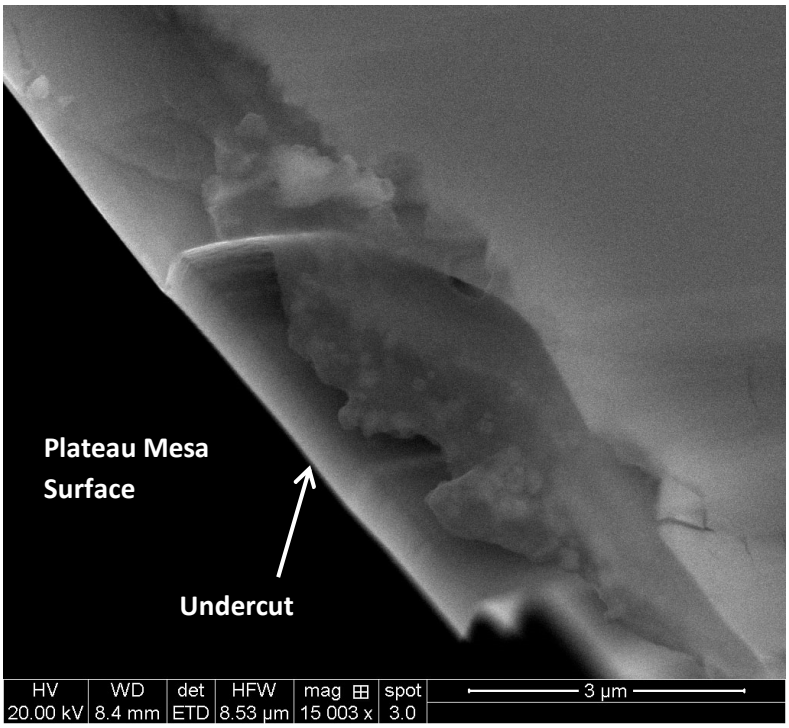

Figure 5.9 SEM image of mesa structure with undercutting.

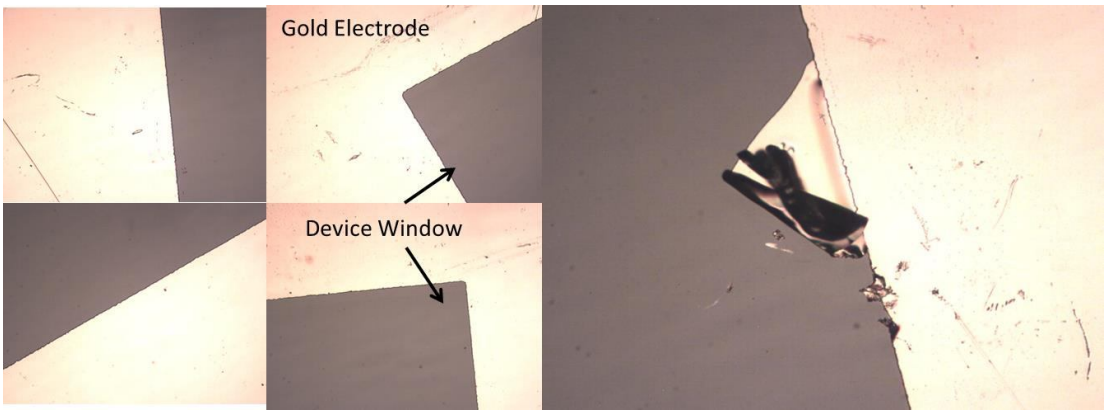

Figure 5.10 Microscopic image of electrode patterned. Rigid edges occur during electrode patterning in the Lift-off process.

CHAPTER 6

DEVICE CHARACTERIZATION

This chapter presents the results of each optical characterization method and the resultant spectra.

6.1 Surface Analytics

The surface of each composite device is examined using microscopy techniques and data visualization analysis software. Each sample is grown by the process described in Chapter 5. After successful growth operation, the sample surface is visually characterized to evaluate the physical quality of the device structure. Defects encountered during growth propagate to each subsequent epitaxial layer. Therefore, observing the surface of the device gives sufficient indication of the apparent defects within the structure. These defects are marked by dark cavities on the microscopic image. The deeper the defect lies within the structure, the darker the cavity appears. Through the use of Gwyddion, a data visualization and analysis software, the depth of defects for a specific feature size can be determined. Figures 6.1-6.6 show the surface quality and defect depth of each sample. The samples characterized below show areas of high smoothness and mirror-like quality.

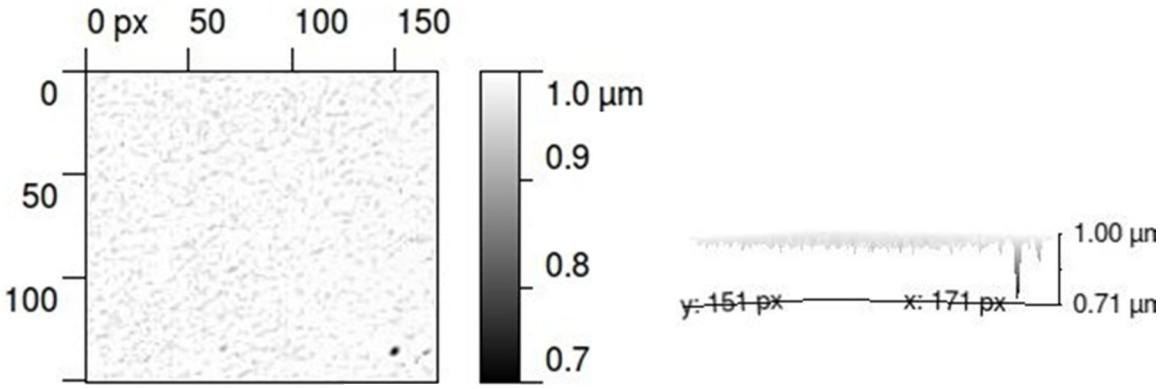

Figure 6.1 M278 surface roughness scan using optical microscopy. Image analysis shows depth of defect and surface roughness with a submicron (~290 nm) defect within the sample(10x magnification and 256 mm^2 approximate area).

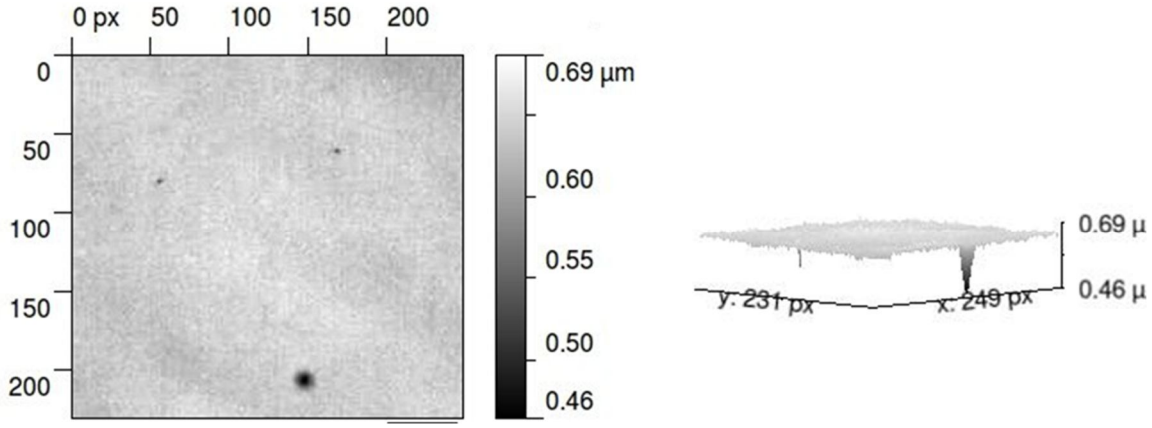

Figure 6.2 M258 surface analysis shows depth of defect ~230 nm within the sample(10x magnification and 400 mm^2 approximate area).

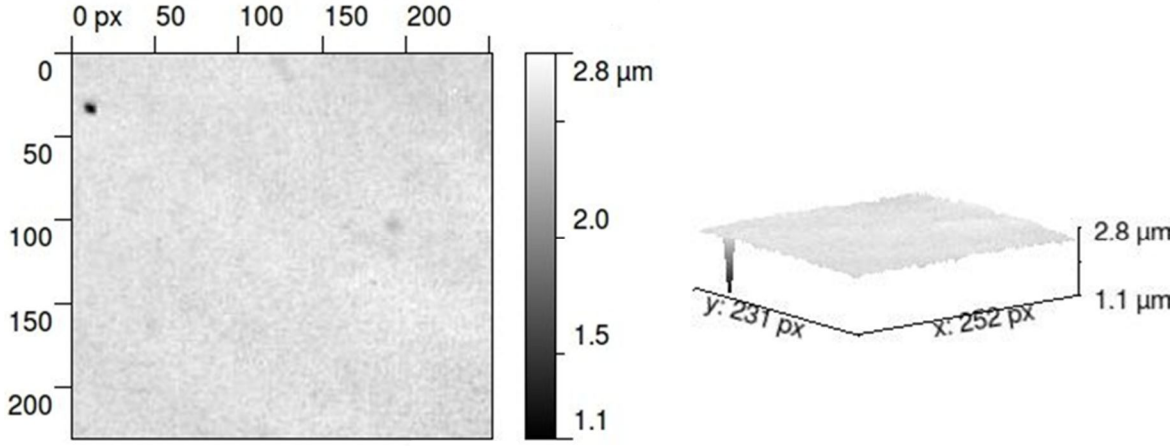

Figure 6.3 M272 deep defect (~1.7 µm) within the sample(10x magnification and 400 mm^2 approximate area).

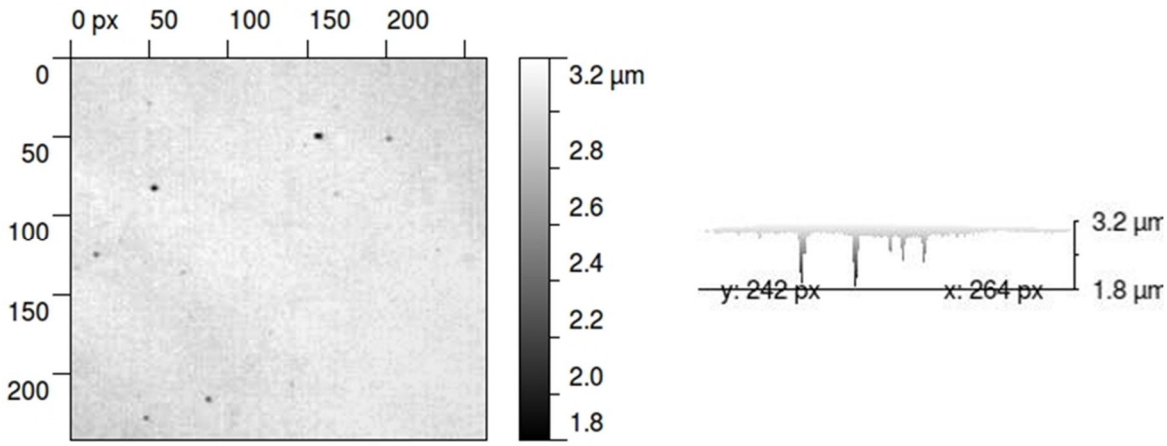

Figure 6.4 M277 with multiple point defects 1.4 µm deep (10x magnification and 400 mm^2 approximate area).

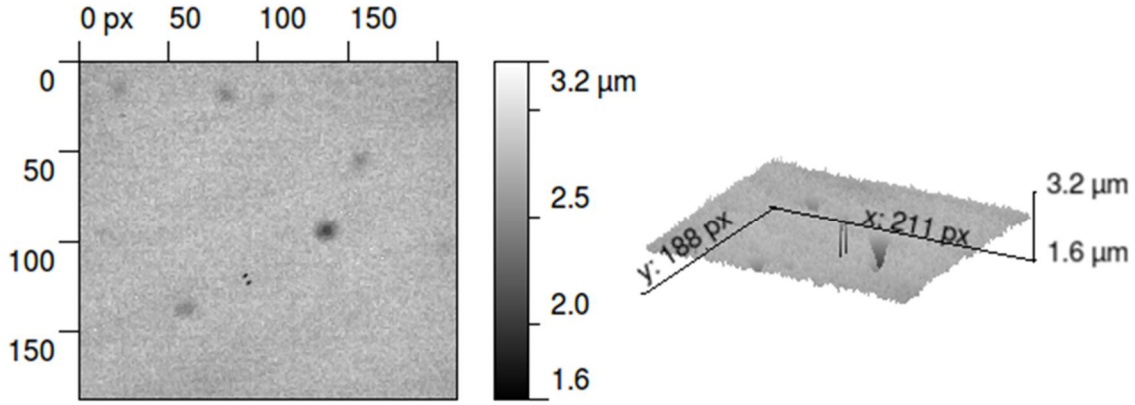

Figure 6.5 M280 surface roughness with point defects. (10x magnification and 225 mm^2 approximate area).

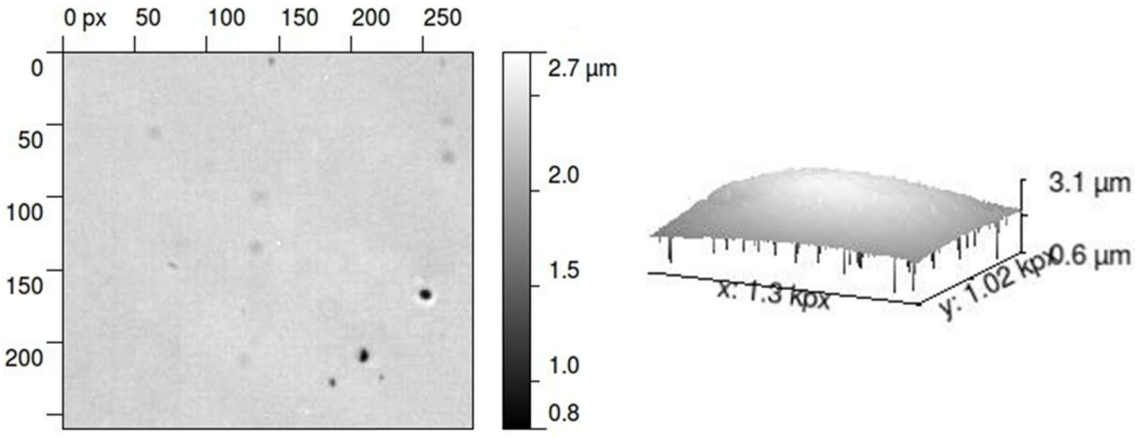

Figure 6.6 M276 non uniformity with deep level defects approximately 2.5 µm deep. (10x magnification and 400 mm^2 approximate area).

The growth temperature of each sample is 580 °C as it has proven affective for construction of devices with the GaAs/AlAs material system. The surface reconstruction is monitored *in situ* during MBE growth and the surface analyzed subsequently. An ideal structure exhibits layer uniformity across the entire wafer. Therefore, the surface of the finished structure should exhibit the surface properties of the substrate. Uniform layers are marked by a mirror-like surface appearance. The level of uniformity to which the structure exhibits directly correlates to the growth environment (i.e. substrate temperature, As_4 overpressure, and flux ratio). Each of which are manipulated to achieve the optimal growth condition for yielding uniform layered structures.

Another factor that plays a major role in the material distribution upon the substrate is the mechanism in which the sample is held on the substrate heater. Each sample is mounted on Uni block holders with heat diffusers mounted on the back of the substrate to ensure a uniform heat distribution. Using this method, typically results in slightly higher substrate heater temperatures (due to the fact that additional energy is needed to heat the substrate through the diffuser). Though the relative substrate temperature does not change (at the surface when considering desorption and adsorption) additional heat energy is added to the growth environment and influence surface migrations of atoms and mean free paths of incident molecules. Areas of high mirror-like quality (less roughness) are observed using this optical microscopy technique and the level of deep defect anomalies are visualized in Figures 6.1-6.6.

The surface quality of each device is also analyzed using Atomic Force Microscopy. Isolated regions of smooth (low roughness) areas can be found on the

surface of each sample. It is in these localized regions that the device performance is more desirable. Though absolute smoothness of growth upon the substrate is ideal, the average surface roughness is increases with epitaxial distance in the growth direction.

Many experiments were conducted in order to fully optimize the growth environment conditions to produce samples with minimal surface aberrations and interior defects. High quality homo/heteroepitaxial layers are essential in the fabrication of functioning optoelectronic devices. The surface morphology of each subdevice is considered to characterize the optical properties of the composite device. Each sample is grown on semi-insulate GaAs (100).

6.1.1 AFM of DBR Design

The as-grown AFM topography scan regions (2x2 μm scan area) of DBR subdevice samples are depicted below. The topography scans show the acute physical characteristics at each sample surface. The formation of nano-scale valleys become apparent with material deposition rates > .9 Å/s under variable V/III beam equivalent pressure ratio (30-16:1). The growth temperatures range from 580-630˚C. In particular, the growth of the AlAs layers has proven extremely difficult on GaAs (100). This is primarily due to the AlAs/GaAs interfaces between heteroepitaxial layers. Surface dislocations at the substrate interface are inherent to the thermal cleaning and desorption process of MBE growth. These dislocations are enhanced by bending at the AlAs/GaAs interfaces and difference in material electric charge. Dislocations can be

suppressed by reducing the material deposition rates, modulation doping of layers, or increasing the surface entropy by increasing the growth temperatures.

These dislocations can impede the performance in thin layer (< 90 Å) superlattice heterostructure devices, but have minimal effect on DBR functionality. This is largely due to the fact that the GaAs and AlAs layer thicknesses are very large (>1000 Å) and have material characteristics similar to that of the bulk material (as opposed to thin film characteristics). Therefore, the average surface roughness (~2-4 Å) associated with the DBR samples are negligible and is not detrimental to device functionality. Figures 6.7 and 6.8 displays the topography of 2x2 μm heteroepitaxial GaAs/AlAs layers. The surface texture profile for each sample is depicted in Figures 6.9 and 6.10 with surface parameters listed in Table 6.1 below.

Table 6.1 Surface Roughness parameters of heteroepitaxial GaAs/AlAs DBR samples for 5x5 μm^2 surface area topography.

	R_a (nm)	R_q (nm)	R_t (nm)	R_v (nm)	R_p(nm)	W_a (nm)
M2-121	.55	.81	5.7	2.6	3.1	820.1
M2-122	.35	.46	2.7	1.7	1	44.8

The roughness parameters of Table 6.1 show a roughness average (R_a) of <.55 nm. The roughness parameter gives indication of the high frequency variation depth and height at the device surface. This value is an arithmetic deviation, therefore these samples vary between 3-6 Å (corresponding to 1-2 MLs). The root mean square roughness (R_q) gives the relative roughness associated with the texture profile. The values R_t. R_v, and R_p are the maximum height of roughness, maximum roughness valley depth, and the maximum roughness peak height respectively. The waviness (W_a) is a

measure of sample flatness. This parameter is a measure of spacing in the lateral direction of features greater than the roughness sampling length.

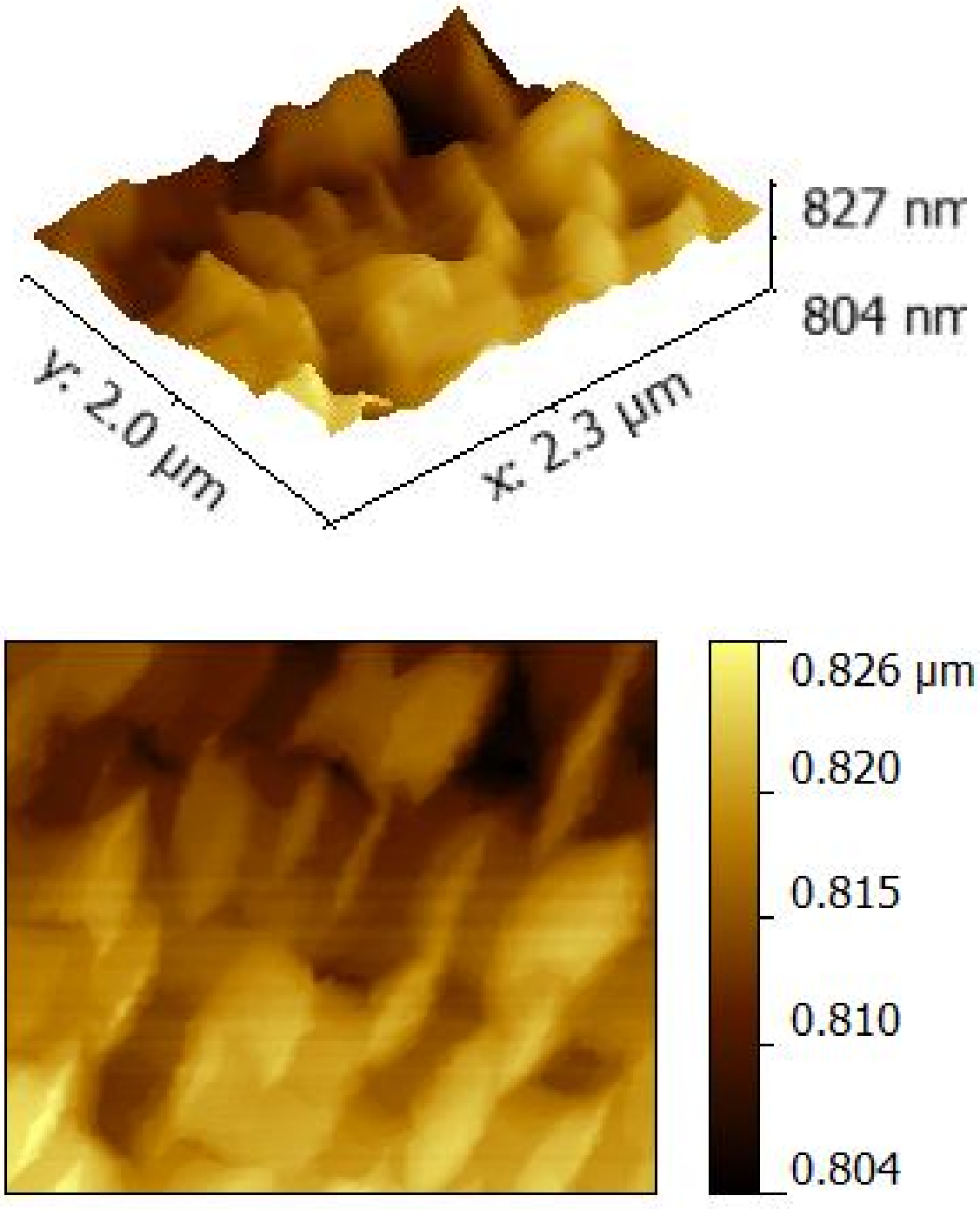

Figure 6.7 Sample M2-121 AFM 2x2 µm three dimensional surface scan (top) topography image (bottom) of heteroepitaxial GaAs/AlAs DBR region grown on GaAs (100). Growth temperature: 620 ˚C with V/III BEP ratio 21:1 (GaAs) and 30:1 (AlAs). Surface average roughness: R_a = 5.5 Å, RMS roughness: <.81 nm.

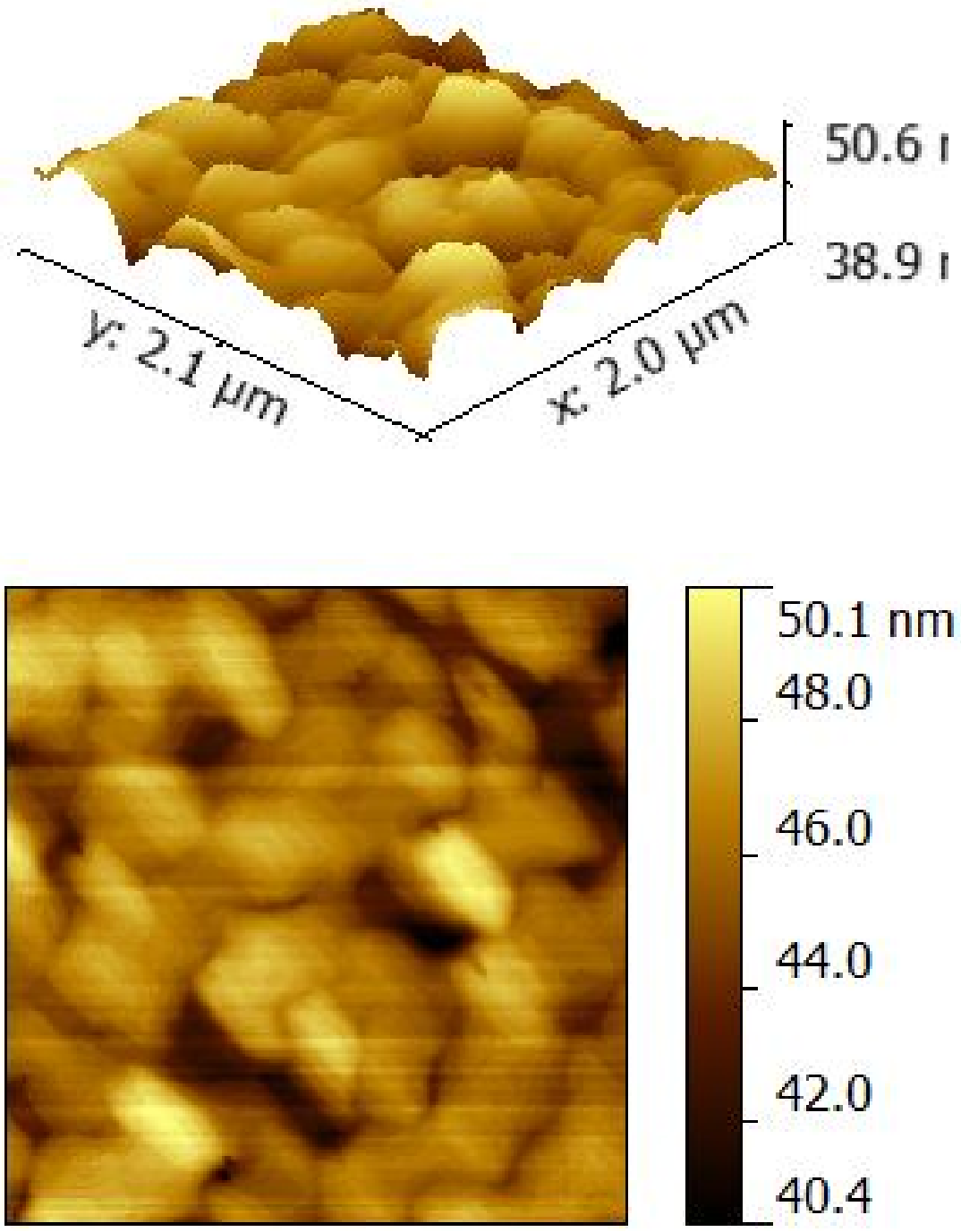

Figure 6.8 Sample M2-122 AFM 2x2 µm three dimensional surface scan (top) topography image (bottom) of heteroepitaxial GaAs/AlAs DBR region grown on GaAs (100). Growth temperature: 620 ˚C with V/III BEP ratio 21:1 (GaAs) and 30:1 (AlAs). Surface average roughness: R_a = 3.5 Å, RMS roughness: <.46 nm.

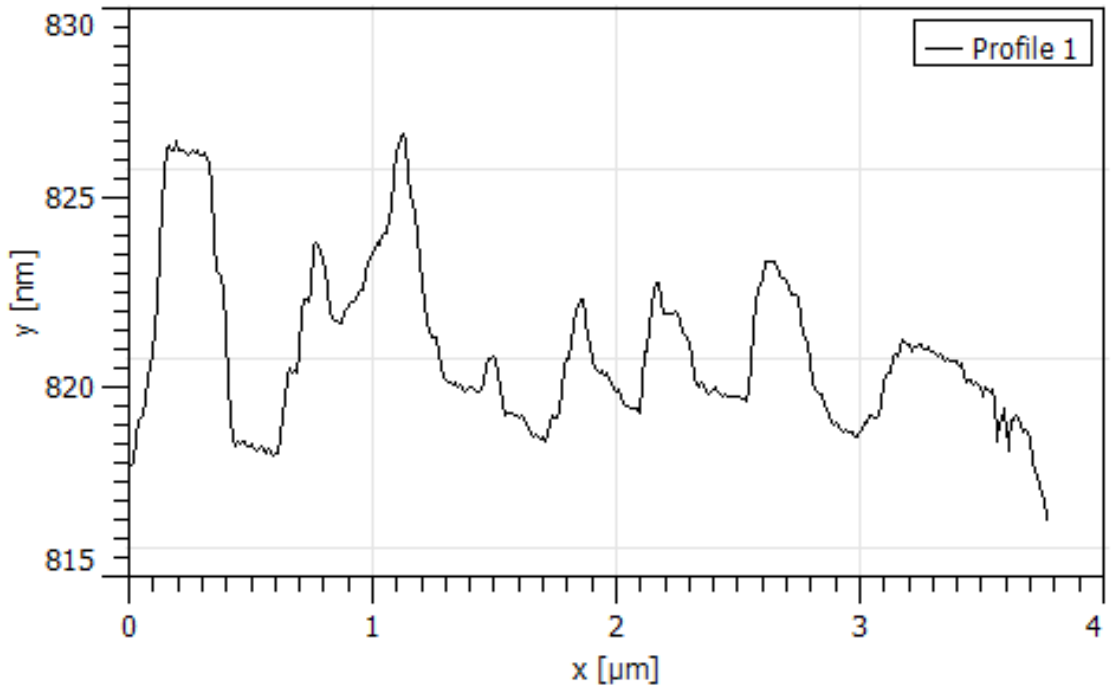

Figure 6.9 Sample M2-121 4 µm surface texture profile of GaAs/AlAs heteroepitaxial layers DBR on GaAs (100). Maximum Roughness height R_t = 5.69 nm and Maximum roughness valley depth R_v = 2.61 nm.

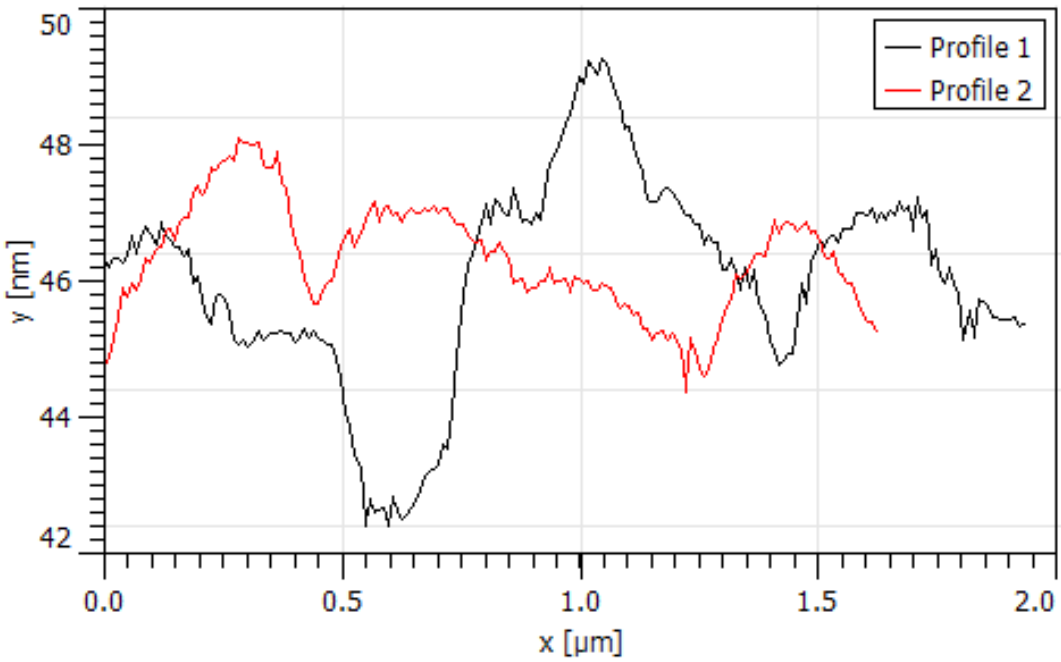

Figure 6.10 Sample M2-122 2 µm surface texture profile of GaAs/AlAs heteroepitaxial layers DBR on GaAs (100). Maximum Roughness height R_t = 2.5 nm and Maximum roughness valley depth R_v = 5.03 nm.

The texture profile of Figure 6.9 shows a 4 μm lateral cross-section with distinct valleys and peaks of variable heights. The spacing between the periodic peaks (waviness) of sample M2-121 is much larger than that of M2-122. This can be attributed to the fact that the features on the surface of M2-122 have much lower heights/depths and are wider (or flatter) than those of M2-121 resulting in a lower waviness (i.e. greater flatness).

6.1.2 AFM of Quantum Well Design

The as-grown AFM topography scans of the quantum well regions are shown in Figures 6.11 and 6.12. Sample M2-127 has an average surface roughness much lower than that of M2-134 and therefore a lower waviness. From the topography scans the size in surface features is very apparent and the maximum heights and depth are listed in Table 6.2. The texture profile of sample M2-127 exhibits a high frequency response with little vertical deviations characteristic of flatter surfaces. Conversely, sample M2-134 is marked by large valleys on the surface resulting in a very low frequency surface texture map indicating high roughness at the surface (Figure 6.14). The height of these terraced nanostructures are approximately as high as 9.3 nm off of the epitaxial plane. This substrate orientation (100) has proven effective for both homo and heteroepitaxial growths of this particular nature due to adequate surface energy and minimal strain fields between materials. Due to the natural variation of surface reconstructions in the growth direction, the quantum well energy states (intersubband) can be dispersed and lead to an inhomogeneous broadening effect for rougher samples. This makes the

reduction of surface roughness for the quantum well region particularly important as the performance of the device is more sensitive to the acute surface features than that of the DBR region due to the much smaller thicknesses of the epitaxial layers. Since surface morphology is strongly dependent on the substrate orientation, each sample is grown on semi-insulate GaAs (100) to reduce lattice strain effects and unwanted misfit dislocations at the substrate device interface.

Table 6.2 Surface Roughness parameters of heteroepitaxial GaAs/AlAs/$Al_xGa_{1-x}As$ tunnel barrier quantum well modulator samples for 5x5 μm^2 surface area topography.

	R_a (nm)	R_q (nm)	R_t (nm)	R_v (nm)	R_p(nm)	W_a (nm)
M2-127	.81	1.02	5.03	2.5	2.5	110.6
M2-134	1.3	1.6	9.3	4.04	5.2	173

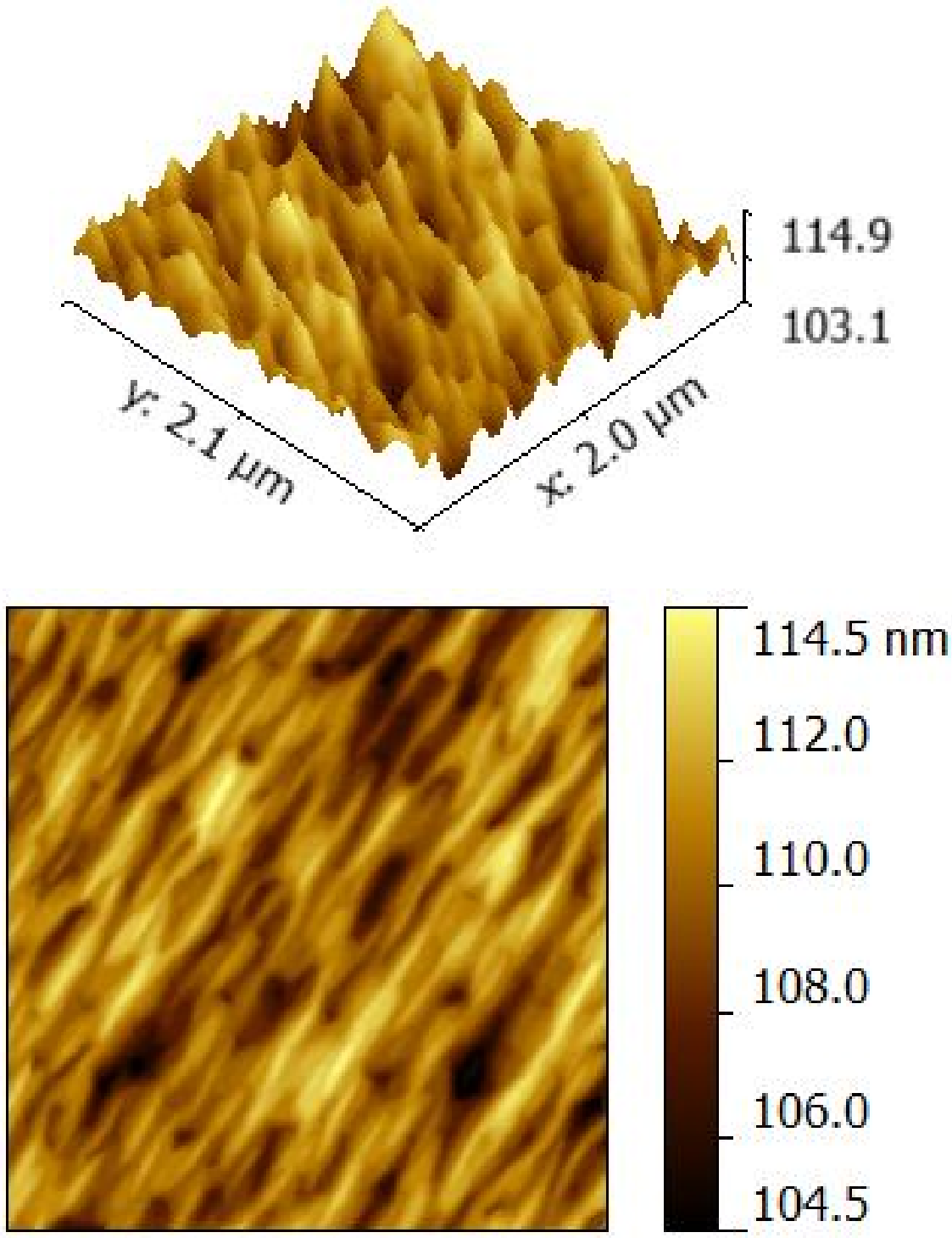

Figure 6.11 M2-127 AFM 2x2 µm three dimensional surface scan (top) topography image (bottom) of heteroepitaxial GaAs/AlAs DBR region grown on GaAs (100). Growth temperature: 610 ˚C with V/III BEP ratio 17:1 (AlGaAs), 21:1 (GaAs) and 30:1 (AlAs). Surface average roughness: R_a = 8 Å, RMS roughness: <1 nm.

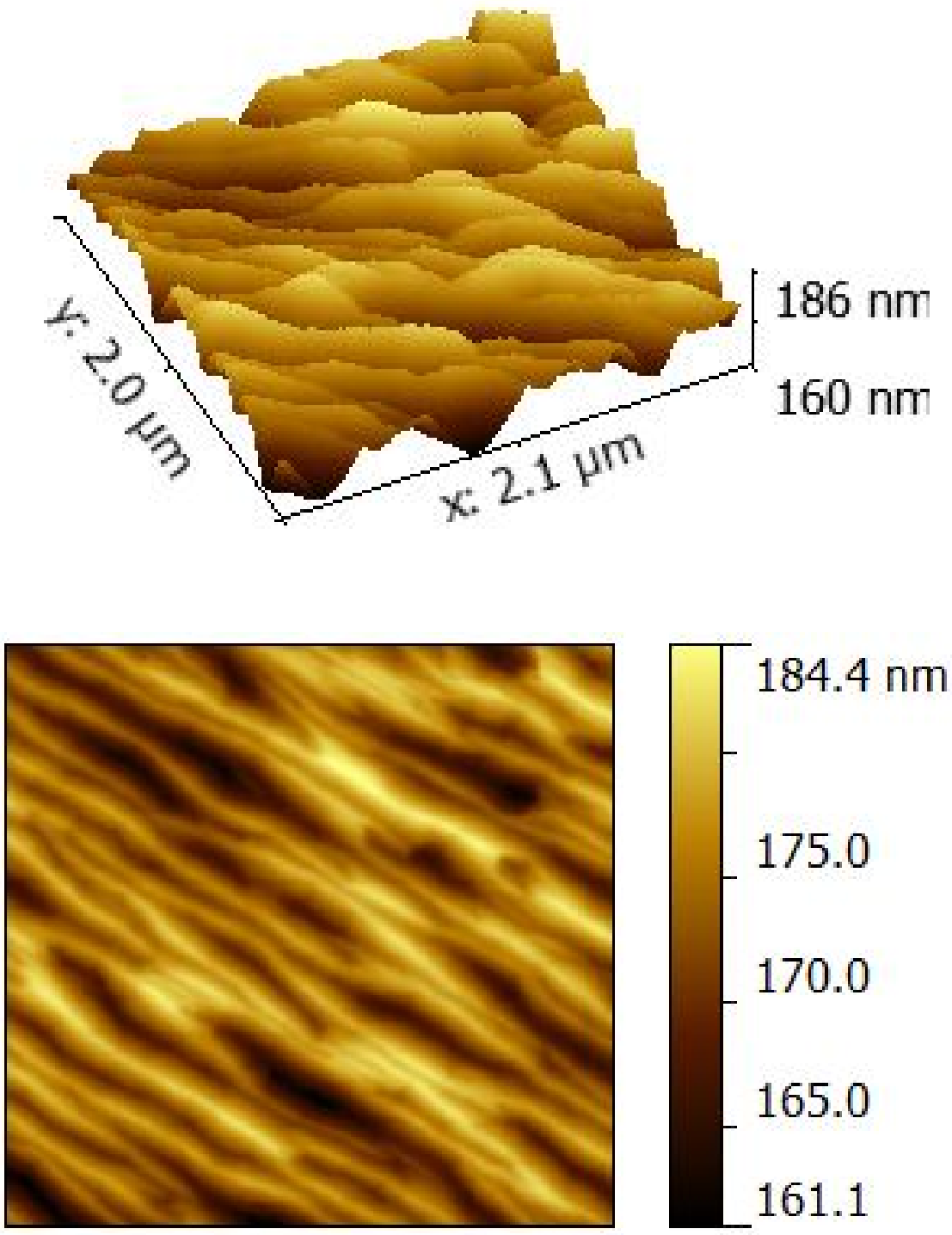

Figure 6.12 M2-134 AFM 2x2 μm three dimensional surface scan (top) topography image (bottom) of heteroepitaxial GaAs/AlAs DBR region grown on GaAs (100). Growth temperature: 610 ˚C with V/III BEP ratio 17:1 (AlGaAs), 21:1 (GaAs) and 30:1 (AlAs). Surface average roughness: R_a = 1.3 nm, RMS roughness: <1.6 nm.

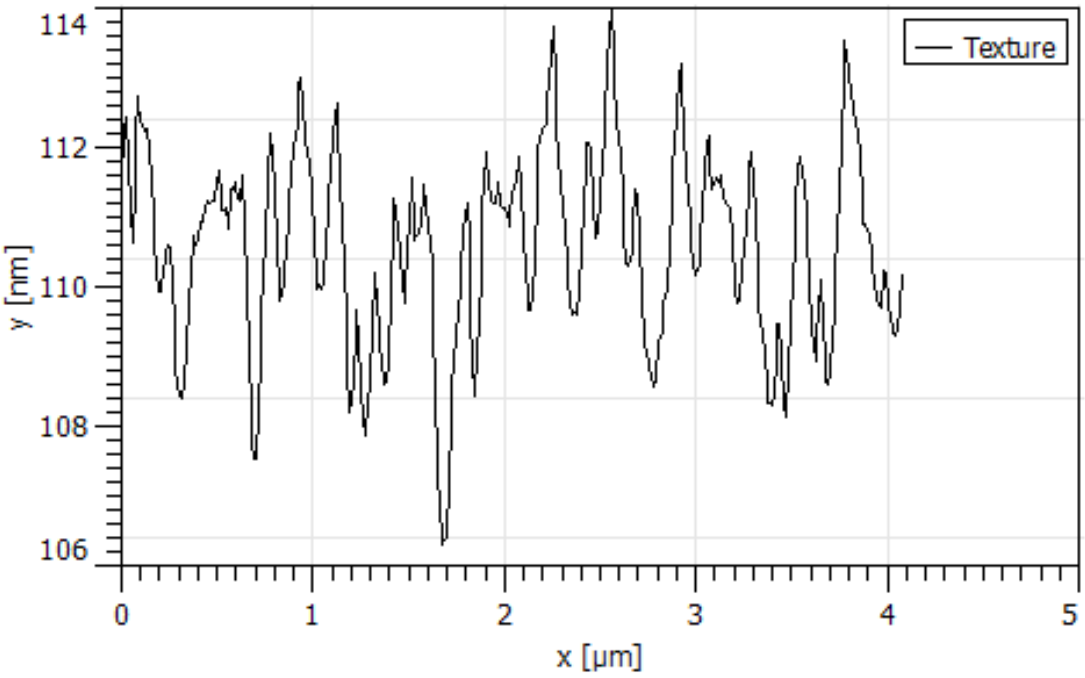

Figure 6.13 Sample M2-127 4 µm surface texture profile of GaAs/AlAs heteroepitaxial layers DBR on GaAs (100). Maximum Roughness height R_t = 5.69 nm and Maximum roughness valley depth R_v = 2.61 nm.

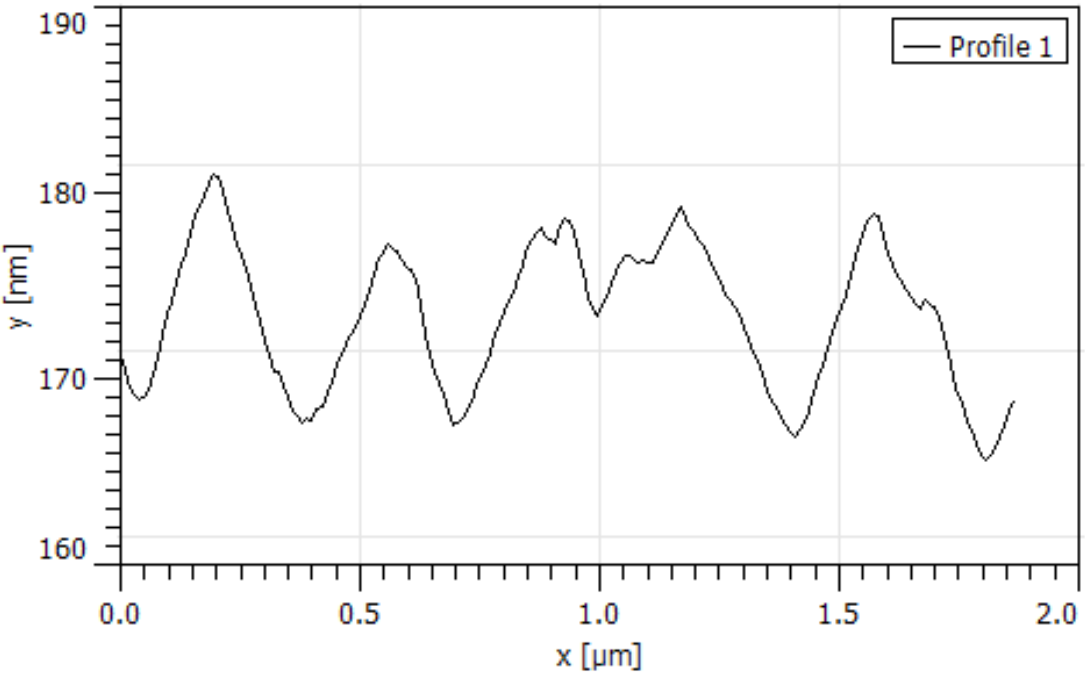

Figure 6.14 Sample M2-134 2 µm surface texture profile of GaAs/AlAs heteroepitaxial layers DBR on GaAs (100). Maximum Roughness height R_t = 9.03 nm and Maximum roughness valley depth R_v = 4.04 nm.

6.2 Optical Characterization

6.2.1 Interband Photoluminescence

Photoluminescence is a widely used optical characterization technique for analyzing surface, interface, and material quality nondestructively (discussed in Chapter 2). Traditional PL setups simply consists of a pump source oriented toward the sample at a specific angle to achieve maximum transmission into the sample (at the Brewster Angle) and a detector or spectrometer position to capture emissions orthogonal to the sample surfaces. Photons with the greatest energy are emitted orthogonal to the surface and for this reason PL is measured orthogonal to the epitaxial layers. Figure 6.15 depicts the PL setup used for optical characterization.

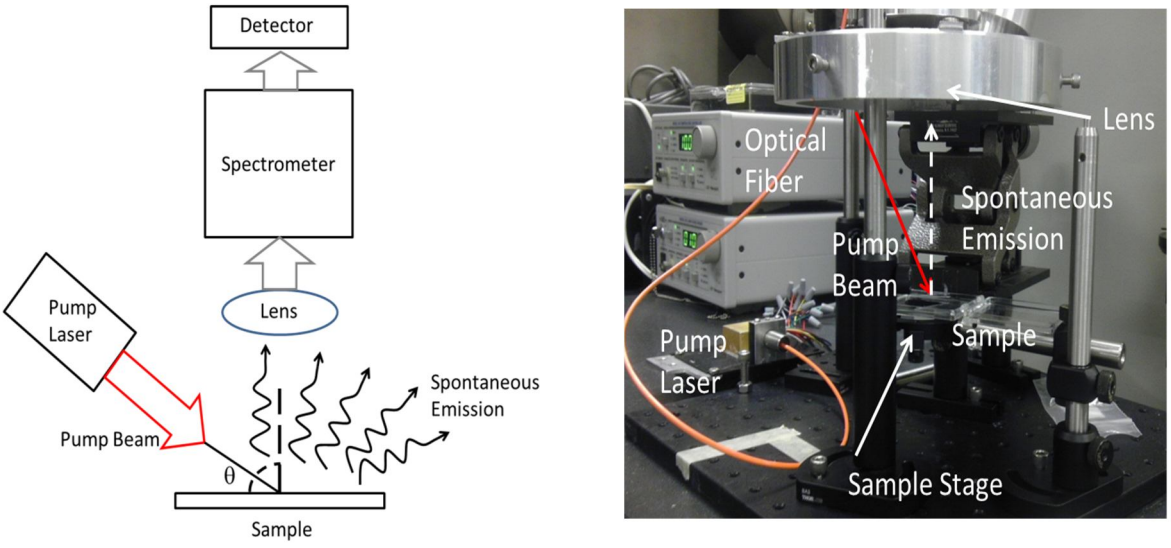

Figure 6.15 Schematic (left) and experimental setup (right) of PL optical characterization where the incident angle is arbitrarily chosen at approximately 45°C.

The PL spectrum of $Al_{0.4}Ga_{0.6}As$ quantum well structures is considered. Each sample is constructed in similar fashion in the EPI Model 930 MBE chamber. The PL spectrum of

Sample M258 is a Gaussian-like shape with an absolute maximum located at approximately 1.587 eV with a high-energy tail. This implies that a band to band transition of approximately 1.6 eV in magnitude is necessary to produce such luminescent peaks. The tailing phenomenon associated with the curve is associated with the heavy doping of the quantum wells. This peak is the result of spontaneous emissions from free electrons in the conduction band in the GaAs quantum well layer. From Figure 6.16, a noticeable shift in the absolute PL intensity peak can be observed. This shift is characteristic of heavily doped samples as noted by Burstein and Moss [50-52]. Sample M278 is modulation doped (as opposed to uniform doping of M258 and M272) the lower energy PL shifting is not yet understood. Using an empirical model, the doping level and Fermi energy can be approximated from the PL peak as a function of the peak width (eqn. 6.1).

$$\Delta E = 3.84 \times 10^{-14} n^{\frac{2}{3}} \tag{6.1}$$

From equation 6.1 and the change in energy (ΔE) taken as the full width at half maximum (FWHM) of the PL intensity of Sample M258, the doping concentration (n) is determined to be 2.813×10^{18} cm^{-3}. Doping the GaAs quantum well at such a donor density implies degeneracy. Degenerate semiconductor layers are layers that have been doped beyond the effective density of states (the effective density of states at the conduction band edge (N_c) of GaAs is 4.7×10^{17} cm^{-3}). In doing so, Pauli's exclusion principle plays a much greater role in the solution to the wave equation and the

electron probability cannot be simplified by Maxwell-Boltzmann approximation and must be derived from the Fermi-Dirac distribution (eqn. 6.2).

$$f(E) = \frac{1}{1 + \exp\left(\frac{E - E_F}{k_B T}\right)} \tag{6.2}$$

E_F is the Fermi Energy given by

$$E_c - E_F = -\ln\left(\frac{n}{N_c}\right) k_B T \tag{6.3}$$

where E_c is the minimum conduction band energy, N_c is the effective density of states in the conduction band, and $k_B T$ is approximately 0.0259 eV. The Fermi-Dirac function yields the probability of finding an electron in a quantum state at the energy (E) as a function of the Fermi energy (E_F); which corresponds to the lowest level the electron can reside at 0 K. From the Fermi equation for electron concentration in the conduction band (eqn. 6.2), the probability of an electron residing at the energy of the PL absolute maxima of Sample M258 is nearly zero. This implies that the carrier recombination which produces this luminescent peak occurs doesn't occur at the band edge of GaAs (which corresponds to an energy of 1.424 eV at room temperature). The luminescent peak of Sample M258 is due to the relaxation of both electrons at energies above the Fermi level and those that have been promoted into the conduction band from the

valence band. After sufficient energy absorption, recombination occurs in the quantum well layer or (the adjacent well) down into vacancies in the valence band caused by photoexcitation (a small minority of electrons may also recombine in the thick barrier layers at the GaAs/AlAs interface and contribute to the luminescence). The energies that comprise the PL peak of Sample M258 can be deciphered through the use of peak analysis software. Using a custom peak extraction module in MATLAB, the PL peak is dissolved into smaller sub-peak components that integrate to form the composite curve (Figure 6.17-19).

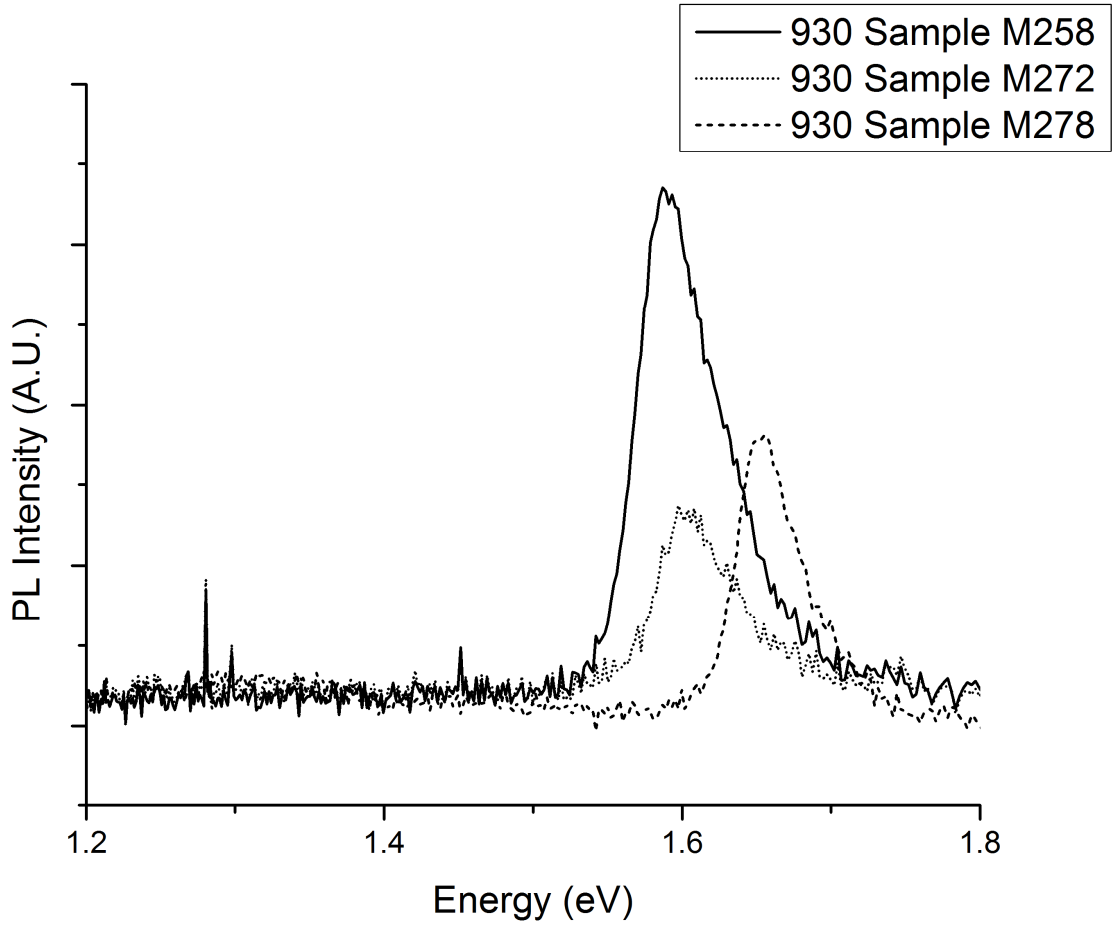

Figure 6.16 PL spectra of $Al_{0.40}Ga_{0.60}As$ double barrier quantum well structure. Sample M258 (bold), SampleM272 (dotted), and Sample M278 (dashed) is each grown in MBE at a growth temperature of 610 °C. The PL intensity of Sample 1 is distinctly greater than the other two samples.

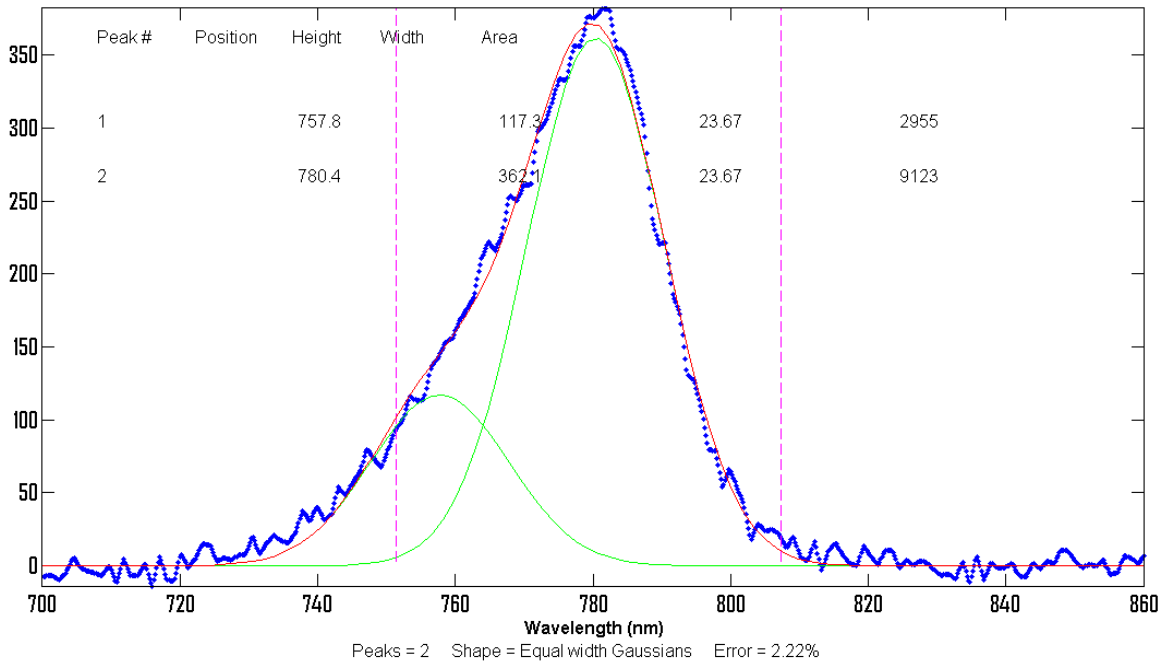

Figure 6.17 Gaussian peak analysis of Sample M258. Sub-peaks occur at 757.8 nm and 780.4 nm which corresponds to an energy separation of approximately .047 eV. This separation is approximately equal to E_c-E_F.

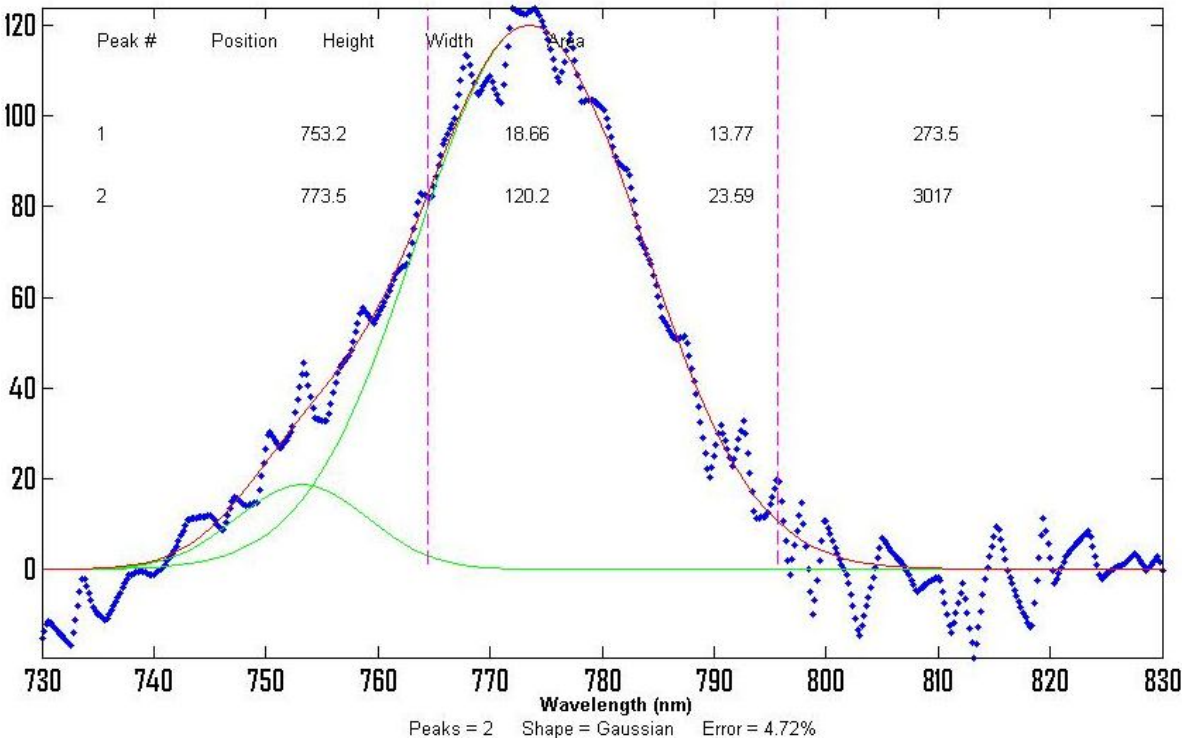

Figure 6.18 Gaussian peak analysis of Sample M272. Sub-peaks occur at 753.2 nm and 773.5 nm which corresponds to an energy separation of approximately .043 eV. This separation is approximately equal to E_c-E_F.

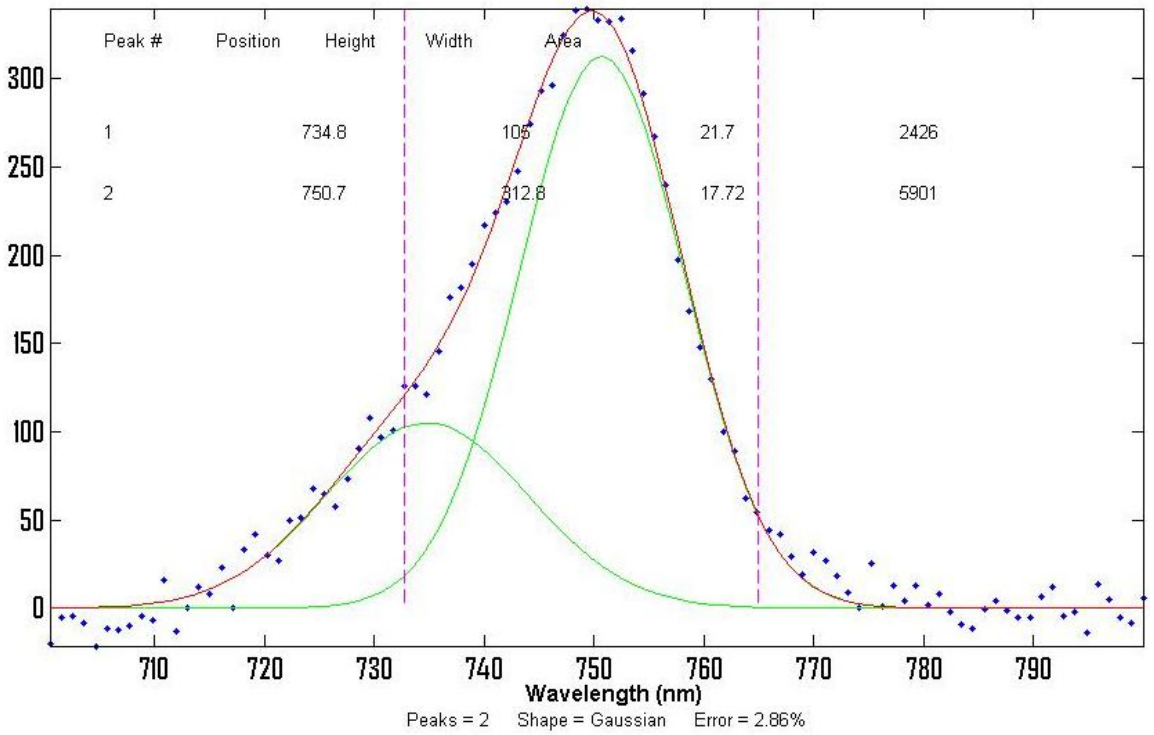

Figure 6.8 Gaussian peak analysis of Sample M278. Sub-peaks occur at 734.8 nm and 750.7 nm which corresponds to an energy separation of approximately .036 eV. This separation is slightly below the E_c-$E_{F\,l}$evel.

Figure 6.16 shows the PL spectra for three quantum well samples. Each peak falls relatively close to the energy of 1.6 eV. This energy corresponds to the n=1 direct interband (Gamma) transition within the GaAs quantum well. The majority of the conduction band electrons relax within the well and irradiate at approximately 755 nm as seen from Figure 6.20. It is also apparent that electrons at the Fermi energy (approximately .04 eV above E_c) recombine at a slightly higher energy and contribute to the PL peak. The subpeaks are separated by .036 to .047 eV.

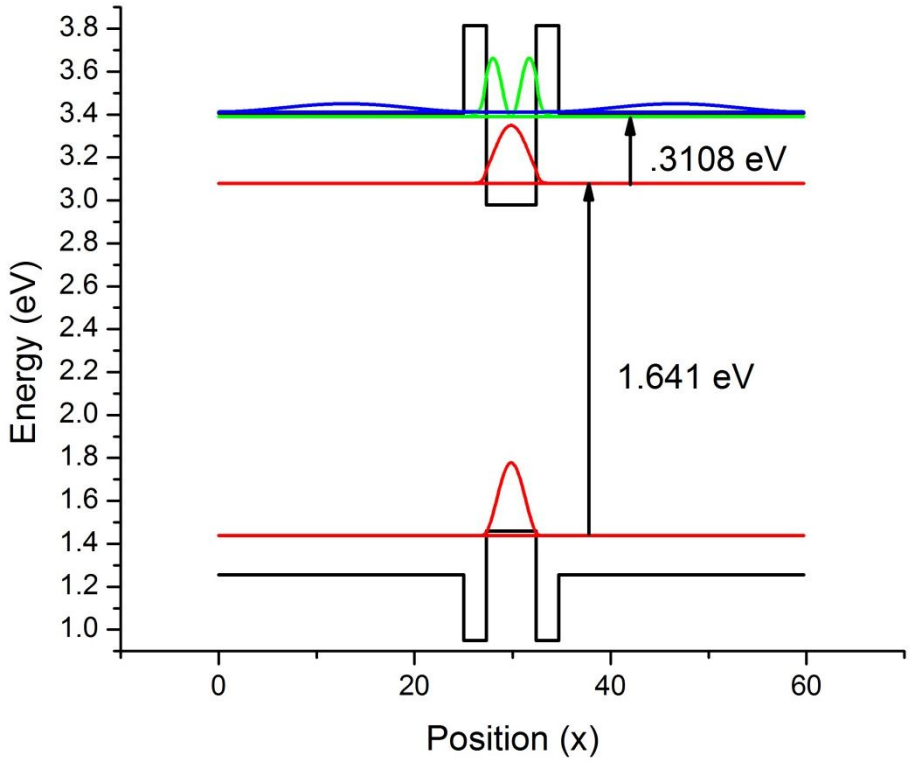

Figure 6.20 Energy band diagram of Samples M258, M272, and M278. Direct gap transition corresponds to approximately 1.641 eV energy release (755 nm).

The magnitude of the peak for Sample M258 is substantially larger than that of Samples M272 and M278. The amplitude of the PL signal directly correlates to the surface and interface quality of the structure under characterization. Samples M258 and M272 align at the same energy level indicating a similar distribution of radiative transition energies, while Sample M278 is slightly shifted toward higher energies due to discrepancy in doping. Each PL peak is marked by a steep slope on the lower energy side with a tapered tail at higher energies. With peak analysis, it is determined that the integration of the component energies give rise to this high energy tail. This separation of the component energies of each sample is approximately 0.041 which is equivalent to E_c-E_F (difference between the conduction band edge and the Fermi energy). This separation occurs due to the degenerate doping of the samples. From equation 6.3, it is determined that the

Fermi level lays approximately .042 eV above the conduction band edge. Table 6.3 lists the PL peak parameters

Table 6.3 Photoluminescence peak parameters with 40% Al composition.

	Position *(nm)*	**Height**	**Width (FWHM)**	**Area**
M258-1	757.8	117.3	23.67	2955
M258-2	780.4	363	23.67	9123
M272-1	753.2	18.66	13.77	273.5
M272-2	773.5	120.2	23.59	3017
M278-1	734.8	106	21.7	2426
M278-2	750.7	312.8	17.72	5901

A broad, low energy peak is also observed in the PL spectra of each sample. This broad peak is attributed to the donor impurity vacancy complexes that occur [46, 47]. These self-activated centers (SAC) are associated with the Si donor impurities that bundle at the antiphase domains (APD) within the lattice. The clustering of the Si donors along these Ga-Ga and As-As bounds create nonradiative and semi-radiative traps that impede the band to band transitions. This phenomenon has been previously studied in other works [45-48]. Electrons that relax into these traps still have the tendency to recombine into lower energies. This relaxation occurs at energies much lower than the band edge resulting in a broad spectrum of radiative emissions. Sample M272 best illustrates these transitions (Figure 6.18). In this particular structure, the effects of these transitions play no significant role and can be neglected.

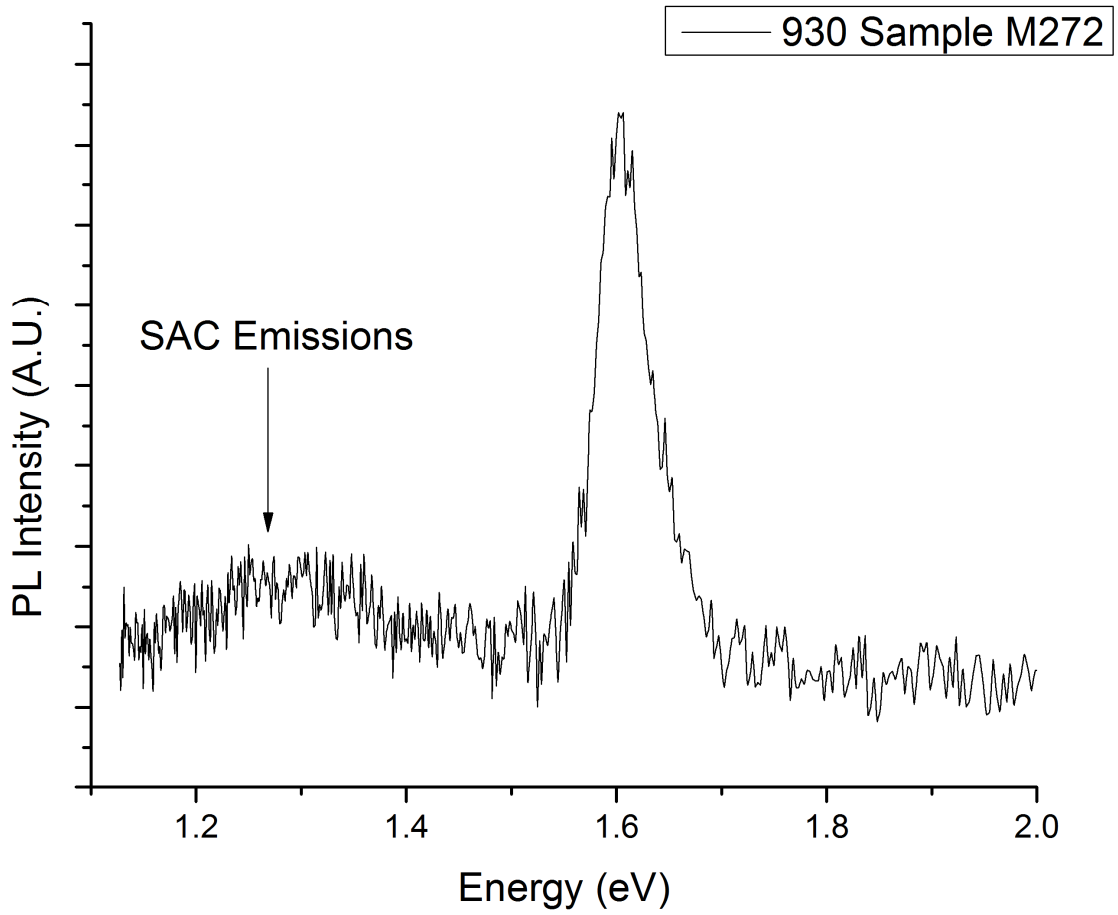

Figure 6.21 Sample M272 PL spectrum with low energy SAC emissions due to isolated traps caused by Si clustering along APD boundary.

A strong difference in the PL spectrum can be observed as the thick barrier composition is varied from $Al_{0.4}Ga_{0.6}As$ to $Al_{0.3}Ga_{0.7}As$. Two distinguishably large peaks emerge in the PL spectrum. Figure 6.19 shows the PL spectra of Samples M277 and M274 which are grown under similar growth conditions of the previous samples but have lower thick barrier heights (as the Al composition is much lower). In doing so, a lower energy peak arises with equal amplitude as the higher energy tailing peak due to the doping transitions. This implies that there are a large number of transitions take place at and below the band edge of the quantum well. Using peak analysis (Figures 6.23 and 6.24), it is determined that the lower energy peak is approximately equal to the energy gap

associated with GaAs interband transitions (~1.4-1.5 eV at room temperature). The PL peak parameters are given in Table 6.4.

Table 6.4 Sample Photoluminescence parameters with 30% Al composition.

	Position *(nm)*	**Height**	**Width (FWHM)**	**Area**
M277-1	792.6	153.2	22.06	3598
M277-2	846	196.8	60.86	12640
M274-1	861.9	68.35	38.95	2833
M274-2	907	76.33	45.89	3729

The change in energy at the conduction band edge in the well and at the thick barrier is approximately 0.033 eV. The Fermi energy lies 0.0426 eV above the quantum well band edge, meaning that it is slightly elevated beyond the thick barriers. This implies a large amount of electrons tunnel through the thin barriers and recombine in adjacent wells. There is still much to be understood about the contribution of carrier density to the trends observed in the PL spectra.

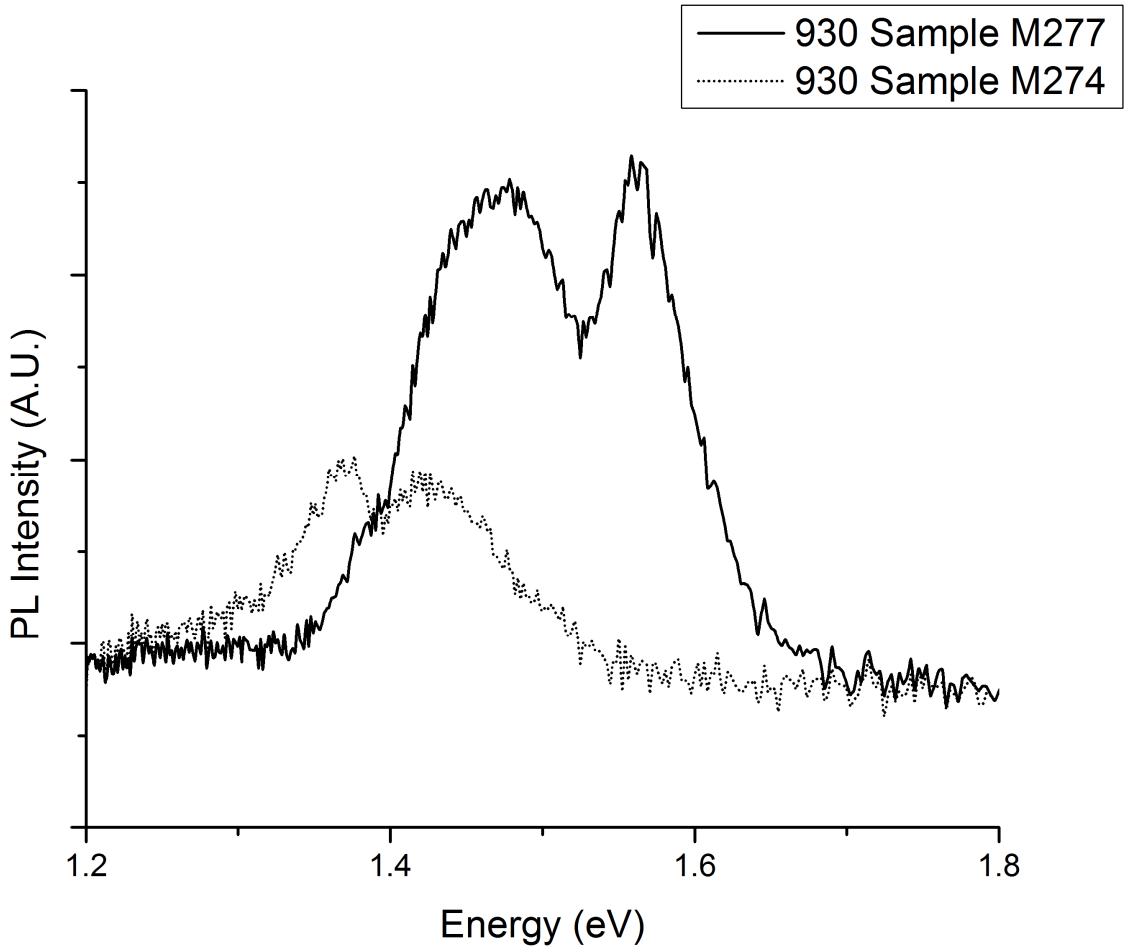

Figure 6.22 PL spectra of Samples M277 and M274. Two distinct peaks of equal amplitude emerge indicating large volume of transitions occur slightly above and below the band edge.

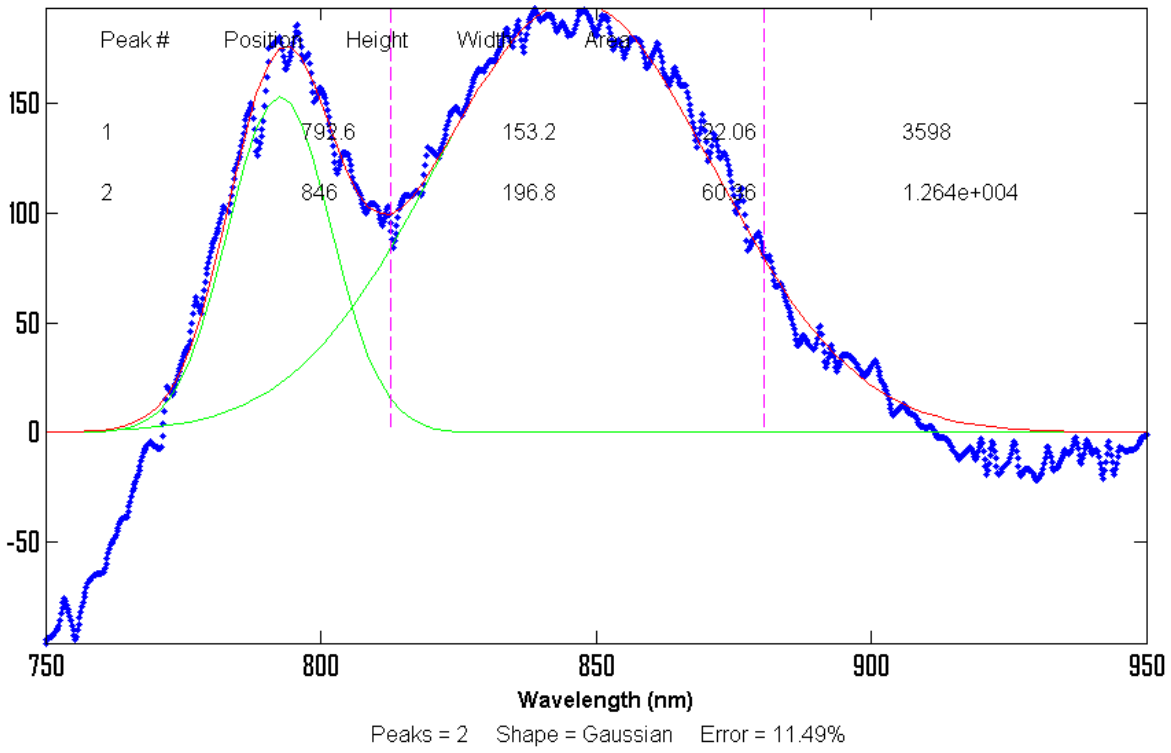

Figure 6.23 Peak analysis of Sample M277.

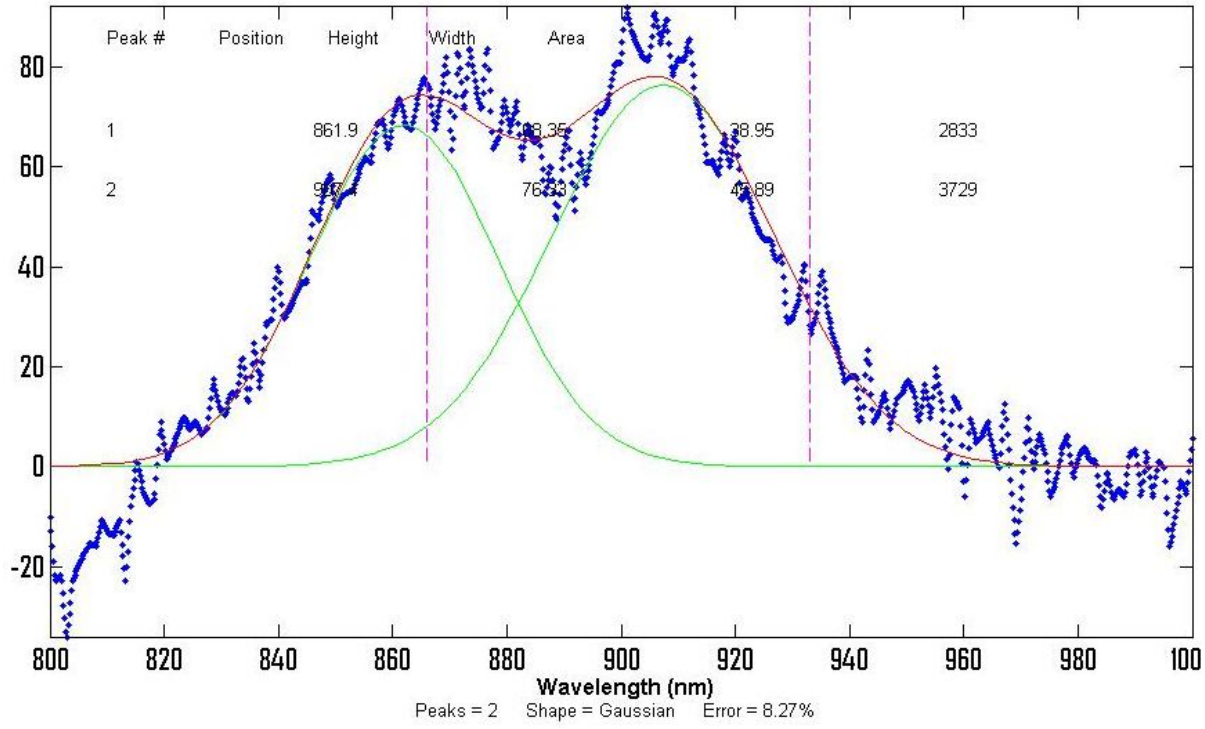

Figure 6.24 Peak analysis of Sample M274.

Figure 6.25 shows the energy band diagram for Samples M274 and M277. The E_2 wavefunction only exists in the thick barrier. This implies that electrons with an energy greater than that of E_1 have a high probability of tunneling through the AlAs barrier and into the thick barrier. The tunnel probability through the AlAs layer is effected by both the width of the GaAs well and the thick barrier height. A thick barrier Al composition of x = 30%-45% (Figure 6.26 and 6.27) shows greater confinement of the E_2 wavefunction for a given barrier height with increasing quantum well width..

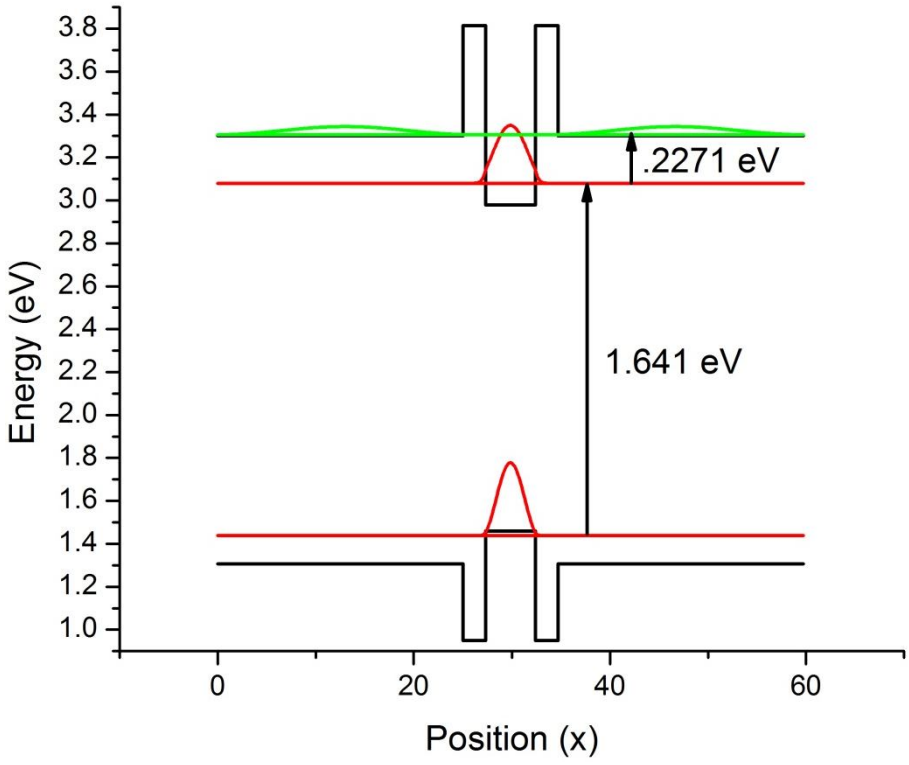

Figure 6.9 Energy band diagram of Samples M274 and M277. Direct gap transition corresponds to approximately 1.641 eV energy release (755 nm).

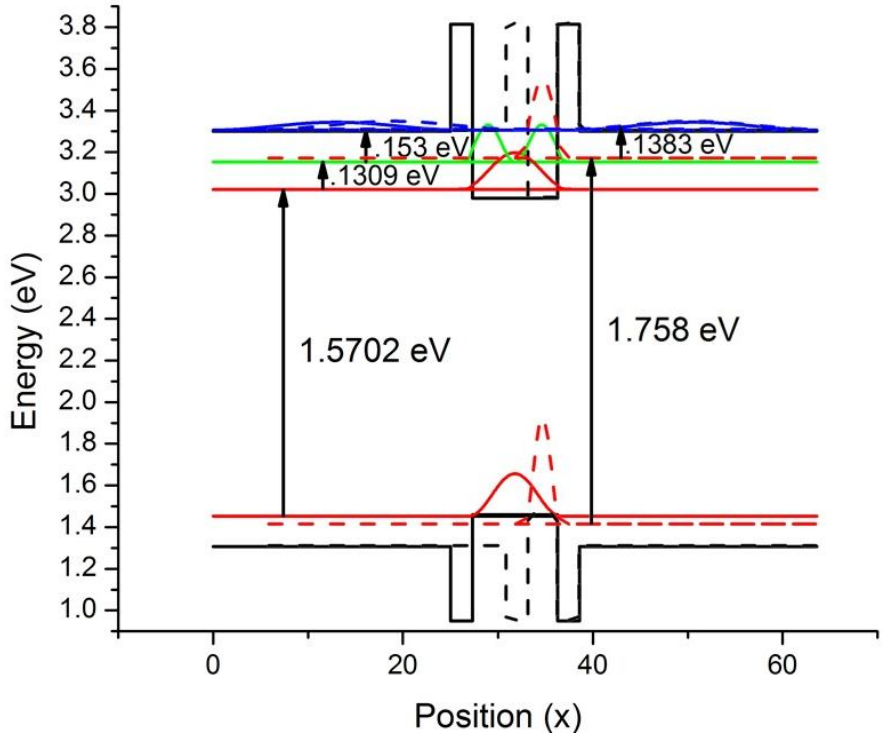

Figure 6.26 Energy band diagram of direct gap transition with increasing quantum well width (3.1 – 9 nm). The interband transition energy ranges from 1.5702 – 1.7579 eV (705.4 – 789.7 nm) for Al x = 30% barrier composition.

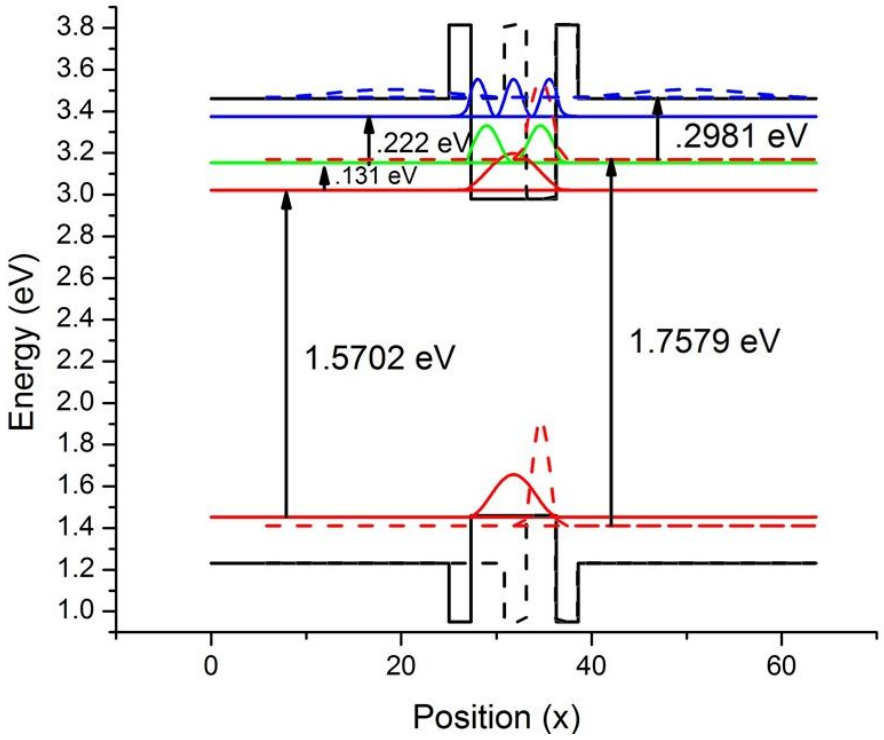

Figure 6.27 Energy band diagram of direct gap transition with increasing quantum well width (3.1 – 9 nm). The interband transition energy ranges from 1.5702 – 1.7579 eV (705.4 – 789.7 nm) for Al x = 45% barrier composition.

6.2.2 Reflectance Spectroscopy

Specular reflectance spectroscopy is the technique used to evaluate the reflective capabilities of the proposed DBR structure. Figure 6.21 shows the experimental setup constructed for reflectance measurements. Each sample's reflectance is measured in reference to a high reflectivity gold (Au) mirror. The resultant reflectance is the ratio of the sample reflectance to that of the gold reference mirror. This reflectance measurement is widely used to characterize the reflective capabilities of smooth, mirror-like surfaces as directional irradiance obeys the laws of reflection. For smooth surfaces, the reflected intensity closely resembles the incident intensity, therefore the reflectance ratio is relatively one for high reflective zones. Low reflectance intensities may indicate zones of heavy absorption/transmission or diffuse surface scattering caused from surface degradation in the growth process.

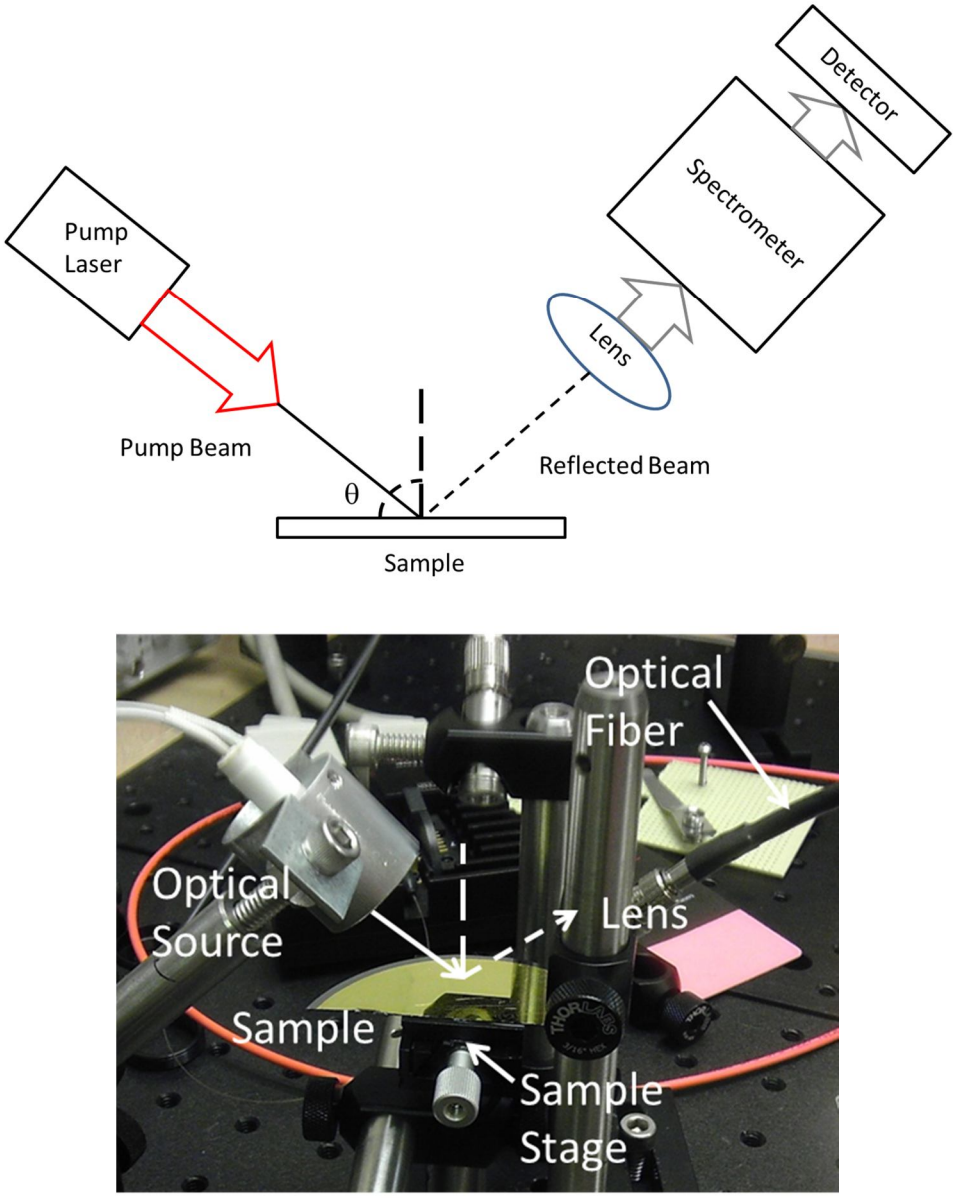

Figure 6.28 Schematic (top) and experimental setup (bottom) of specular reflectance characterization.

The reflectivity measurements reveal the devices capability to redirect incident irradiation. A DBR sample (M267) is characterized and the reflectivity spectrum is depicted in Figure 6.22. A substantial shifting of the high reflective zone occurs due to level of flux drift inherent to growth in the EPI 930 MBE chamber. Drifting in flux ratios occurs as the cell shutters open to release material into the growth chamber. Since the crucible containing the material is coned shaped, the flux of material entering the chamber gradually varies as the material depletes (as the cross sectional area of material decreases as it depletes). In the DBR growth process, drift causes a slight variance in the refractive index of the layer. The reflectivity of the DBR is directly correlated to the refractive index; therefore the gradient change in refractive index results in a sloping effect of the high reflective zone reflectivity spectrum (Figure 6.14). This effect becomes more drastic the longer the growth process. The level of this drift is very difficult to gauge *in situ* simply because the flux monitor mechanism within this MBE chamber cannot be lowered in to the correct position while a sample is in place. This adds another level of complexity to device construction.

Figure 6.23 shows the normalized high reflectivity zone of Sample M267 and the simulated reflectivity. The broadening of the high-reflectivity zone is apparent as well as a slight shift toward longer wavelengths. This shift attributed to the gradient change in material flux and the broadening of the high reflectivity zone is due to discrepancies in the layer thickness between repeated layers.

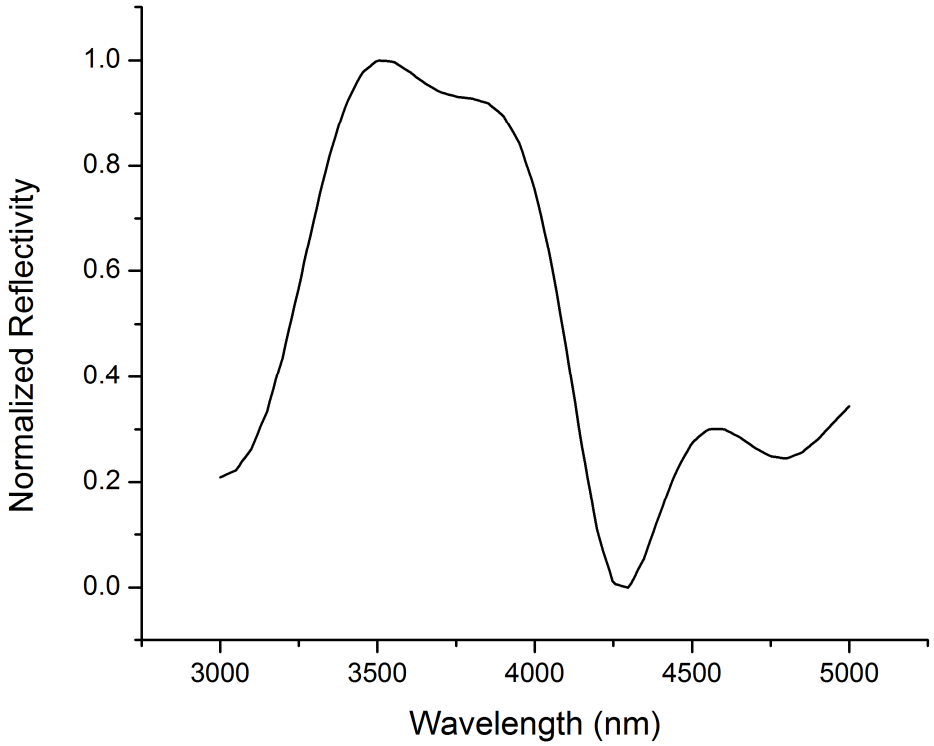

Figure 6.29 Reflectivity of Sample M2687 DBR with high reflectivity zone from 3.2-4.2 μm.

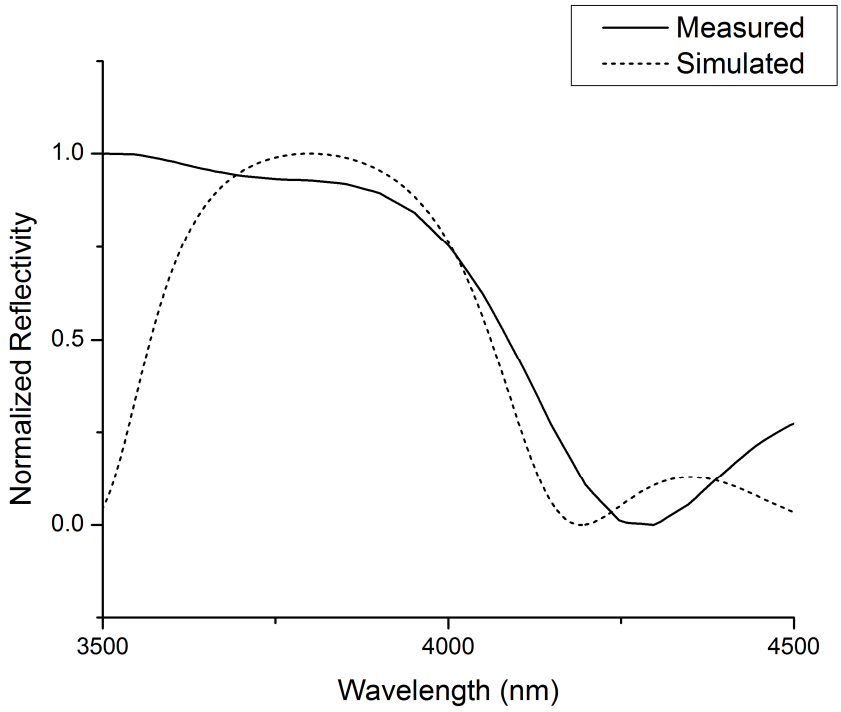

Figure 6.30 Normalized reflectivity of Sample M267 and simulated reflectivity.

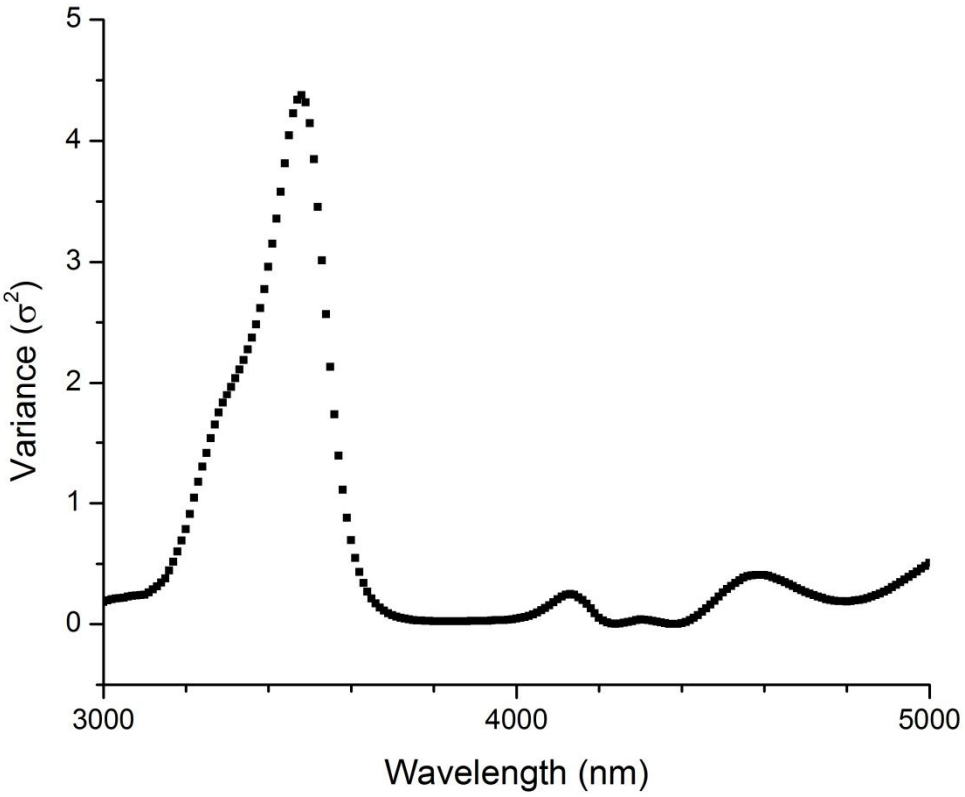

Figure 6.31 Residual plot of variance in relative reflectivity. The large peak marks the broadening of the high reflective zone.

Figure 6.24 depicts the variance in reflectivity between the measured and simulated spectra (residual). The large peak in variance is associated with the broadening that occurs of the high reflectivity zone of the DBR structure. This plot also depicts the regions of little and no variance between the simulated and the measured reflectivity spectra. Little variance occurs between the range of 3.7-4.4 μm (within the range of design) corresponding to a high level of correlation in the relative reflectivity between the measured and simulated values.

A significant shifting also occurs in the reflectivity spectrum of the DBR device. This shifting is associated with the slight change in layer to layer refractive index due to system drifting during MBE growth. To accurately determine the level of shifting that

occurs, the center of third order peak that arises due to odd numbered layer constructive interference fringes is measured with respect to the theoretical value. It is determined that the center wavelength of the DBR structure shifts approximately 60 nm ± 13.67 nm toward higher energies. The corresponding variance indicates the level of residual between the reflectivity spectra.

Each DBR structure is grown at growth temperatures 610 °C on GaAs (100) semi-insulative substrates. The substrate is mounted Molybdenum blocks by Indium, which causes an adhesive effect to the block through surface tension. Using this technique requires an even distribution of Indium on the back of the substrate to ensure uniform temperature distribution during growth. This method has proven more effective for growth of thick layers in the EPI Model 930 and is the method used to construct each DBR structure.

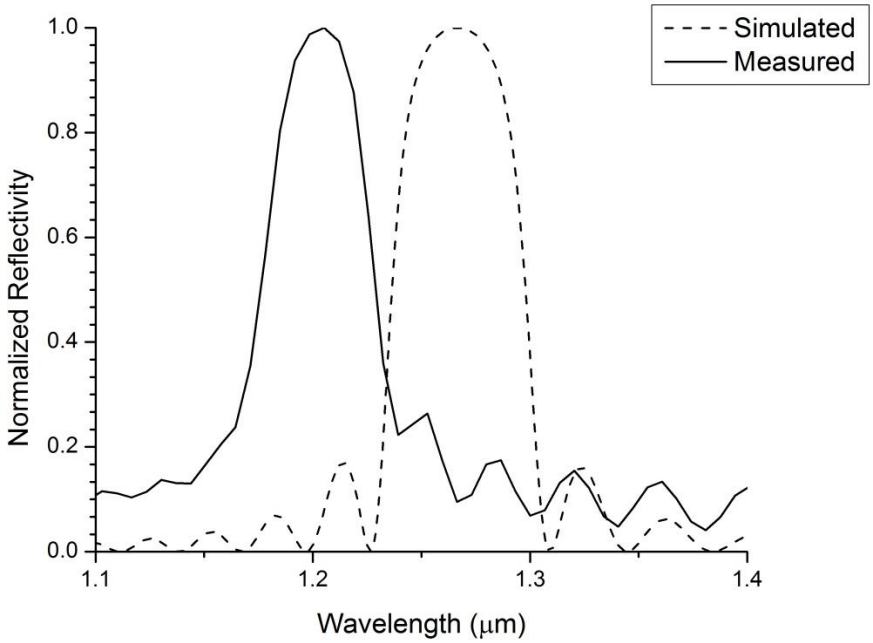

Figure 6.32 Shift in third order reflection peak used to determine the shift of center wavelength.

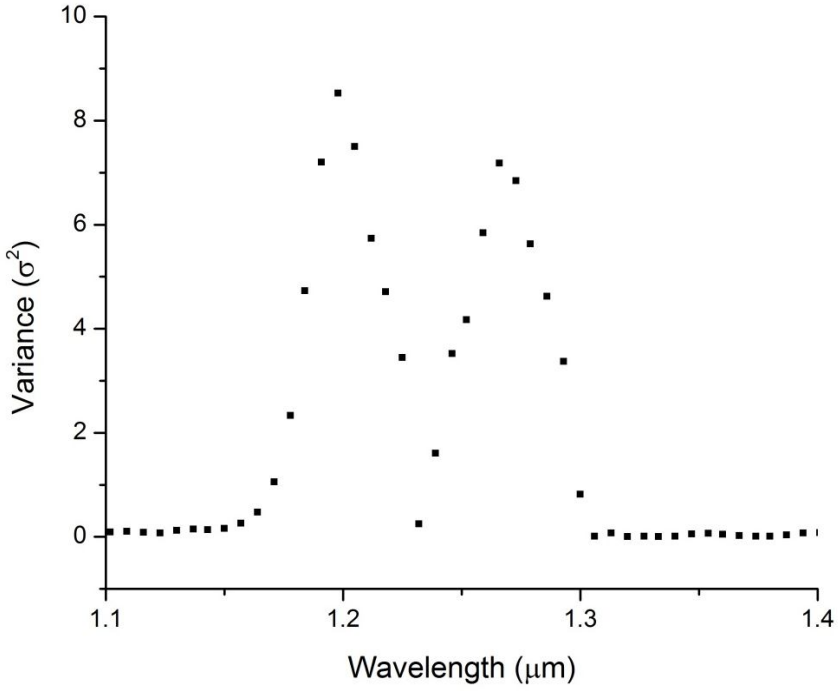

Figure 6.33 Residual plot of variance in third order reflection peak.

6.2.3 Absorption/Transmission Spectroscopy

The experimental absorption/transmission setup is depicted in Figure 6.19. This technique is a common optical characterization method to assess the ability of a device to absorb or permit optical energies. The physics of this optical process is as described in Chapter 2. Considering the experimental setup of Figure 6.3, infrared radiation is normally incident upon the quantum well sample causing a transfer of optical energy within the sample at room temperature.

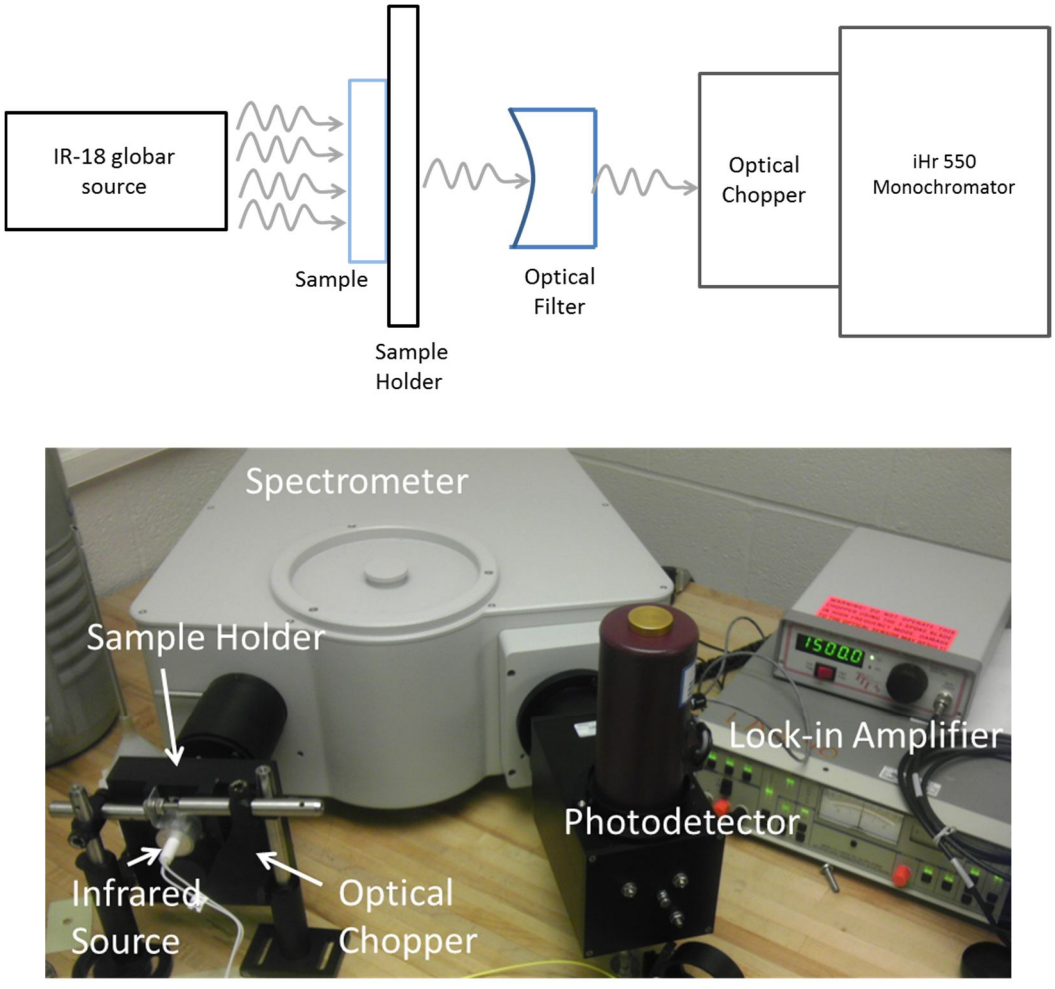

Figure 6.34 Schematic (top) and experimental setup (bottom) of absorption/transmission spectroscopy.

Energy that is not transferred (absorbed) within the quantum well is transmitted through the sample and captured by the photodetector. The change in intensity of the incident wave and the transmitted wave (as described by equation 2.3) denotes the level of optical absorption at the incident wavelength. The absorption spectrum of two quantum well samples is depicted in Figure 6.20.

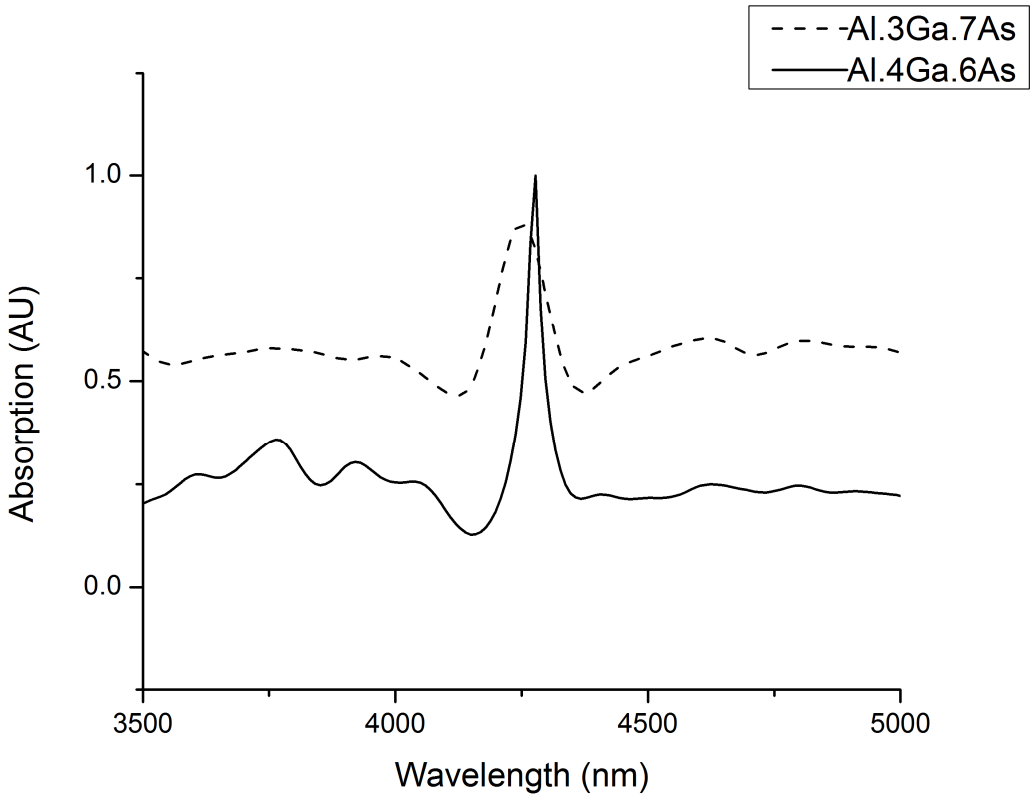

Figure 6.35 Absorption of $Al_{0.3}Ga_{0.7}As$ sample (dotted) and $Al_{0.4}Ga_{0.6}As$ sample (solid). Increasing the Al composition in each thick barrier layer, increase the intensity of absorption within the quantum well layers (slight red-shift is observed due to sample heating).

From the absorption spectra depicted in Figure 6.20, the dominate absorption wavelength of the quantum well region can be deduced. Thus, the absorptive behavior the structure can be analyzed and vetted against the specified design parameters. The samples characterize show distinct absorption peaks near 4200 nm (~4000 nm deduced

from simulation). A significant red shift occurs due to sample heating during measurements.

Theoretically, the absorption intensities are infinitely sharp at the correspondent transition energies, but as is apparent from the spectra in Figure 6.20, substantial broadening of the absorption peak occurs due to interatomic effects of the lattice system. The intermixing of transition energies from adjacent wells and unwanted transition states (due to layer traps and insufficient lifetimes) contribute to the broadening effect. This broadening may also highlight the nonuniformity of each successive well; as this study has affirmed the strong correlation between the well width and the intersubband spacing. This inhomogeneity in well widths is attributed to the variation in fluxes density inherent to MBE growth. Samples are consistently rotated (~6-9 rpm) during growth to compensate for this fluctuation, but cannot fully counteract radial variation from center of the wafer outward; contributing to angstrom variation between well structures. Though considerably minute, these variations in width are sufficient enough to effect energy separation and thus the absorption spectrum.

Figures 6.21, 6.22, and 6.23 show the resultant transmission spectrum for quantum well samples and the associated reference substrate. Each transmission measurement is averaged over three runs. The transmission spectra gives indication to the sample's reaction to incident mid-infrared energy.

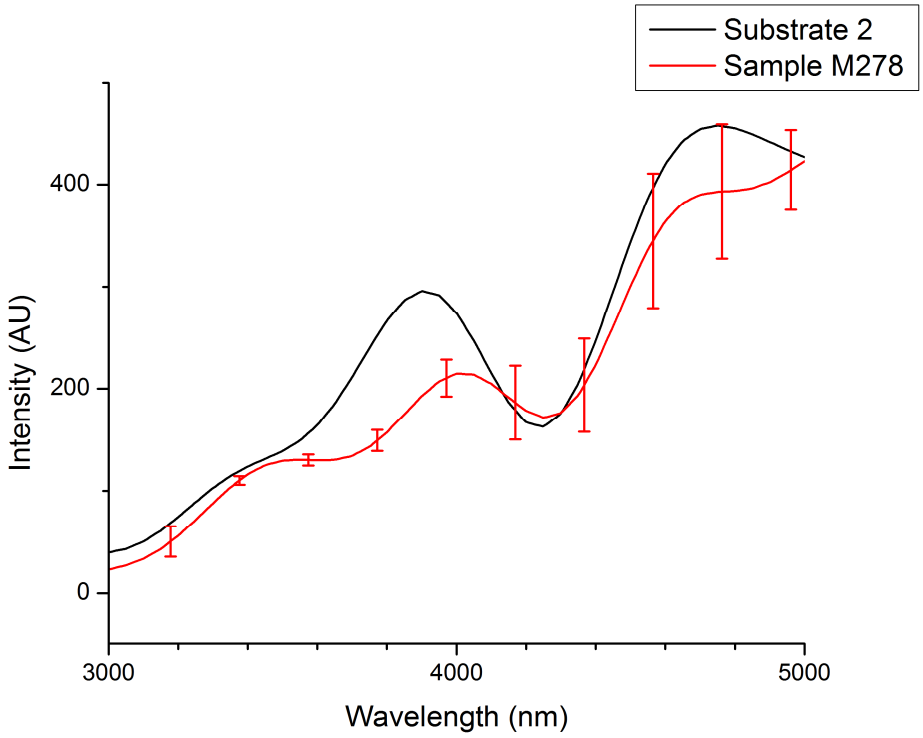

Figure 6.36 Transmission spectra of Sample M278 and reference substrate. The transmission spectrum of Sample M278 is averaged over three runs.

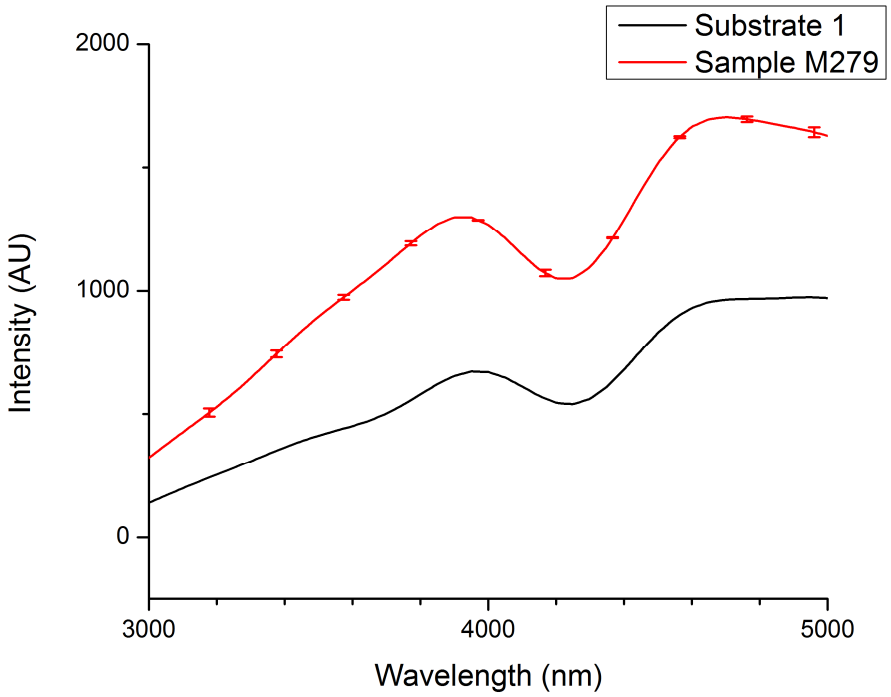

Figure 6.37 Transmission spectra of Sample M279 and reference substrate. The transmission spectrum of Sample M278 is averaged over three runs.

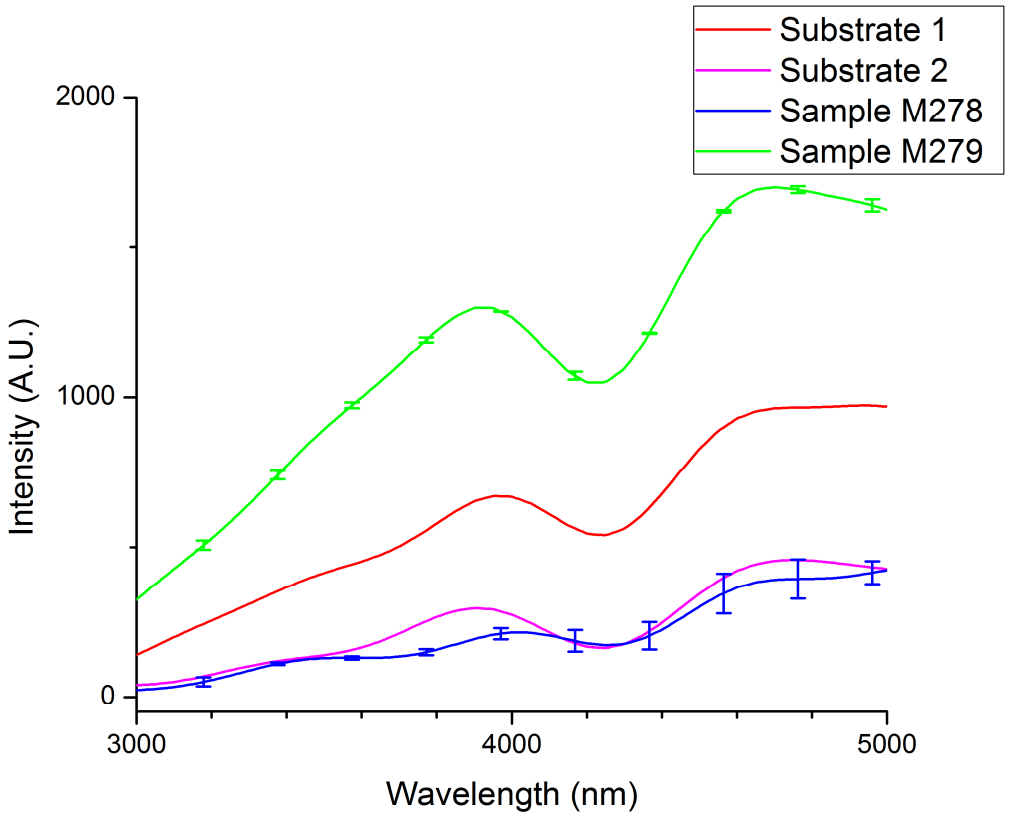

Figure 6.38 Relative intensities for transmission spectra for Samples M278 and M279 and reference substrates.

6.3 Electrical Characterization

Electrical characterization is employed to evaluate the active region's electrical performance. A potential bias is applied normal to the epitaxial layers to encourage electron current flow through the device. A globar emitter irradiates the device at infrared frequencies. With the applied bias, the absorption of the infrared photons promote additional ground state electrons to the conduction band current. The experimental electrical characterization setup is depicted by Figure 6.39.

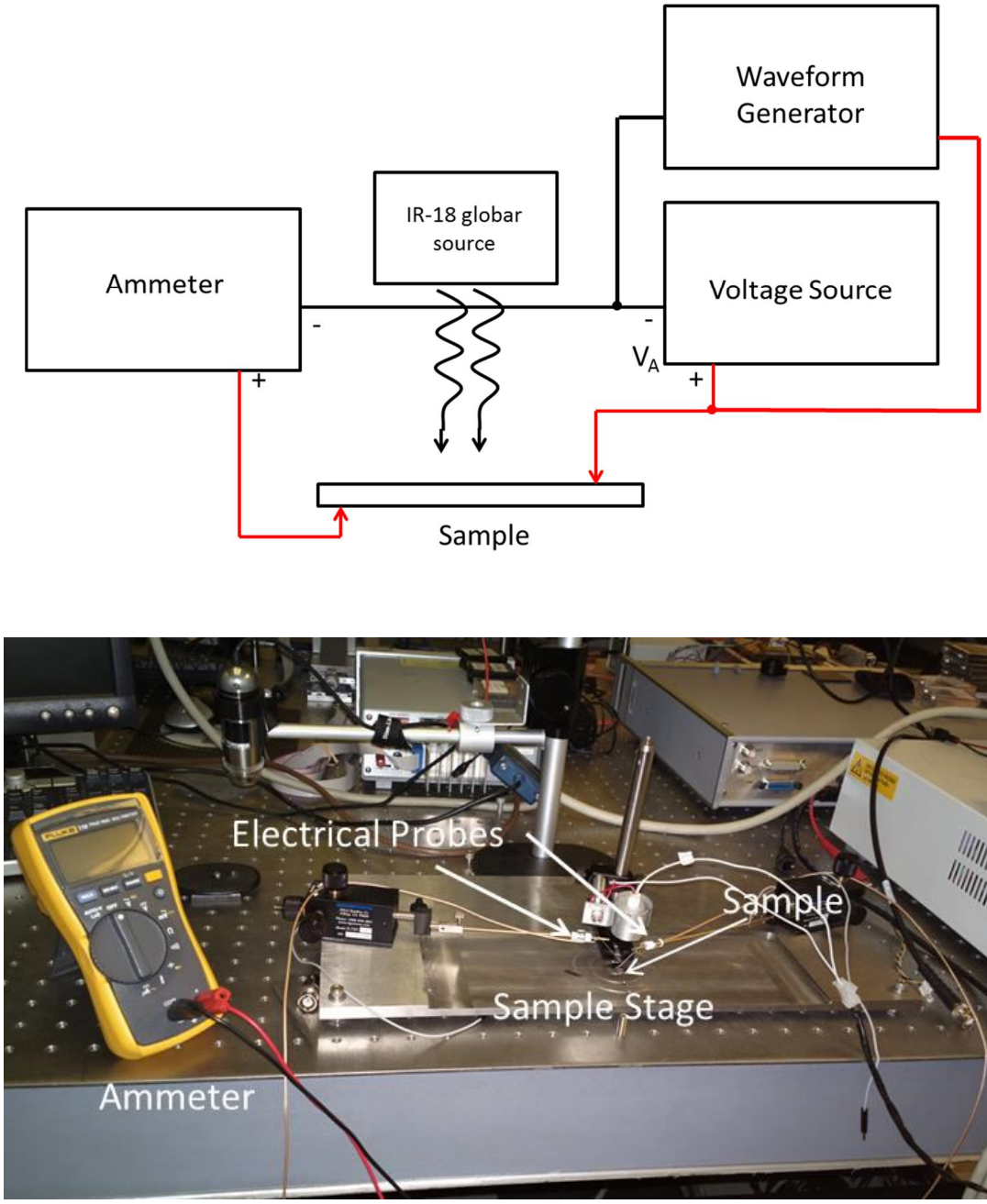

Figure 6.39 Schematic (top) and experimental photocurrent electrical characterization setup (bottom).

Figure 6.40, 6.41, and 6.42 show the noise current, current due to 6 V (~9 W) optical source, and 12 V (~20 W) optical source respectively. The current characteristics are evaluated from approximately -55 KV/cm to +55 KV/cm (or ±5 V external bias). The

current flow in the positive direction (+) direction is much more significant than that attributed to the opposite polarity. This is due impart to the large resistance of the substrate under external bias. Under sufficient reverse bias and electron injection current begins to flow in the opposite direction. This effect is negated by placing the bottom electrode directly beneath the modulator region.

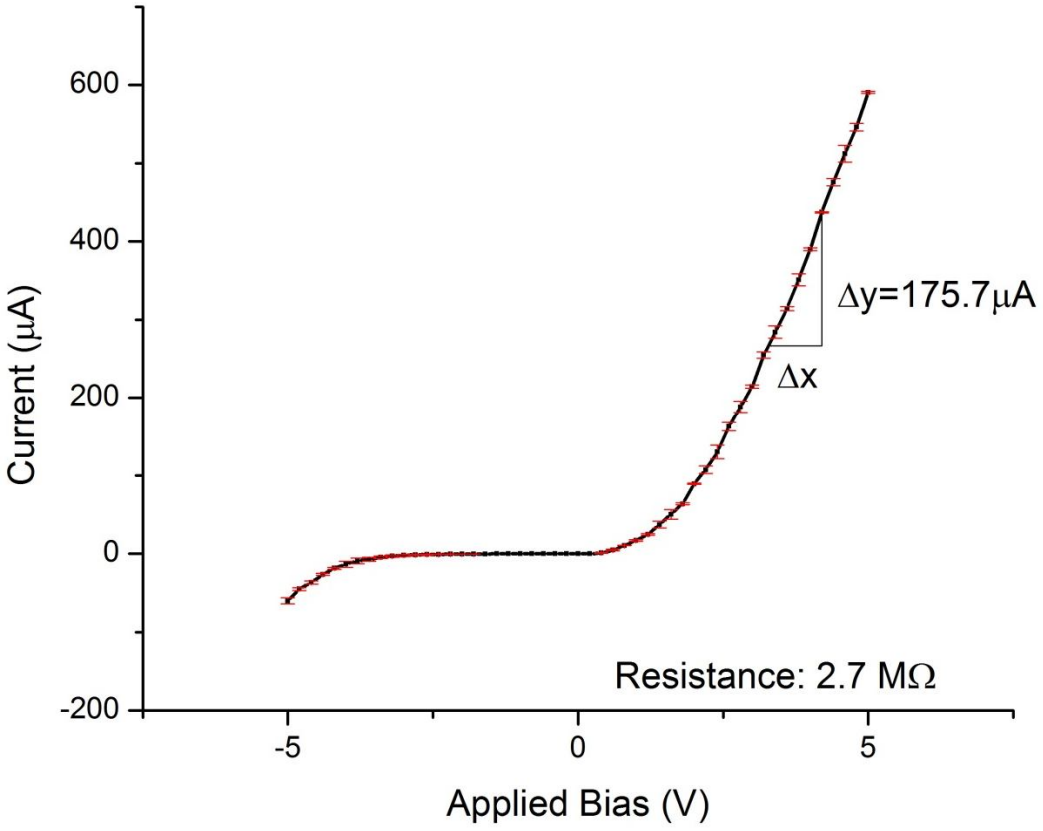

Figure 6.40 Noise current measurement sweep from -55KV/cm to +55KV/cm.

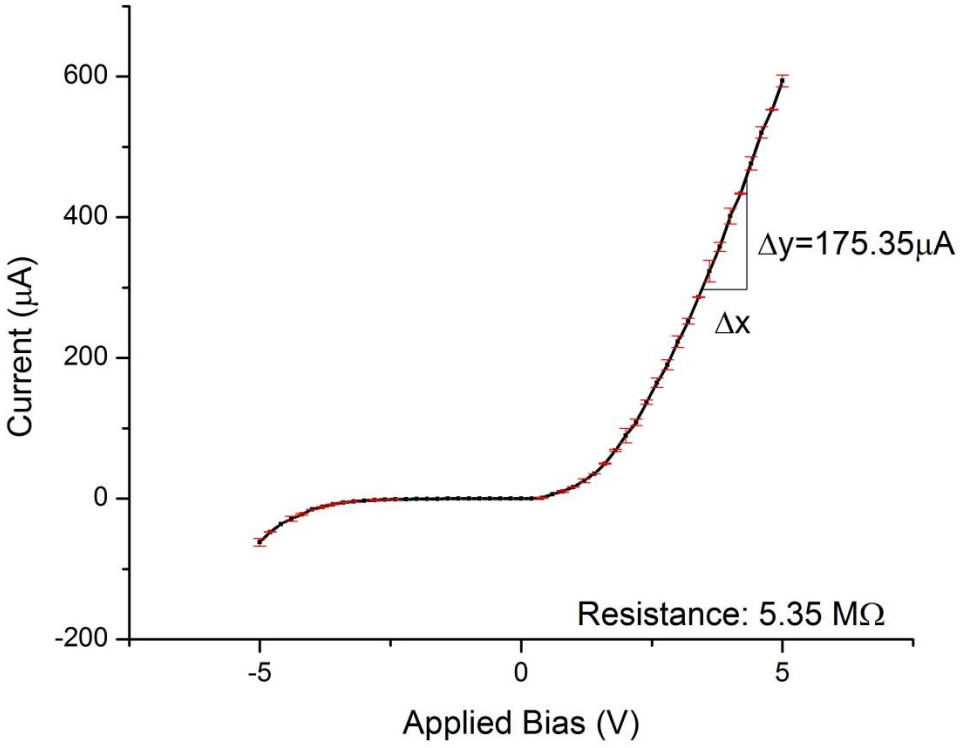

Figure 6.41 Current measurement due to 6V optical source irradiance swept from -55 KV/cm to +55 KV/cm.

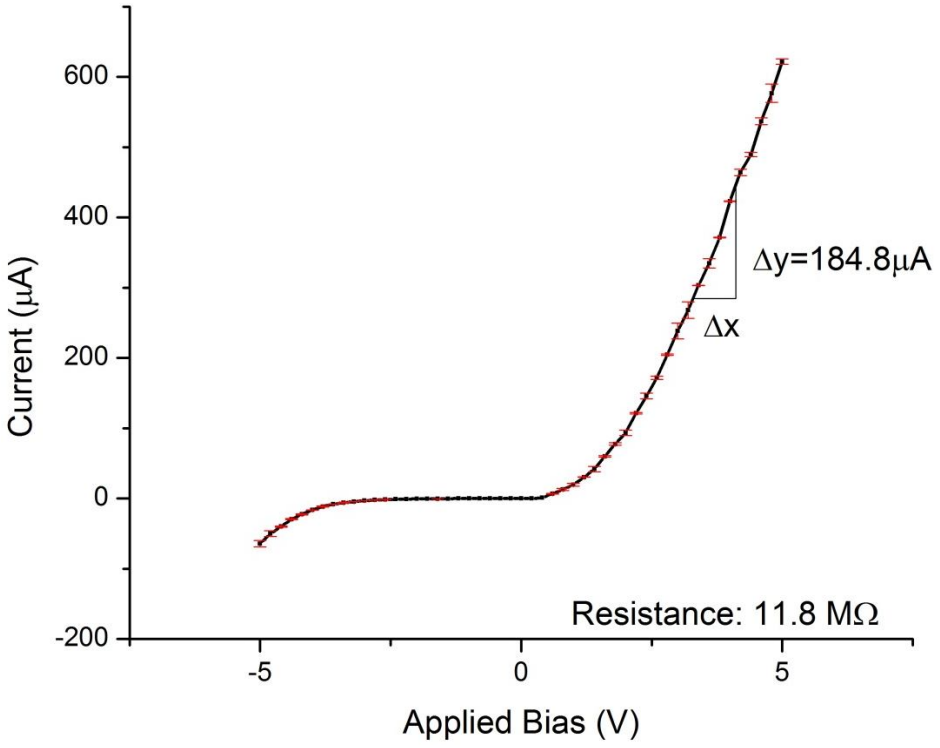

Figure 6.42 Current measurement due to 12V optical source irradiance swept from -55 KV/cm to +55 KV/cm.

Figure 6.43 shows the average photocurrent associated with positive external bias. Approximately 30 μA photocurrent is induced by 20 W (12 V maximum source) infrared radiation achieving a 6:1 current contrast ratio for 4V bias (~44 KV/cm). Under a 9 W optical power (6 V source), the photocurrent is much less stable and falls to noise current levels for certain bias conditions. This is most likely due to a threshold level condition satisfied by sufficient external bias and incident irradiation. Inasmuch, the contribution to photocurrent flow can be increased with the addition of subsequent wells, but conversely reduce device transparency. Figure 6.44 displays the photocurrent sweep from -55 KV/cm to +55 KV/cm. The change in photocurrent is also plotted with respect to varying source power for a 4 V applied external bias.

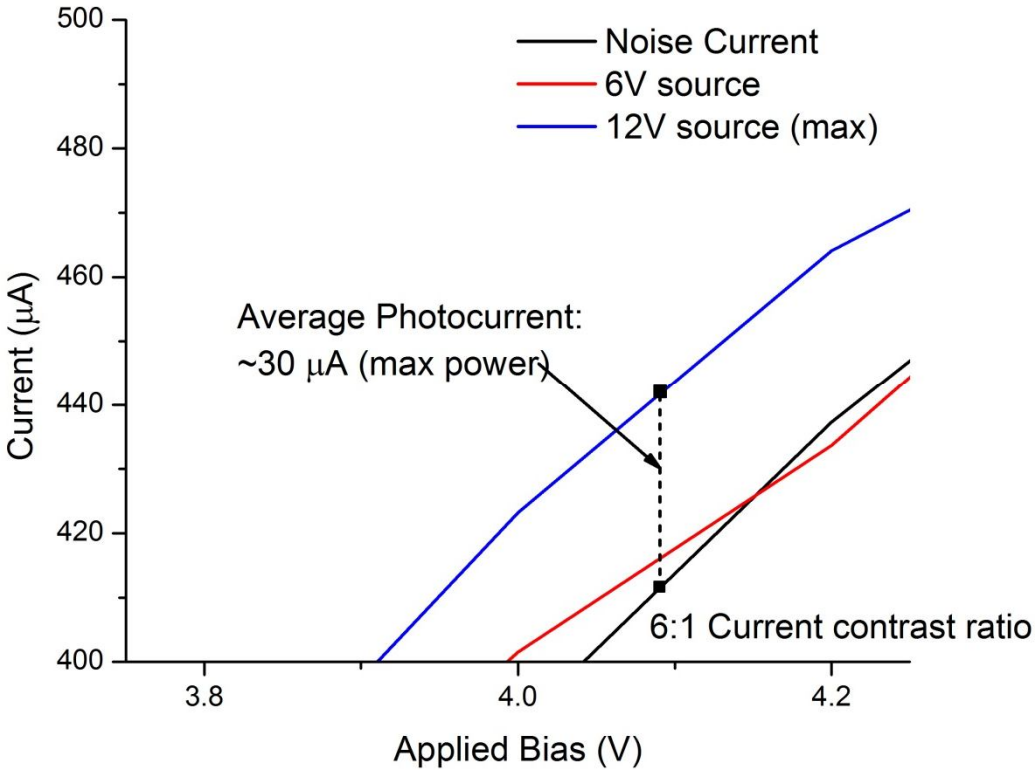

Figure 6.43 Average photocurrent measurement from 44 KV/cm to 46 KV/cm (approximately 30 μA) with 1.6:1 contrast ratio.

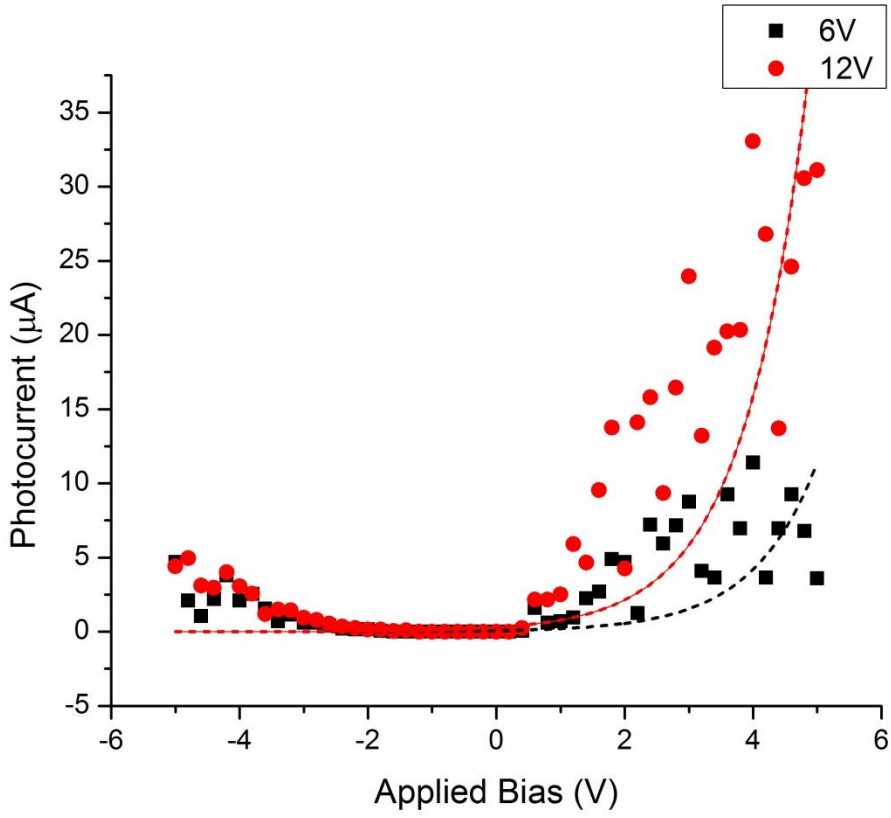

Figure 6.44 Average photocurrent measurement sweep from -55 KV/cm to +55 KV/cm at 6V and 12V (max) power.

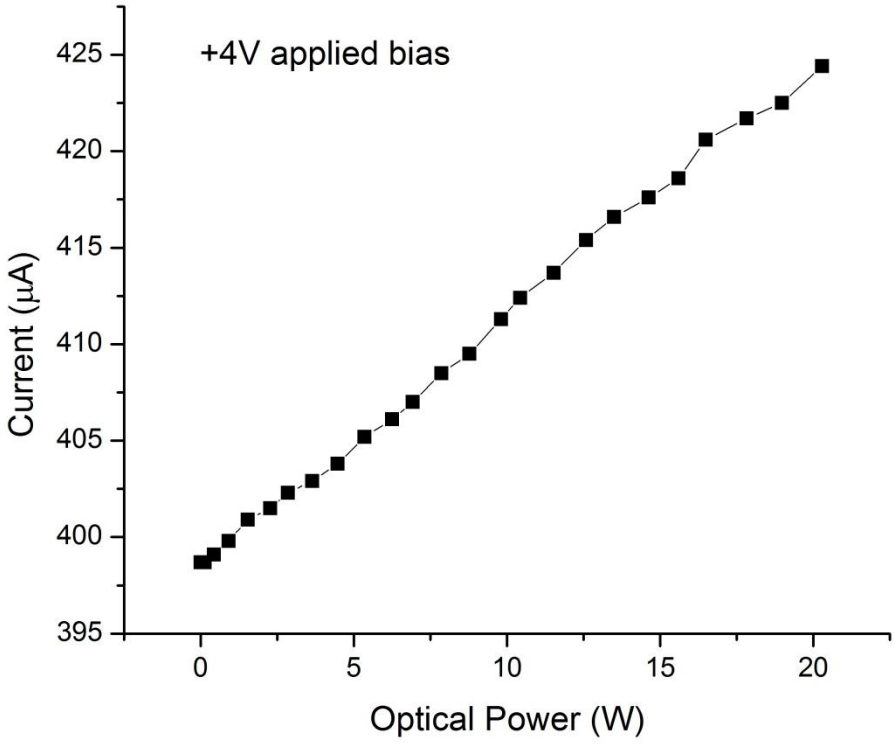

Figure 6.45 Average photocurrent as function of optical source power from 0 to 20 W (source) at 4 V applied bias.

The maximum achievable contrast ratio (I_{max}/I_{min}) for the device is 1.6:1. This contrast ratio is similar to the contrast ratios achieved for NRL fabricated modulators (ranging from 1.75:1 to 4:1 for applied voltages between 12 and 25 V dependent on structure) [13]. The contrast ratio of the structure influences the fundamental limit for the modulator region. Device size, electrode thickness, and inherent resistance-capacitance limits of the structure affect the contrast ratio and thus the switching speeds. Smaller devices reduce these effects but also reduce device aperture.

The switching capability of the device is also measured by applying a low frequency (1 KHz) and high frequency (1 MHz) rectangular pulse across the device active region. Two volts (2 V_{pp}) is supplied at 50% duty cycle via waveform generator. The modulation affect is then measured across the device electrodes. Figures 4.46 and 4.47 shows the output of low and high frequency modulation respectively. From Figure 4.46 it is apparent that the input modulation frequency produces very similar switching characteristics in the device. This is not necessarily the case at higher frequency (Figure 6.47). At higher frequencies the device is more susceptible to “ringing” noise at the rising and falling edge of the input signal due to the resistance to instantaneous change in conduction band current flow. The magnitude of this flicker is exaggerated at higher frequency, but can be reduced by lowering the current density or reducing the peak to peak bias. The role that well doping has on this effect is not quite understood. It is also noted that the RMS magnitude of the applied bias taken across the device is significantly reduced (by nearly half) due to the aforementioned anomaly. The relation between the reduction of switching contrast and input frequency is not fully understood.

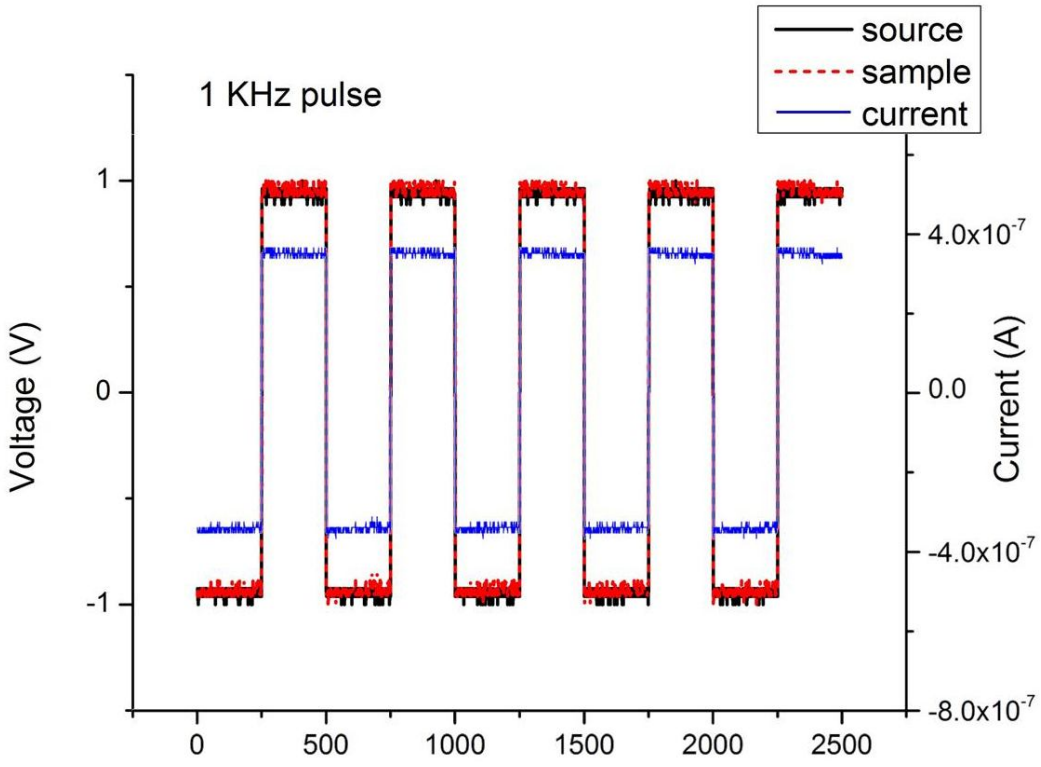

Figure 6.46 Low frequency (1 KHz) modulated input (source) and output (sample) show little distortion.

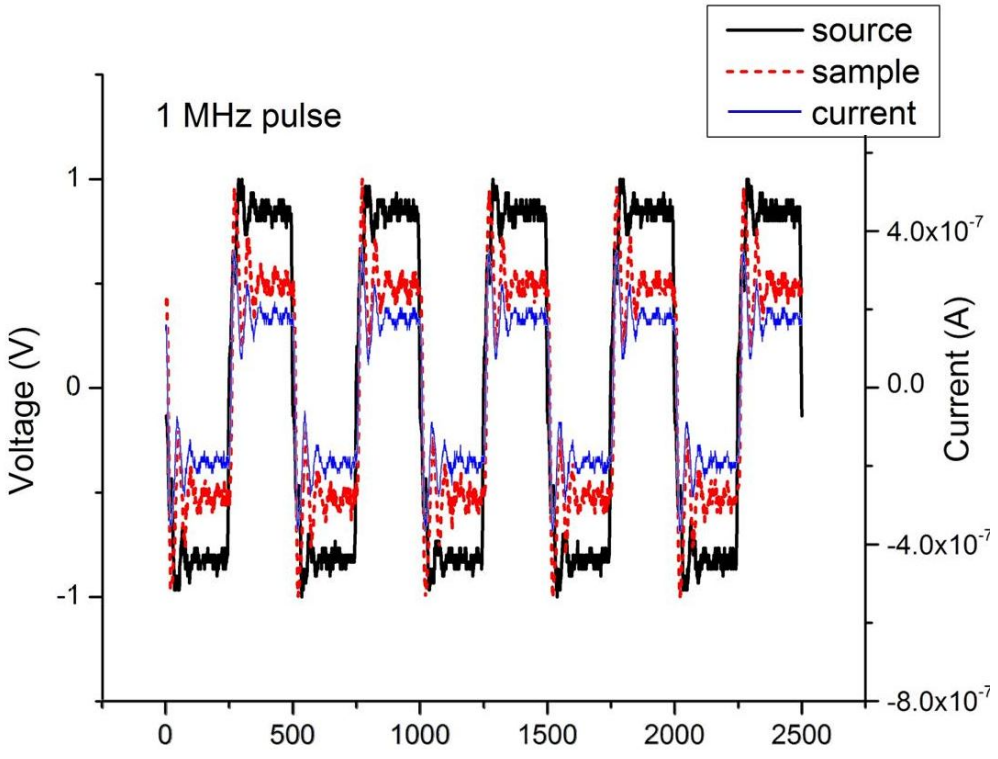

Figure 6.47 Higher frequency (1 MHz) modulated input (source) and output (sample) show shot noise distortion.

CHAPTER 7

SYNOPSIS

7.1 Distributed Bragg Reflector

The design of the mid-infrared distributed Bragg reflector region is construed from empirical values of the refractive indices of GaAs and AlAs (as proposed by Palmer [14]). A prior study was conducted to verify that the refractive indices of a GaAs/AlAs material system can be simplified as a constant value for the wavelength range considered (3-6 μm). With these constants in mind, a DBR region is designed for reflection at approximately 3.9 μm. To achieve the maximal reflectivity (>99%) for the DBR, it is calculated that a minimum of twenty-four alternated dielectric pairs are required. Beyond this number of repeated dielectric pairs in a GaAs/AlAs material system, the level of enhanced reflectivity becomes saturated (Figure 7.1). This curve gives a great deal of indication of the compromise between the desired reflectivity and the total thickness of the device. As the device thickness increases, as does the allotted growth time, which potentially leads to defective devices.

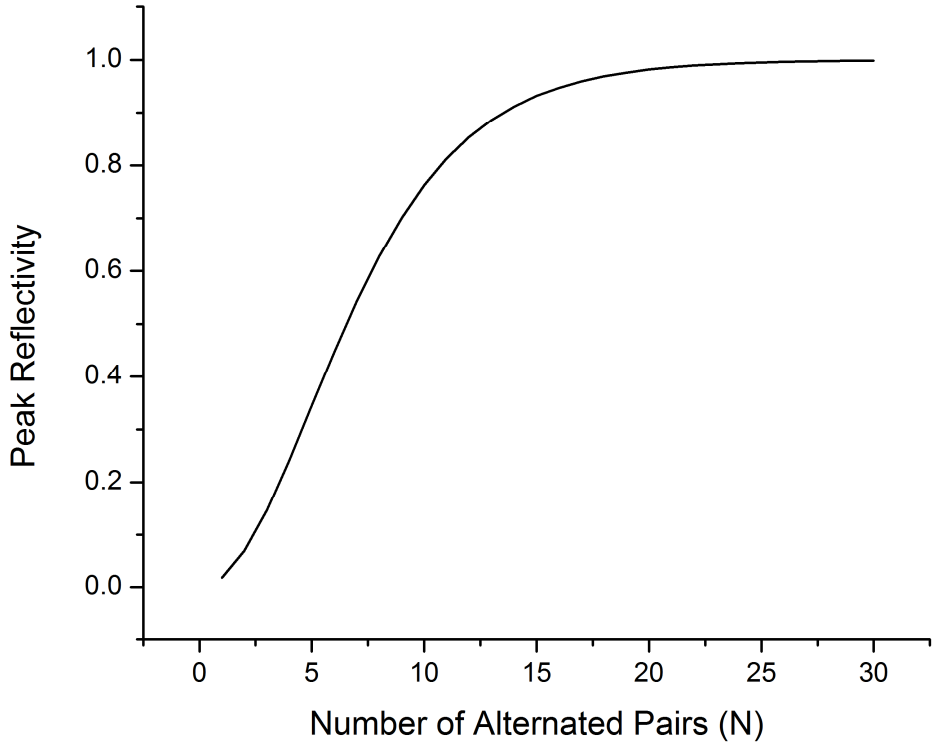

Figure 7.1 Plot of Peak Reflectivity vs. Number of Alternated dielectric pairs.

Growing twenty-four periods (forty-eight epitaxial layers) presents great difficulty at the growth level as long growth times imply substantial system drift which may lead to the degradation of quality of each subsequent layer. Since the thickness of each dielectric layer is directly proportional to the wavelength, the thickness of each layer increases with the operation wavelength of the device (Figure 7.2).

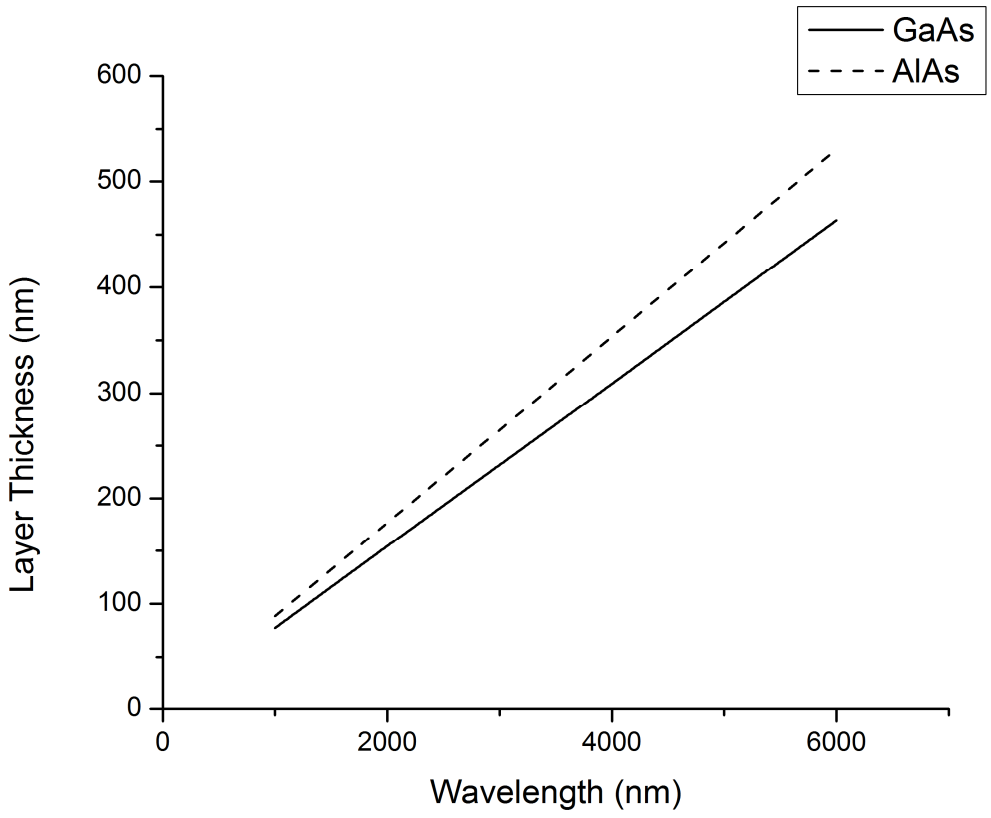

Figure 7.2 Plot of layer thickness for GaAs and AlAs layers for increasing operation wavelength. The empirical refractive index for each remain constant corresponding to 3.236 and 2.8283 for GaAs and AlAs respectively.

From the plot of Figure 7.2, a device designed for operation at 3.9 μm corresponds to a layer thickness of 299.3 and 342.61 for GaAs and AlAs respectively. Considering a device with a minimum of 24 periods (more than 16 μm thick), a minimum of ninety continuous hours are required to construct such a device using the MBE technique. Such a growth would lead to an incalculable level of drift and hence layer degradation of the structure. Therefore a compromise is made sacrificing the peak reflectivity of the device to decrease the growth duration and sample quality of the layers.

As the number of dielectric pairs is increased, a significant change in the reflective spectrum can be observed (Figure 7.3). The peak reflectivity increases as

expected, as well as a narrowing of the high reflective zone. It is also noted that the width of the high reflective zone also increases with increased center wavelength due to the increasing thickness of each layer (Figure 7.4). Furthermore, the peak reflectivity of the high reflectivity zone is slightly reduced for a given number of alternated pairs. This decay in peak reflectivity is associated with reduction in refractive indices for each material in this particular stratified system as the center wavelength shifts toward longer wavelengths. Figure 7.5 depicts the rate at which the decay of peak reflectivity occurs in GaAs/AlAs systems.

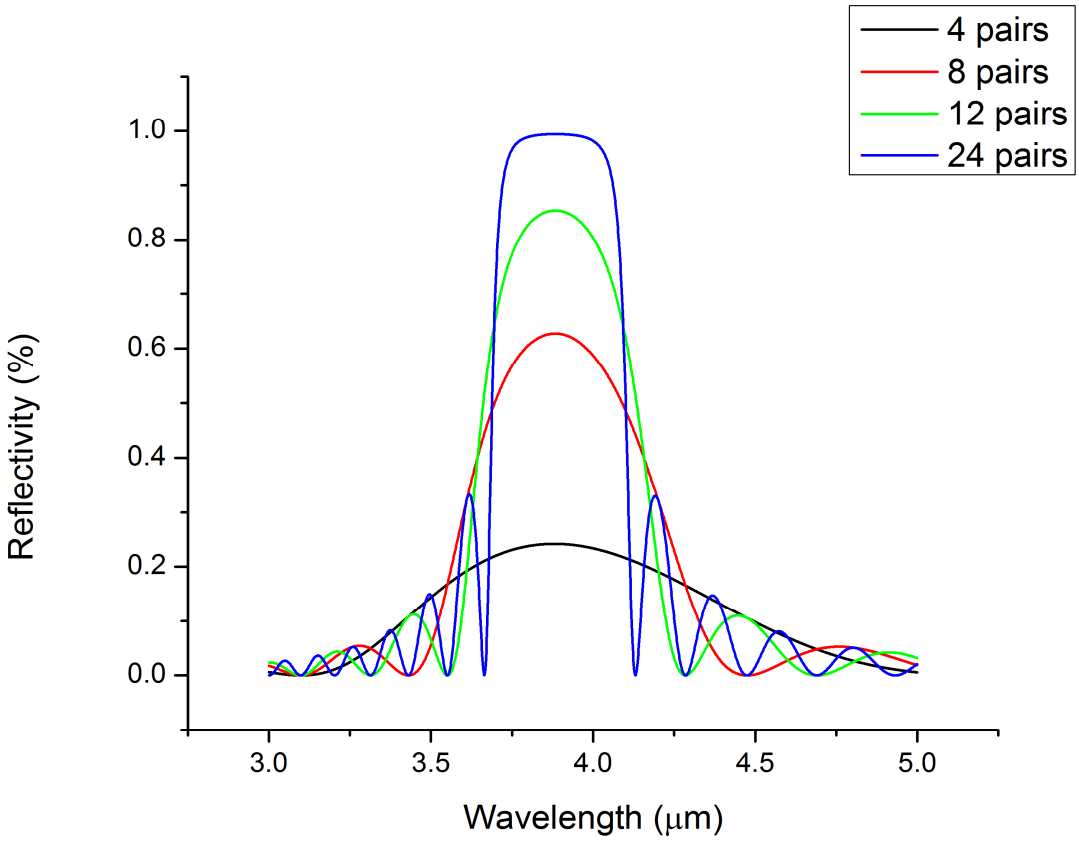

Figure 7.3 Reflectivity spectra for increasing number of dielectric pairs and design wavelength of approximately 3.9 μm.

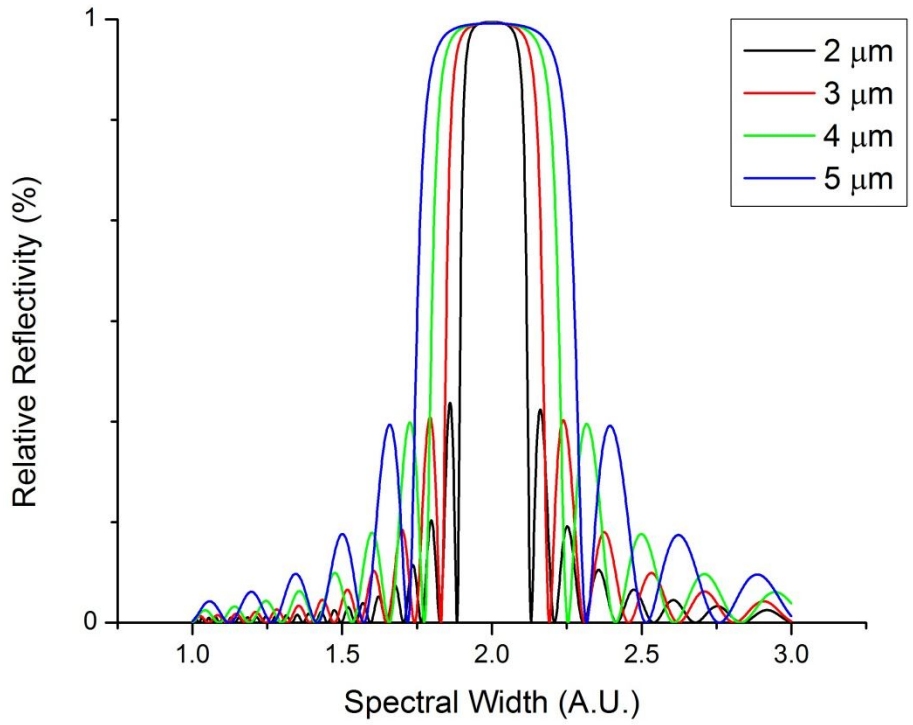

Figure 7.4 Change in spectral width of high reflective zone for 2, 3, 4, and 5 μm. Increasing center wavelength increases spectral width of high reflective zone.

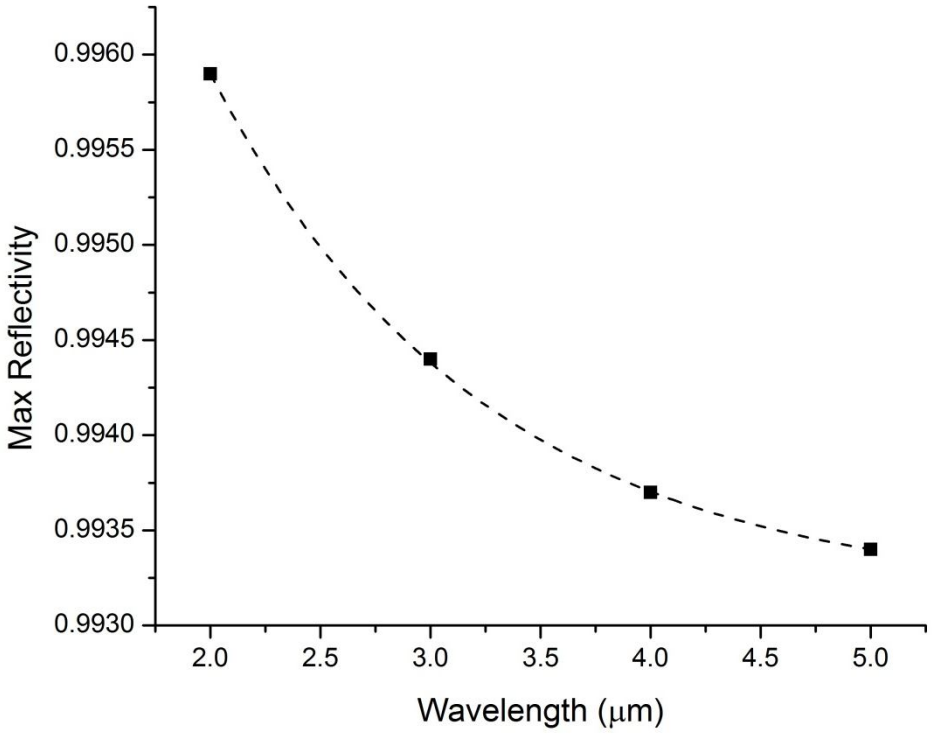

Figure 7.5 Change in peak reflectivity for 2-5 μm center wavelengths with constant number of repeated pairs (N=24).

7.2 Quantum Well Modulator

The design of the quantum well modulator region for 3-5 μm operation with the GaAs/AlAs material system is a very intricate process. A tunnel barrier quantum well structure (as proposed by Schneider et. al [18-19]) is considered to achieve such operation using the specified choice of materials. Extensive intersubband engineering is required in order to successfully achieve mid-infrared absorption. The optical properties of the quantum well structure can are altered by manipulating certain physical well parameters (i.e. well width, thick barrier height, tunnel barrier width). After a thorough investigation, it is determined that the for GaAs/AlAs material system a quantum well width of approximately 5 nm (17-18 ML) and tunnel barriers of approximately 2 nm (7-8 ML) encourage the desired intersubband transitions. Therefore, the variable parameter in this study is the thick barrier height (Figure 7.6).

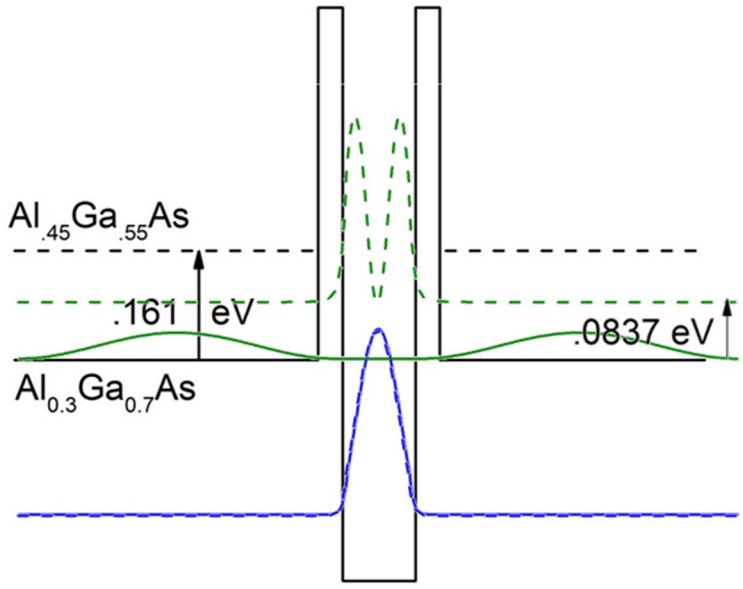

Figure 7.6 Shifting of intersubband spacing due to change in Al composition of thick barrier layers.

With a composition of $Al_{0.3}Ga_{0.7}As$, the thick barrier lies slightly below the E_2 discrete energy band, which invoke band to quasi-free transitions. The effective shifting the band edge in the $Al_xGa_{1-x}As$ layer by increasing the Al composition raises the band edge slightly above the second energy level. This forces the E_2 wave-function to be constrained within well layer. This change in Al composition yields a shift to higher energy of the E_2 wave-function increasing the E_{21} energy separation by approximately 84 meV.

Considering the material system configuration with $Al_{0.3}Ga_{0.7}As$ thick barrier layers, the second wave-function lies slightly above the band edge. This carrier distribution implies that photoexcited electrons, residing in the first subband, tunnel out of the well layer and into the thick barrier layer. Conversely, those free carriers then relax into the adjacent well layers through the same quasi-ballistic tunneling mechanism [51,52]. This phenomenon is characterized by high oscillator strengths and low dipole moments; which corresponds to the high probability of photoexcitation within the well layer. For this very reason, photoconductivity can be observed without external biasing. Gradually increasing the Al composition from 30% to 45% reduces the probability of tunneling out of the quantum well.

Though increasing the Al composition of the thick barrier regions may suggest a continuous migration of the E_2 wave-function into the quantum well, this is generally not the case. The manner in which the wave-function permeates the tunnel barriers occurs somewhat discretely as a threshold thick barrier composition is reached. This

phenomena is outlined by the stepwise behavior of the transition oscillator strength within the quantum well layer (Figure 7.5). This phenomenon can be best explained by the inelastic tunnel probability at GaAs/AlAs heterointerfaces [51-55].

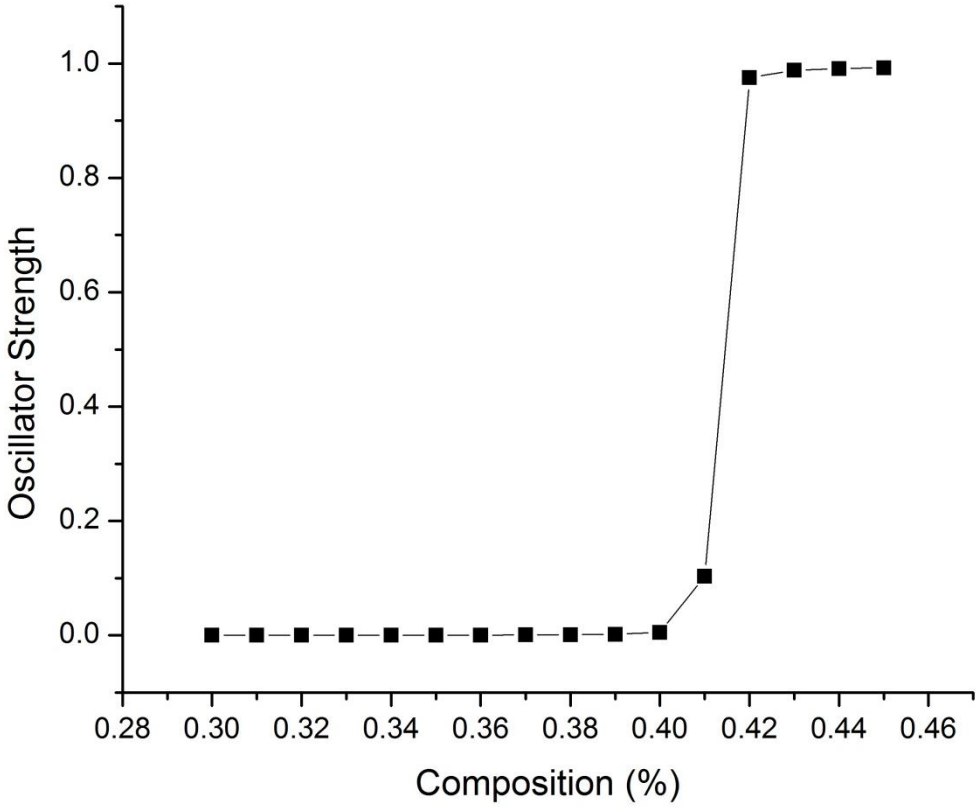

Figure 7.7 Instantaneous change in transition oscillator strength (resonance energy) with thick barrier Al composition variance.

A threshold condition occurs between 40-42% Al composition. At this composition point, the E_2 wave-function exists in both the quantum well and the thick barrier layers. This is marked by slightly higher transition oscillator strength within the quantum well. At this threshold point, excited conduction band electrons have an enhanced probability of recombining within the well layer; whereas lower compositions result in extremely high tunnel probability. The innate ability of this device design to induce a photocurrent

irrespectively, despite electronic biasing, is compensated as the E_2 wave function moves into the well due to the fact that the tunnel probability is greatly reduce at the inversion point (between 40-42% Al composition) and free electrons do not tunnel and recombine in subsequent wells.

REFERENCES

[51] Y. Fu, M. Willander, E. L. Ivchenko, and A. A. Kiselev, "Valley mixing in GaAs/AlAs multilayer structures in the effective mass method," *Phys. Rev.* B 47 (20). May 1993.

[52] R. Bonnefoi, D. H. Chow, T. C. McGill, R. D. Burnham, and F. A. Ponce, "Current transport mechanisms in GaAs/AlAs tunnel structures grown by metal-organic chemical vapor deposition," *J. Vac. Sci. Technol.* B 4 (4), Jul/Aug 1986.

[53] R.T Collins, J. Lambe, T. C. McGill, and R. D. Burnham, "Inelastic tunneling characteristics of AlAs/GaAs heterojunctions," *Appl. Phys. Lett.* 44 (5). 1 March 1984.

[54] R. Bonnefoi, R. T. Collins, T. C. McGill, R. D. Burnham, and F. A. Ponce, "Resonant tunneling in GaAs/AlAs heterostructures grown metal organic chemical vapor deposition," *Appl. Phys. Lett.* 46, 285 (1985).

[55] M. K. Hudait, P. Modak, S. Hardikar, and S. B. Krupahidhi, "Photoluminescence studies on Si-doped GaAs/Ge," *Journal of Applied Physics*. Vol. 83 (8). 15 April 1998.

CHAPTER 8

CONCLUSION

In this dissertation, a GaAs/AlAs mid-infrared reflective modulator is designed and its feasibility evaluated for free space optical implementation. Many design considerations must be taken into account in the development of such a device including the choice of growth material, achievable operation wavelength, and device size. The device itself consists of two subdevices: a quantum well modulator and reflective medium; each with its own design specifications. The reflective medium is designed to redirect incident radiation and is designed according to the absorption specifications of the quantum well modulator. In this work, the foundation for constructing such a device is formed.

An investigation of the explanatory parameters of both subdevices is explored in this work as well as overall device functionality. An in depth simulation analysis of physical parameters of both subdevices is presented as well as a complete optical device evaluation. Devices of similar material configuration have been proposed and evaluated for Free Space Optical applications in the near-infrared spectral range [5-14]. This work examines the feasibility as well as implementation of ideal theoretical approximations into a practical design of a device for mid-infrared FSO application and the design trade-offs encountered. The results of this work provide great potential for mid-infrared reflective modulators using GaAs/AlAs.

Practicality vs. Feasibility

One of the major difficulties of implementing such a device lies in its practical application. Due to the fact that the infrastructure backbone of the majority of FSO communication systems is implemented in the near-infrared spectral region, it will be difficult to readily employ such a device in modern FSO communication links. Though mid-infrared FSO communication shows great potential [1-5], it has not reached full technological maturity and not integrated in modern systems. There are apparent advantages of utilizing MIR frequencies as opposed to NIR in free space communications. The 3-5 (with transmissivity peaks at 3.8-4.1 μm) micron range is less vulnerable to atmospheric moisture, low-power, and has a potential to provide higher integrity transmissions for short to mid-range communications links. Yet these advantages may not yet prove worth the costs of production with GaAs/AlAs materials.

The use of GaAs/AlAs materials has proven effective for many optoelectronic device technologies due to their desirable optical properties. The use of GaAs/AlAs is not widely used for 3-5 micron devices, in particular traditional rectangular quantum well devices are unable to achieve the applicable transitions and a high refractive contrast is unattainable implying that many thick layers must be successfully constructed to achieve Bragg reflection. Therefore, the production of such a device can become very time consuming and expensive.

Closing Remarks

Many difficulties were encountered during the design, fabrication, and testing of this novel device. The primary goal of this study is to outline the necessary adaptations of a reflective modulator device for effective operation at mid-infrared communication wavelengths. Free space optics serves as a target application for which such a device is applicable and design constraints were chosen to adhere to specifications of similar FSO devices.

Future Works & Optimization

The concept of such a device has been applied to similar optoelectronic devices with great success. Yet, the adaptation of such a device for operation in the mid-infrared regime may propose new challenges. MIR wavelengths are associated with low power emissions and are generally considered undesirable for communication applications for this very reason. Though studies have shown promise in atmospheric transmissivity in this spectral range, technology has not yet reached full maturity to achieve great signal resolution with minimal signal to noise ratios (SNR). The physical parameter is most readily influenced by the device size.

Increasing the surface area feature size of the device directly increases the aperture allowing larger irradiance upon the sample. In doing so, the RC time constant increases due to the increase of surface area and capacitance associated with each epitaxial interface and contact region. Thus, presenting a trade-off on device speed and signal resolution. A comprehensive study considering the effects of feature size to more

accurately assess the functional performance of the device would prove very substantial. Inasmuch, due to low intensities associated with MIR emission, optical signals are highly susceptible to thermal noise introduced by the ambiance as well as the device itself. Therefore, substantial cooling methods must be employed during operation to ensure the device maintains thermal equilibrium. Inasmuch, the devices in this dissertation consider multiple quantum well structures separated by approximately 250 Å to ensure no overlap of adjacent quantum well wave-functions occur. Theoretically, reducing the thickness of the large barrier region will in fact increase the penetration depth of incident radiation into the multiple quantum well region for enhanced absorption characteristics. This feature will also be exploited by increasing the number of cascading wells. Conversely, increasing the overall thickness off the MQW region, though enhancing absorptive capability, will reduce the reflective capability of the subsequent reflective optic; the extent of which is unknown. Future studies will take into account the adverse effects of thermal noise on mid-infrared modulating reflectors and its direct impedance on device performance as well as the effect of physical device size and adjacent well spacing.

BIBLIOGRAPHY

[1] S. Ikpe, “Atmospheric Effects on Near-Infrared Free Space Optical Communication Links,” 2009.

[2] S. Bloom, E. Korevaar, J. Schuster, H. Willebrand, “Understanding the performance of free-space optics,” June 2003.

[3] C. P. Colvero, M. C.. R. Cordeiro, J. P. von der Weid, “Real time measurements of visibility and transmission in far-, mid- and near-IR free space optical links,” *Elec. Letters* 41 (10). 2005.

[4] P. Corrigan, R. Martini, E. A. Whittaker, and C. Bethea, “Mid-Infrared Lasers and the Kruse-Mie Theorem in Fog for Free-Space Optical Communication Applications,” *Optical Society of America*, 2008.

[5] R. Martini, et. al., “Free-Space Optical Transmission of Multimedia Satellite Data Streams Using Mid-Infrared Quantum Cascade Laser,” *Electronics Letters* vol. 38, iss. 4, pp.181-183, 2002.

[6] W. S. Rabinovich, P. G. Goetz, R. Mahon, E. Waluscka, D. S. Katzer, S. C. Binari, M. L. Biermann, and G. C. Gilbreath, “Cat’s eye quantum well modulating retro-reflectors for free-space optical communications,” 2003.

[7] Rabinovich, W.S.; Gilbreath, G.C.; Mahon, R.; Burris, R.; Goetz, P.G.; Moore, C.I.; Ferraro-Stell, M.; Witkowsky, J.L.; Swingen, L.; Oh, E.; Koplow, J.; Stievator, T.H.; , "Free-space optical communication link at 1550 nm using multiple quantum well modulating retro-reflectors over a 1-kilometer range," *Lasers and Electro-Optics,* 2003.

[8] W.S. Rabinovich; R. Mahon; P.G. Goetz; E. Waluschka; D.S. Katzer; S.C. Binari; G.C. Gilbreath; , "A cat's eye multiple quantum-well modulating retro-reflector," *Photonics Technology Letters, IEEE* , vol.15, no.3, pp.461-463, March 2003.

[9] Gilbreath, C. G. ;Bowman, S. R.; Rabinovich, W. S.; Merk, C. H.; Senasack H. E.;, 2000. “Modulating retroreflector using multiple quantum well technology,” United State. “*The United States of America as represented by the Secretary of the Navy* “ (Washington, DC) 6154299
URL: http://www.freepatentsonline.com/6154299.html

[10] T.H. Stievater; W.S. Rabinovich; P.G. Goetz; R. Mahon; S.C. Binari; , "A surface-normal coupled-quantum-well modulator at 1.55 µm," *Photonics Technology Letters, IEEE* , vol.16, no.9, pp.2036-2038, Sept. 2004.

[11] Richard, H. L., “The Atmospheric Transmission of Infrared Radiation from 2-5 microns for slant paths from 35,000 feet to the Upper Limit of the

Atmosphere, A Survey," *National Aeronautics and Space Administration*, Washington, D.C., June 1967.

[12] G. C. Gilbreath, W. S. Rabinovich, C. I. Moore, H. R. Burris, R. Mahon, K. J. Grant, P. G. Goetz, J. L. Murphy, M. R. Suite, M. F. Stell, M. L. Swingen, L. M. Wasiczko, S. R. Restaino, C. Wilcox, J. R. Andrews, and W. J. Scharpf, "Progress in Laser Propagation in Maritime Environment at the Naval Research Laboratory," *Free-Space Laser Communications V*, Proc. Of SPIE vol. 5892, 2005.

[13] G. C. Gilbreath, W. S. Rabinovich, T. J. Meehan, M. J. Vilcheck, R. Mahon, R. Burris, M. Ferraro, I. Sokolsky, J. A. Vasquez, C.. S. Bovais, K. Cochrell, K. C. Goins, R. Barbehenn, D. S. Katzer, K. Ikossi-Anatasiou, M. J. Montes, "Large-aperture multiple quantum well modulating retroreflector for free-space optical data transfer on unmanned aerial vehicles," *Society of Photo-Optical Instrumentation Engineers* 2001.

[14] E. Korevaar, I. Kim, B. McArthur, "Debunking the recurring myth of a magic wavelength for free-space optics," Proceedings: SPIE 4873, 155. 2002.

[15] C. M. Herzinger, P. D. Swanson, T. K. Tang, T. M. Cockerill, L. M. Miller, M. E. Givens, T.A. DeTemple, J. J. Coleman, and J. P. Leburton, "Electroabsorption properties of a single GaAs quantum well" *Phys. Rev.* B 44 (24). 15, December 1991.

[16] S. L. Chuang, S. Schmitt-Rink, D. A. B. Miller and D. S. Chemla, "Exciton Green's-function approach to optical absorption in a quantum well with an applied electric field," *Phys. Rev.* B *43 (2).* 15, January 1991.

[17] M. O. Manasreh, *Semiconductor Quantum Wells and Superlattices for Long-Wavelength Infrared Detectors*, Artech House, Inc. 1993.

[18] H. Schneider, P. Koldi, F. Fuchs, B. Dischler, K. Schwarz, and J. D. Ralston, "Photovoltaic intersubband detectors for 3-5 μm using GaAs quantum wells sandwiched between AlAs tunnel barriers," *Semicond. Sci. Technol.* 6. C120-C123. 1991.

[19] H. Schneider, F. Fuchs, B. Dischler, J. D. Ralston, and P. Koidl, "Intersubband absorption and infrared photodetection at 3.5 and 4.2 μm in GaAs quantum wells," *Appl. Phys. Lett.* 58 (20). 20, May 1991.

[20] D. S. Chemla, T. C. Damen, and D. A. B. Miller, "Electroabsorption by Stark effect on room-temperature excitons in GaAs/GaAlAs multiple quantum well structures," *Appl. Phys. Lett.* 42 (10), 15 May 1983.

[21] D. A. B. Miller and D. S. Chemla, "Relation between electroabsorption in bulk semiconductors and in quantum wells: The quantum confined Franz-Keldysh effect," *Phys. Rev.* B 33*,* pp.6976-6982, 1986.

[22] A. Harwit and J. S. Harris, “Observation of Stark shifts in quantum well intersubband transitions,” *Appl. Phys. Lett. 50, 685.* 1987.

[23] D. A. B. Miller, D. S. Chemla, T. C. Damen, A. C. Gossard, W. Wiegmann, T. H. Wood and C. A. Burrus, “Band-Edge Electroabsorption in Quantum Well Structures: The Quantum-Confined Stark Effect,” *Phys. Rev. Lett. Vol. 53, 22.* 26, November 1984.

[24] A. Krier, “Mid-infrared Semiconductor Optoelectronics,” Springer-Verlag London Limited, 2006.

[25] M. H. MacDougal, H. Zhao, P. D. Dapkus, M. Ziari, W. H. Steier, “Wide-bandwidth distributed Bragg reflectors using oxide/GaAS multilayers,” *Electronics Letters,* vol. 30, no. 14, July 1994.

[26] Murtaza, S.S.; Anselm, K.A.; Srinivasan, A.; Streetman, B.G.; Campbell, J.C.; Bean, J.C.; Peticolas, L.; , "High-reflectivity Bragg mirrors for optoelectronic applications," *Quantum Electronics, IEEE Journal of* , vol.31, no.10, pp.1819-1825, Oct 1995.

[27] Cho, A. Y. (ed) 1994 Molecular Beam Epitaxy (Woodbury, NY:AIP)

[28] Robin f. C. Farrow, “Molecular Beam Epitaxy: Applications of Key Materials,: Noyes Publications. Park Ridge, NJ. 1995. *ISBN 0-8155-1371-2.*

[29] Sadao Adachi, “GaAs, AlAs, and $Al_{[x]}Ga_{[1-x]}As$: Material parameters for use in research and device applications,” *J. Appl. Phys.* 58, R1 (1985), DOI:10.1063/1.336070

[30] D. A. B. Miller, “Optical Physics of Quantum Wells,” *AT&T Bell Laboratories.* Holmdel, NJ.

[31] *Image: http://web.tiscali.it/decartes/phd_html/III-Vms-mbe.png*

[32] M. A. Herman and H. Sitter, “Molecular Beam Epitaxy: Fundamentals and Current Status,” Springer-Verlag Berlin Heidelberg, NY. 1996. *ISBN*: 3-540-60594-0.

[33] B. E. A. Saleah and M. C. Teich, “Fundamentals of Photonics,” 2nd Ed. John Wiley & Sons Inc. 2007. *ISBN*: 9780-471-35832-9.

[34] M. Ohring, “The Material Science of Thin Films,” Academic Press, 1992.

[35] T. H. Gfoerer, “Photoluminescence in Analysis of Surfaces and Interfaces,” *Encyclopedia of Analytical Chemistry*. R. A. Meyers (Ed.) pp. 9209-9231. John Wiley & Sons Ltd. 2000.

[36] S. Perkowitz, “Optical Characterization of Semiconductors,” Academic Press. 1993.

[37] Donald A. McQuarrie, “The Kronig-Penney Model: A Single Lecture Illustrating the Band Structure of Solids,” vol. 1 no. 1. The Chemical Educator. ISSN 1430-4171 (1996).

[38] IUPAC Compendium of Chemical Terminology, 2nd Edition (1997).

[39] B. G. Kim, E. Garmire, S. Hummel, and P. D. Dapkus, "Nonlinear Bragg reflector based on saturable absorption," *Appl. Phys. Lett.* 54 (12), 20 March 1989.

[40] S. Hastings, M. J. A. de Dood, H. Kim, W. Marshall, H. Eisenberg, and D. Bouwmeester, "Ultrafast optical response of a high reflectivity GaAs/AlAs Bragg mirror," *Appl. Phys. Lett.* 86 (3) 031109. (2005).

[41] Neamen, D. A. *Semiconductor Physics and Devices: Basic Principle*, 3rd ed.2003.

[42] Handbook of Optics, sponsored by the Optical Society of America. 2nd ed. vol. 2, 1994

[43] Palmer, C.; Stravrinou, P. N.; Whitehead, M.; Phillips, C. C.;, "Mid-infrared (λ ~ 2-6 μm) measurements of the refractive indices of GaAs and AlAs," *Semiconductor Science and Technology, 2002*, no.,pp.1189-1192, 16 Oct. 2002.

[44] S. H. Wemple and M. DiDomenico Jr., "Behavior of the Electronic Dielectric Constant and Ionic Materials," *Phys. Rev. B 3,* pp.1338-1351, 1971.

[45] J. Trull, C. Cojocaru, J. Massaneda, R. Vilaseca, and J. Martorell, "Determination of Refractive Indices of Quarter-Wavelength Bragg Reflectors by Reflectance Measurements in Wavelength and Angular Domains," *Appl. Opt.* 41, 5172-5178 (2002).

[46] J. C. Bean, L. J. Peticolas, R. Hull, D. L. Windt, R. Kuchibhotla, and J. C. Campbell, "Design and fabrication of asymmetric strained layer mirrors for optoelectronic applications," *Appl. Phys. Lett.* 63, 444 (1993).

[47] T. Makino, "Transfer Matrix Method With Applications To Distributed Feedback Optical Devices," *PIER* 10, 271-319, 1995.

[48] Z. Y. Li, B. Y. Gu, and G. Z. Yang, "Slowly varying amplitude approximation appraised by transfer-matrix approach," *Phys. Rev.* B vol. 60. (15). 15 October 1999.

[49] G. D. Boyd, D. A. B. Miller, D. S. Chemla, S. L. McCall, A. C. Gossard, and J. H. English, "Multiple quantum well reflection modulator," *AT&T Bell Laboratories*. 1987.

[50] Campbell, S. A. The Science and Engineering of Microelectronic Fabrication. 2nd ed., New York, New York, Oxford University Press Inc. 2001.

[51] *Infrared Atmospheric Transmission Spectra,* University of Virginia Department of Astronomy,
URL: http://www.astro.virginia.edu/~mfs4n/ir/atmtrans.html

[52] D. S. Katzer, W. S. Rabinovich, K. Ikossi-Anastasiou, and G. C. Gilbreath, "Optimization of buffer layers for InGaAs/AlGaAs PIN optical modulators grown on GaAs substrates by molecular beam epitaxy," *J. Vac. Sci. Technol.* B 18(3), May/Jun 2000.

[53] D. S. Katzer, W. S. Rabinovich, K. Ikossi-Anastasiou, and G. C. Gilbreath, "Optimization of buffer layers for InGaAs/AlGaAs PIN optical modulators grown on GaAs substrates by molecular beam epitaxy," *J. Vac. Sci. Technol.* B 18(3), May/Jun 2000.

[54] Y. Fu, M. Willander, E. L. Ivchenko, and A. A. Kiselev, "Valley mixing in GaAs/AlAs multilayer structures in the effective mass method*," Phys. Rev.* B 47 (20). May 1993.

[55] R. Bonnefoi, D. H. Chow, T. C. McGill, R. D. Burnham, and F. A. Ponce, "Current transport mechanisms in GaAs/AlAs tunnel structures grown by metal-organic chemical vapor deposition," *J. Vac. Sci. Technol.* B 4 (4), Jul/Aug 1986.

[56] R.T Collins, J. Lambe, T. C. McGill, and R. D. Burnham, "Inelastic tunneling characteristics of AlAs/GaAs heterojunctions," *Appl. Phys. Lett.* 44 (5). 1 March 1984.

[57] R. Bonnefoi, R. T. Collins, T. C. McGill, R. D. Burnham, and F. A. Ponce, "Resonant tunneling in GaAs/AlAs heterostructures grown metal organic chemical vapor deposition," *Appl. Phys. Lett*. 46, 285 (1985).

[58] H. Sakaki, T. Noda, K. Hirakawa, M. Tanaka, and T. Matsusue, "Interface roughness scattering in GaAs/AlAs quantum well," *App. Phys. Lett.* 51 (1934). 1987.

[59] A. R. Bonnefoi, D. H. Chow, T.C. McGill, R. D. Burnham, and F. A. Ponce, "Current transport mechanisms in GaAs/AlAs tunnel structures grown by metal-organic chemical vapor deposition," *J. Vac. Sci. Technol.* B 4(4), Jul/Aug 1986.

[60] J. Y. Duboz, M. Hughues, B. Damilano, A. Nedelcu, P. Bois et al., "Infrared detectors based on InGaAsN/GaAs intersubband transitions," *App. Phys. Lett.* 94, 022103 (2009).

[61] M. Shinohara, "Dislocation-free GaAs epitaxial growth with the use of modulation-doped AlAs-GaAs superlattice buffer layers," *App. Phys. Lett. 52, 7, p.543 (1988).*

[62] Q. Gong, "Stable nonplanar surface formed on patterned GaAs (311)A substrate by MBE," *Appl. Phys. Lett. 77, 3538 (2000)*

[63] Levine, B. F., Cho, A. Y., Walker, J., Malik, R. J., Kleinman, D. A., and Sivco, D. L., 1988 *Appl. Phys. Lett. 52 1481..*

VITA

Stanley Ikpe was born on the 31st of January of 1985 to Stephenson and Philomina Ikpe in Kansas City, Missouri. The third of their four children, Stanley was the first in his family to pursue a doctoral degree. He has previously received his Bachelors of Science in Electrical & Computer Engineering (with Honors) in December of 2007. He then pursued and achieved his Masters of Science in Electrical Engineering from the University of Missouri at Columbia in December of 2009. Stanley successfully defended is doctoral dissertation on April 19, 2013 with aspirations of working in the Electrical and Computer Engineering industry and advancing the use of optoelectronic devices and their applications.